



THE UNIVERSITY OF
SYDNEY

COPYRIGHT AND USE OF THIS THESIS

This thesis must be used in accordance with the provisions of the Copyright Act 1968.

Reproduction of material protected by copyright may be an infringement of copyright and copyright owners may be entitled to take legal action against persons who infringe their copyright.

Section 51 (2) of the Copyright Act permits an authorized officer of a university library or archives to provide a copy (by communication or otherwise) of an unpublished thesis kept in the library or archives, to a person who satisfies the authorized officer that he or she requires the reproduction for the purposes of research or study.

The Copyright Act grants the creator of a work a number of moral rights, specifically the right of attribution, the right against false attribution and the right of integrity.

You may infringe the author's moral rights if you:

- fail to acknowledge the author of this thesis if you quote sections from the work
- attribute this thesis to another author
- subject this thesis to derogatory treatment which may prejudice the author's reputation

For further information contact the University's Copyright Service.

sydney.edu.au/copyright

FEATURE-DRIVEN VOLUME VISUALIZATION OF MEDICAL IMAGING DATA



THE UNIVERSITY OF
SYDNEY

A thesis submitted in fulfillment of the requirements for the degree of
Doctor of Philosophy.

Faculty of Engineering & Information Technologies

The University of Sydney

Younhyun Jung

October 2015

© Copyright by Younhyun Jung 2015

All Rights Reserved

Abstract

Direct volume rendering (DVR) is a volume visualization technique that has been proved to be a very powerful tool in many scientific visualization domains. Diagnostic medical imaging is one such domain in which DVR provides new capabilities for the analysis of complex cases and improves the efficiency of image interpretation workflows. However, the full potential of DVR in the medical domain has not yet been realized.

A major obstacle for a better integration of DVR in the medical domain is the time-consuming process to optimize the rendering parameters that are needed to generate diagnostically relevant visualizations in which the important *features* that are hidden in image volumes are clearly displayed, such as shape and spatial localization of tumors, its relationship with adjacent structures, and temporal changes in the tumors. In current workflows, clinicians must manually specify the transfer function (TF), view-point (camera), clipping planes, and other visual parameters. Another obstacle for the adoption of DVR to the medical domain is the ever increasing volume of imaging data. The advancement of imaging acquisition techniques has led to a rapid expansion in the size of the data, in the forms of higher resolutions, temporal imaging acquisition to track treatment responses over time, and an increase in the number of imaging modalities that are used for a single procedure. The manual specification of the rendering parameters under these circumstances is very challenging.

This thesis proposes a set of innovative methods that visualize important features in multi-dimensional and multi-modality medical images by automatically or semi-automatically optimizing the rendering parameters. Our methods enable visualizations necessary for the diagnostic procedure in which (i) 2D slice of interest (SOI) can be augmented with 3D

anatomical contextual information to provide accurate spatial localization of 2D features in the SOI; (ii) the rendering parameters are automatically computed to guarantee the visibility of 3D features; and (iii) changes in 3D features can be tracked in temporal data under the constraint of consistent contextual information. We also present a method for the efficient computation of visibility histograms (VHs) using adaptive binning, which allows our optimal DVR to be automated and visualized in real-time.

We evaluated our methods by producing visualizations for a variety of clinically relevant scenarios and imaging data sets. We also examined the computational performance of our methods for these scenarios.

Acknowledgements

The research presented in this thesis would not have been achieved without the assistance of many different people, especially that of my supervisors. Therefore, my most sincere gratitude is due to Prof. David Dagan Feng and Dr. Jinman Kim for their patient guidance and endless support during my PhD journey of the past four years. Their enthusiasm and eagerness have always been a driving force to me and I have done my best to match their expectations. I wish to thank Dr. Jinman Kim for his style of advising: encouraging me to do research projects independently from the beginning to the end. He never told me what to do next, but expected me to do it by myself first and then helped to make it better with a full heart. I am sure that the gains from this process will be amazingly helpful in my future career.

Prof. Michael Fulham and A. Prof. Stefan Eberl at Royal Prince Alfred Hospital deserve a special mention. It was a great pleasure to learn from them throughout my thesis. They consistently demonstrated compliancy to my research and also gave me incredible feedbacks. I would like to express my special thanks to Prof. Fulham who inspired me to come to a decisive idea, which led to one of the contributions in my thesis.

To my past and present colleagues in the Biomedical & Multimedia Information Technology (BMIT) research group, the Institute of Biomedical Engineering and Technology (BMET), and also Sydney Research Networks (SyReNS). I would like to express my thanks to all my past and present colleagues for creating such an amazing atmosphere in which to work and also to have fun and to provide contributions to my work whenever I needed it. My special thanks go to Dr. Ashnil Kumar. His kind support in guiding and proof reading my thesis has made it more scientific and concise. I am also grateful to Lei Bi and Robin Haung for providing their experiences in the area of medical image processing. My collaboration with

Euijoon Ahn allowed me to get insights into a different yet complementary research field, which has been a mind-broadening experience. It was a great opportunity to work alongside other colleagues including Liviu Constantinescu, Michael de Ridder, Mohib Shah, Ha Phan, and Falk Nette.

Very special thanks to my family for their endless emotional support throughout the years. Great thanks also to my uncle who motivated me to start my PhD journey as well as my aunts for their constant encouragements.

Table of Contents

Abstract	iii
Acknowledgements	v
List of Tables	xiii
List of Figures	xiv
List of Publications	xx
Abbreviations	xxii
1. Introduction	1
1.1 Motivation	2
1.1.1 Volume Visualization in Clinical Use	2
1.1.2 Leveraging Image Processing and Computer Graphics	5
1.2 Aims	6
1.3 Contributions of this Thesis	7
1.4 Outline of this Thesis	8
2. Background	9
2.1 Volume Visualization Pipeline for Medical Imaging Data	10
2.2 Medical Imaging Data Acquisition	11
2.2.1 Anatomical Imaging Modalities	12
2.2.2 Functional Imaging Modalities	14

2.2.3	Multi-modality Imaging.....	15
2.3	Image Processing.....	16
2.4	Direct Volume Rendering	17
2.4.1	Optical Models	17
2.4.2	Volume Ray Casting.....	20
2.5	Transfer Functions	21
2.5.1	Pre- and Post-classified TF	22
2.5.2	One-dimensional Transfer Functions	22
2.5.3	Multi-dimensional Transfer Functions	23
2.6	Fused Volume Visualization for Multi-modality Images.....	24
3.	Datasets and Visualization Environment	25
3.1	Datasets and Pre-processing.....	26
3.2	Visualization Environment.....	27
4.	Augmentation of 3D Contextual Information on 2D Medical Image Slice Views	29
4.1	Introduction	31
4.2	Related Work.....	36
4.2.1	ROI-based Visualization.....	36
4.2.2	Volume Clipping.....	37
4.2.3	Volume Ray Casting.....	38
4.2.4	Multi-modality Medical Imaging Visualization.....	39

4.3	Methods.....	40
4.3.1	Overview.....	40
4.3.2	Occlusion Distance Histogram Generation and Augmentation Depth Computation.....	42
4.3.3	Dynamic Generation of Opacity Weight Curve.....	43
4.3.4	Fusion of a PET SOI and a CT DVR.....	45
4.4	Implementation.....	45
4.4.1	Occlusion Distance Map Generation.....	46
4.4.2	Occlusion Distance Histogram Generation.....	46
4.5	Results.....	47
4.5.1	OSVRA Visualization.....	48
4.5.2	Computational Performance of OSVRA.....	57
4.5.3	A User Study using Clinical PET-CT Studies with Lung Cancer.....	58
4.6	Discussion.....	61
4.7	Conclusions.....	63
5.	An Automated Region of Interest -based Visibility-driven Direct Volume Rendering Technique.....	65
5.1	Introduction.....	67
5.2	Related Work.....	68
5.2.1	Transfer Function Manipulation.....	68

5.2.2	Visibility-driven Transfer Function.....	69
5.2.3	Segmentation-based Region of Interest Visualization.....	70
5.3	Methods.....	71
5.3.1	Overview.....	71
5.3.2	Regions of Interest Segmentation.....	72
5.3.3	Regions of Interest-based Multi-modality Visibility Histogram.....	73
5.3.4	Automated Transfer Function Optimization	74
5.3.5	User Interaction for Regions of Interest Definition.....	76
5.4	Implementation.....	77
5.5	Results.....	77
5.5.1	Synthetic Image Volumes	77
5.5.2	Whole-body PET-CT Studies	79
5.5.3	Computational Performance	82
5.6	Discussion	84
5.7	Conclusions	85
6.	Tracking and Visualizing the Changes in Regions of Interest over Temporal Image Volumes	86
6.1	Introduction	88
6.2	Related Work.....	90
6.2.1	Temporal Volume Visualization	91

6.2.2	Automatic visibility-driven Transfer Function Optimization	92
6.2.3	Temporal Segmentation of Abnormalities in PET Image Volumes	92
6.3	Methods.....	93
6.3.1	Transformation Indices Generation via Temporal Image Volume Registration.....	94
6.3.2	Temporal Region of Interest Segmentation	95
6.3.3	Automatic Visibility-driven Transfer Function Optimization for Temporal PET-CT Image Volume	96
6.4	Implementation.....	97
6.5	Results.....	98
6.5.1	Temporal Visualization Using Clinical PET-CT Studies	98
6.5.2	PET Region of Interest Segmentation Performance.....	102
6.5.3	Computational Performance	106
6.6	Conclusions	107
7.	Visibility Computation Optimization based on Adaptive Binning.....	109
7.1	Introduction.....	111
7.2	Related Work.....	113
7.2.1	Visibility-driven Transfer Function Manipulation	113
7.2.2	Adaptive Binning in Histogram Construction.....	114
7.3	Methods.....	114

7.3.1	Adaptive Binning of Visibility Histogram.....	115
7.3.2	Dissimilarity Measurement of Adaptively Binned Visibility Histogram to Full-Bin Counterpart	116
7.3.3	Automatic Transfer Function Optimization using Adaptively Binned Visibility Histogram	117
7.4	Implementation.....	117
7.4.1	CUDA-based <i>K</i> -Means Cluster analysis.....	117
7.4.2	Visibility Histogram	118
7.5	Results.....	119
7.5.1	Adaptive Binning on Visibility Histogram	119
7.5.2	Adaptive Binning in Visibility-driven Volume Manipulations.....	122
7.5.3	Adaptive Binning in Automatic Visibility-driven Transfer Function Manipulations.....	125
7.5.4	Computational Efficiency	127
7.6	Discussion	128
7.7	Conclusions	130
8.	Conclusions.....	131
8.1	Future Work	133
9.	List of References.....	135

List of Tables

6-1: DSC results of PET ROI segmentation using our algorithm (CA) in a comparison with region-based (CCRG and SRG) algorithms.....	104
7-1: Dissimilarity indices of the AB-K+ in ROI-based TF optimization and view-independent TF definition, among different bin sizes.....	125

List of Figures

1.1: DVR visualizations of a multi-modality PET-CT lung cancer patient	4
2.1: The volume visualization pipeline for medical imaging data	10
2.2: Medical imaging data acquisition	11
2.3: A whole-body CT image	12
2.4: A brain MR image.....	13
2.5: An abdomen CTA image.....	14
2.6: Slices from different planes of a whole-body PET image	15
2.7: Axial views (top-to-bottom) of multi-modality PET-CT	16
2.8: An overview of DVR light ray model	18
2.9: A standard 1D TF.....	23
2.10: A multi-dimensional intensity-gradient-based TF.....	24
3.1: The component-based GPU visualization framework of Voreen showing one of the proposed visualization methods	28
4.1: Cross-sectional view planes of PET-CT data of a patient with disseminated lung cancer with skeletal metastases	32
4.2: Different volume rendering visualizations applied to PET-CT image volumes in transaxial views	34
4.3: An overview of the OSVRA with PET-CT image volumes.	41

4.4: Construction of the occlusion distance histogram allows for structure-level depth D analysis.....	43
4.5: Opacity weight curve generation based on a logistic function.....	44
4.6: Efficient computation of the occlusion distance map and resulting histogram, using parallel GPU architecture.....	46
4.7: An example of our OSVRA and conventional slice-based volume rendering with manual clippings at various depths.....	48
4.8: OSVRA results using various D values.....	50
4.9: A patient study with the bone marrow involvement of the proximal humeri (see arrows in (a)).....	51
4.10: Slice-by-slice image volume navigation with OSVRA in comparison to coronal view planes of PET, applied to the same PET-CT patient study as in Figure 4.9.	53
4.11: A patient with lymphoma at the base of the neck and in the mediastinum.....	54
4.12: A PET-CT study in a patient with a large right lung tumor showing different TFs to OSVRA.....	55
4.13: A comparison of OSVRA with MIDA and DFE DVR methods	56
4.14: Processing times (ms) and frame rates (FPS) for OSVRA during typical volume manipulations in various viewport sizes.	57
4.15: The issues in accurately staging NSCLC in the thorax from a PET-CT study	61
5.1: An overview of our ROI-based visibility-driven visualization framework applied to multi-modality PET-CT image volumes.....	71
5.2: Calculation of the ROI-based multi-modality PET-CT VHs.....	73

5.3: An example of ROI selection in multi-modality visibility-driven visualization.	76
5.4: Illustration of composite and view dependencies of multi-modality VHs on two aligned image volumes.	78
5.5: PET-CT visualizations using a pair of single-modality visibility-driven TFs ((a) and (b)) compared with multi-modality visibility-driven TF ((c) to (e))......	79
5.6: Automatic CT TF optimization according to varying constraint of PET ROI's visibility tolerance from low (0.2) to high (0.8).	80
5.7: Optimized visualization results for a PET-CT study consisting of multiple ROIs across the whole body.....	81
5.8: The computational performance of ROI-based visibility-driven multi-modality PET- CT visualization	83
6.1: Tracking tumor changes using a combined visualization of PET-CT image views.....	89
6.2: An overview of our temporal visualization framework.....	94
6.3: GPU-based visibility computation among the temporal ROIs using MRT.	97
6.4: Temporal segmentation and visualization on a patient study diagnosed with lymphoma	99
6.5: Optimized visualization results during view-point rotations for a PET-CT patient study with a lymphoma in the neck	100
6.6: A comparison of our temporal optimization to per-scan optimization using a PET-CT patient study with multiple abnormalities (encapsulated in cuboids) in different sites across three time points (T_1 to T_3)......	102

6.7: Segmentation results on three different types of ROIs: (a) a small tumor (8×zoom); (b) a middle sized tumor (6×zoom); and (c) a lymphoma of multiple separated regions (2×zoom).....	105
6.8: The tolerance of our visibility-driven TF optimization to errors in ROI segmentation.	106
6.9: The computational performance of our temporal visualization	107
7.1: VH construction with 3 different binning schemes	112
7.2: An overview of AB-VH applied to the visualization of multi-modality PET-CT image volumes.....	114
7.3: GPU-based computation of AB-VH using MRT.	118
7.4: FB-VH with 4096 bins of a CT image volume (as in Figure 7.2) compared to its AB- K+ and also to its EB variants	119
7.5: Dissimilarities in the VH distribution of AB-K+ and EB relative to FB plotted according to the bin sizes using a CT image volume.....	120
7.6: The visibility dissimilarities to FB over CT (a) and PET (b), and brain MR (c) using AB algorithms (blue, red, and green bars) in comparison to those of EB (violet bars)	121
7.7: A case study of a high-resolution CT image volume with the application of 64 AB- K+ in visibility-driven TF manipulation.....	122
7.8: View-point manipulations during the visualization of a high-resolution CT study	123
7.9: A volume clipped brain MR visualization (left column) using 64 AB-K (top row) in comparison to FB (bottom row).	124
7.10: TF optimization results using a 64 AB-K+ and 4096 FB on a multi-modality PET- CT study.....	126

7.11: frame rate (FPS) of VH calculations (left y-axis) and time (seconds) taken for TF optimization computation (right y-axis) with 5 varying histogram bin sizes.	127
---	-----

List of Publications

The following publications were produced over the course of the candidature. Most of these publications were based on the research that is presented in this thesis. The other publications were related to work conducted by my colleagues, to which I made a significant contribution.

Journal Articles (accepted and in preparing)

1. **Y. Jung**, J. Kim, S. Eberl, M. Fulham, and D. Feng, “Visibility-driven PET-CT visualisation with region of interest (ROI) segmentation,” *The Visual Computer*, 29(6-8), pp. 805-15, 2013.
2. **Y. Jung**, J. Kim, M. Fulham, and D. Feng, “Occlusion-based slice of interest (SOI) augmented with volume rendering for PET-CT visualization,” *IEEE Transactions on Visualization and Computer Graphics*, under revision, 2015.
3. **Y. Jung**, J. Kim, A. Kumar, M. Fulham, and D. Feng, “Efficient visibility-driven visualization of medical images via adaptive binning of visibility histogram,” *Computerized Medical Imaging and Graphics*, submitted, 2015.
4. **Y. Jung**, J. Kim, L. Bi, M. Fulham, and D. Feng, “A Temporal Visualisation Framework for Multi-modality Medical Images,” in preparing for *Computer Graphics International*, 2016.

Conference and Symposium Proceedings

5. **Y. Jung**, J. Kim, and D. Feng, "Dual-modal visibility metrics for interactive PET-CT visualization," *IEEE Engineering in Medicine and Biology Society*, pp. 2696-2699, 2012.
6. **Y. Jung**, J. Kim, and D. Feng, "Adaptive histogram with visibility-driven transfer function for PET-CT visualization," *IEEE Pacific Visualization*, Abstract, 2013.
7. **Y. Jung**, J. Kim, M. Fulham, and D. Feng, "Occlusion-based volume rendering augmentation for slice of interest (SOI) visualization," *Computer Graphics International*, short paper, 2014.
8. **Y. Jung**, J. Kim, M. Fulham, and D. Feng, "Opacity-driven volume clipping for slice of interest (SOI) visualization of multi-modality PET-CT volume," *IEEE Engineering in Medicine and Biology Society*, pp. 6714-6717, 2014.
9. **Y. Jung**, J. Kim, M. Fulham, and D. Feng, "Volume Rendering Augmentation on Slice of Interest (SOI) For Visualisation Of Thoracic PET-CT," *Computer Assisted Radiology and Surgery*, Vol 10 (supplement1), accepted, 2015

Other Contributed Publications

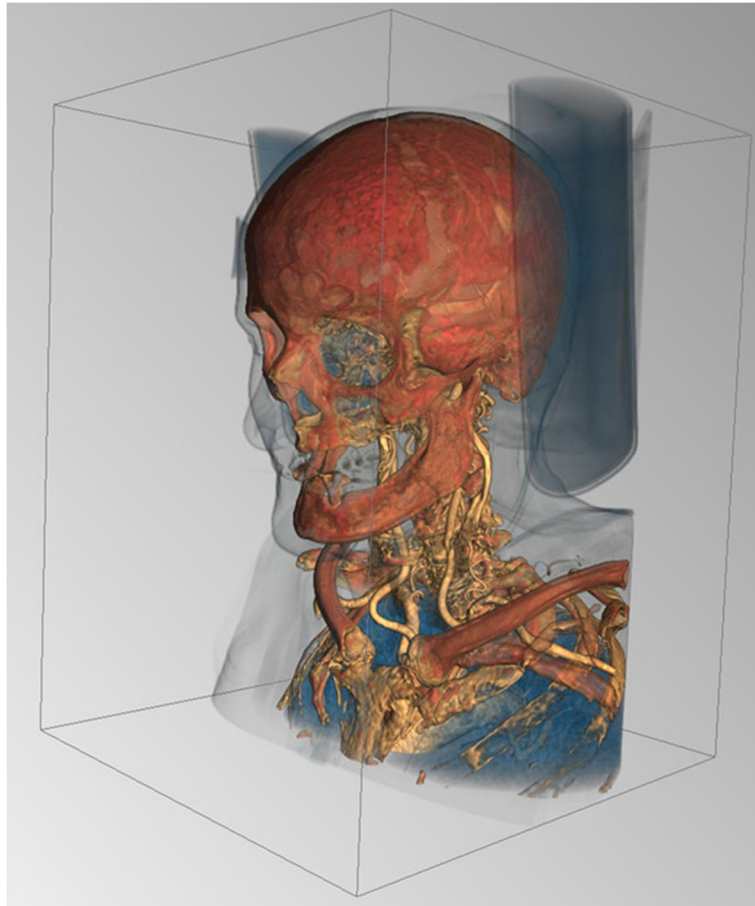
10. M. de Ridder, L. Constantinescu, L. Bi, **Y. Jung**, A. Kumar, J. Kim, M. Fulham, and D. Feng, "A Web-based multimedia visualisation interface for personal health records," *IEEE Computer-Based Medical Systems*, pp. 191-196, 2013.
11. E. Ahn, L. Bi, **Y. Jung**, J. Kim, M. Fulham, and D. Feng, "Automated Saliency-based Lesion Segmentation in Dermoscopic Images," *IEEE Engineering in Medicine and Biology Society*, accepted, 2015.
12. R. Haung, L. Bi, C. Li, **Y. Jung**, J. Kim, M. Fulham, and D. Feng, "A Locally Constrained Knowledge-Based Random Walk Approach for Airway Segmentation

- on Low-Contrast Computed Tomography (CT) Images,” *International Conference on Digital Image Computing Techniques and Applications (DICTA)*, accepted, 2015.
13. E. Ahn, L. Bi, **Y. Jung**, J. Kim, M. Fulham, and D. Feng, “Saliency-based Lesion Segmentation via Background Detection in Dermoscopic Images,” *IEEE Transactions on Biomedical Engineering*, submitted, 2015.
 14. M.D. Ridder, **Y. Jung**, R. Huang, and J. Kim, “Exploration of Virtual Reality for Visual Analytics and 3D Volume Rendering of Functional Magnetic Resonance Imaging (fMRI) Data,” *IEEE International Symposium on Big Data Visual Analytics*, accepted, 2015.
 15. M.A. Nicdao, T. Baldacchino, J. Kim, R. Johnston, M. Mikaheal, A. Patekar, **Y. Jung**, K. Sud, “REACH OUT: the Home Hemo App Project (Real-time Evaluation, Action and Communication (without leaving) Home through Optimal Use of Technology), in preparing for *Renal Society of Australasia Journal*, 2015.

Abbreviations

CT	Computed Tomography
DVR	Direct Volume Rendering
GPU	Graphics Processing Unit
FPS	Frames per Second
MR	Magnetic Resonance
MRT	Multiple Render Targets
PET	Positron Emission Tomography
RGBA	Red-Green-Blue-Alpha
ROI	Region of Interest
SNR	Signal-to-Noise Ratio
SOI	Slice of Interest
TF	Transfer Function
VH	Visibility Histogram

1. Introduction



Volume visualization of medical imaging data

A fundamental element of life sciences is the analysis of data generated during experiments. However, the data are of little use unless they are presented in a form that is interpretable by humans. Visualization is the process of transforming the data into a visual form that can aid in its understanding by humans. Visualization allows scientists and engineers to effectively derive information that are hidden in the data; and are needed for data exploration and analysis [1]. The impact of visualization is rapidly increasing and the medical domain is a prime beneficiary where there is the need to assimilate and interpret massive amounts of imaging data acquired from multi-dimensional (3D spatial + 1D temporal) and multi-modality imaging scanners. This thesis aims to facilitate the visualization of medical imaging data, thereby improving the efficiency of data exploration and enabling new diagnostic capabilities in the medical domain.

1.1 Motivation

1.1.1 Volume Visualization in Clinical Use

Medical imaging is fundamental to modern healthcare as it enables the visual inspection of the interior of a human body in a non-invasive manner, which is essential for clinical diagnosis [2, 3]. There have been vast research and industry efforts into the development of new imaging devices to scan patients and techniques to improve the image quality and diagnostic capabilities of the acquired images. The acquisition of imaging data is only the first step in the diagnostic procedure. Visualization is a key step within this procedure; its purpose is to effectively present the data for diagnostic interpretation and assimilation by clinicians [4].

Most modern medical imaging data are volumetric in nature, i.e., the shape, size, and location of the organs and tissues are natively specified in 3D spatial dimensions. Medical image volumes consist of a stack of 2D slices that collectively represent 3D information. However, current medical imaging visualization techniques are dominated by 2D cross-sectional view planes where clinicians interact with the medical imaging data using a single 2D slice of interest (SOI) at a time [5]. In such 2D visualization approaches, clinicians must manually navigate through the entire image stack and then mentally reconstruct the 3D information. Image interpretation based on such mental 3D reconstruction is a subjective task with a high dependence on the skill, training, and experience of the clinicians who are performing the interpretation. In an attempt to complement such viewing approaches, volume visualization methods have been introduced in order to reduce this subjectivity [6]. One such method is direct volume rendering (DVR), which provides objective volumetric information generated by computer graphics algorithms.

Senior clinicians (e.g., radiologists) are experts at mentally reconstructing 3D visualizations from the image stacks, due to their extensive training and experience in 2D cross-sectional view approaches. As the mental reconstruction process is already in part of their normal imaging interpretation workflow, they may be less reliant on computer-generated 3D DVR visualizations. Nevertheless, the mental reconstruction does not have as much information as what computer-aided DVR can provide, and a rapid and accurate overview of the volumetric information in DVR is still valuable for their workflows [7]. In addition, other clinicians who do not have the same experience benefit more from DVR visualizations to complement their 2D cross-sectional view approaches [6].

Although DVR has a tremendous potential to improve image interpretation workflow, it is not currently fully embedded within clinical routine. A primary reason for this lack of adoption is due to the technical limitations of DVR applications in the clinical context.

Generic DVR methods require extensive manual tweaking of the rendering parameters to tune the visualization so that the important *features* of the image volume are clearly depicted, such as the tumors, its surrounding anatomical structures, and temporal changes in the tumors. However these tuning of the parameters are time-consuming and have high learning curve [8]. By default DVR methods generate the visual abstraction of the imaging data by displaying all the information within the volume at once. The important visual information (features) are often occluded by less important information and become invisible. This problem is exemplified in Figure 1.1, which shows DVR visualizations of a multi-modality positron emission tomography and computed tomography (PET-CT) image scan of a lung cancer patient. The feature of interest is the lung cancer from PET (see the arrow in Figure 1.1(b)) and the surrounding organs and tissues.

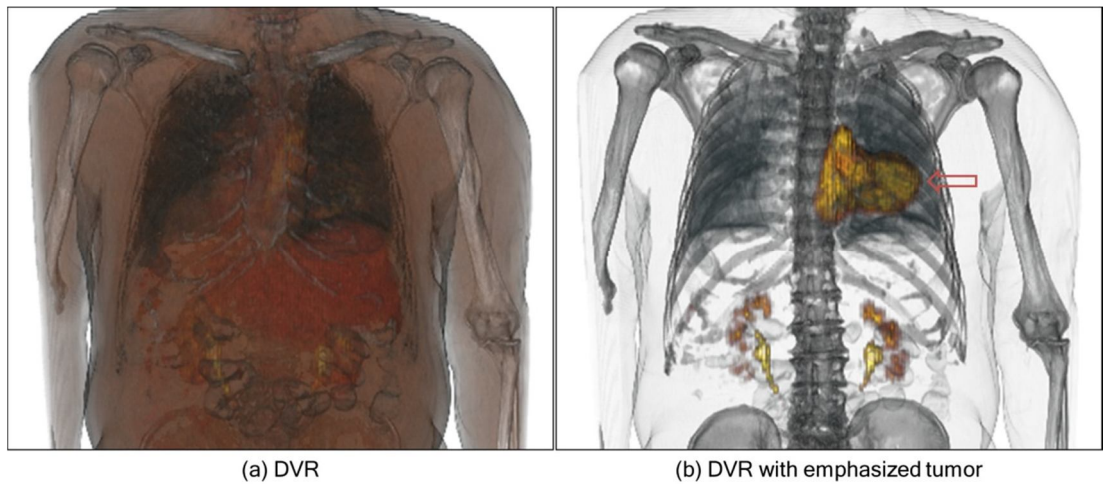


Figure 1.1: DVR visualizations of a multi-modality PET-CT lung cancer patient. In (a) DVR shows the default rendering where all the structures in the patient data are rendered and therefore the lung cancer (indicated by the arrow) is obstructed from the view by unnecessary structures. In (b) a useful visualization, in this case, the depiction of the lung cancer, can be created if less important structures can be de-emphasized.

Figure 1.1(a) is a default DVR in which all structures in the image volume pair are visualized and the feature of interest become occluded by non-relevant structures closer to the view-point, e.g., the muscles and the bone above the pit of the stomach. In comparison, the visualization in Figure 1.1(b) ensures the visibility of the lung cancer by making the non-relevant structures transparent.

The generation of this diagnostically relevant visualization inevitably requires the manual specification of a large number of the DVR rendering parameters that are responsible for what is rendered and how they appear [8]. Clinicians must manually optimize the parameters that control color mapping of the imaging data, view-point settings, clipping planes, and other options. The difficulty of this time-consuming manual task is further compounded in its application to clinical routine where clinicians are usually novices in 3D DVR and have patients, rather than computer systems, as the focus of their work.

Another obstacle for the limited adoption of DVR in the imaging workflow is the ever increasing size of medical imaging data generated for each patient. The advancement of imaging acquisition techniques have led to more images at higher resolutions, temporal image scans to track treatment responses over time, and an increase in the number of imaging modalities. Efficient DVR visualization in these circumstances is a greater challenge. An automatic visualization method is required, one that identifies the features that are diagnostically important and generate the optimal visualizations of the image features.

1.1.2 Leveraging Image Processing and Computer Graphics

The dramatic improvements in modern image processing and computer graphics have the potential to introduce new capabilities in the field of medical imaging visualization. The computing capabilities of modern equipment with the technical improvements mean that

better solutions and more complex approaches can be formulated to answer the open research questions in a wide range of visualization fields.

The application of image processing techniques to medical imaging has introduced new capabilities to enable automatic or semi-automatic extraction of clinically relevant information from the data [9-12]. Image segmentation is a core image processing method that has been widely utilized in the medical domain as an approach to aid in the automatic identification and derivation of features from the images. Image segmentation typically works by partitioning a medical image into sub regions, or regions of interest (ROIs), that share common characteristics; the regions usually correspond to different tissues, organs, pathologies, or other biologically relevant structures. Unfortunately, due to challenges in combining image processing within real-time volume visualization, visualization research has not yet fully leveraged the capabilities from image processing, especially towards multi-modality medical images.

The advancement of computer graphics techniques provides the potential to improve the visual quality of DVR visualizations for medical imaging data [13]; the parallelism and programmability of modern graphical processing units (GPUs) enables the interactive DVR visualizations of massive imaging data [14-16]. State-of-art GPU-based computer graphics techniques can be utilized to provide efficient image processing and DVR calculations that are fundamental to enabling real-time visualization.

1.2 Aims

The overall aim of the research presented in this thesis is to pioneer new feature-driven volume visualization approaches for enhancing the diagnostic capabilities while simplifying

the required user interaction. Achieving this overall aim will require the fulfillment of the following specific objectives:

1. Automated image processing methods for the identification and derivation of the features, and its embedding to the DVR visualization.
2. Optimized visualization of the features by automatically exploring the rendering parameter space and specifying the ideal parameters that ensure the visibility of features.
3. Interactive real-time DVR visualization leveraging the advances in GPU-based computer graphics and imaging processing methods.

1.3 Contributions of this Thesis

In order to address the aims above, this thesis contains the following innovative contributions:

1. **A method for augmenting the visualization of 2D SOI with 3D contextual information.** This proposed method automatically augments the 2D features in the SOI with the 3D structural context without impairing the view of the features. This is a significant advancement over current approaches which rely on human's mental reconstruction of the surrounding 3D contextual information.
2. **An automated ROI-based visibility-driven DVR technique.** This new technique generates visualizations of the 3D ROIs (features) while preserving the surrounding structures without compromising the visibility of the ROIs. This is an advancement over current approaches, where ROIs are often occluded by surrounding structures.
3. **A method for tracking and visualizing changes in ROIs over temporal image volumes.** An innovate DVR method ensures that the 3D ROIs in temporal image

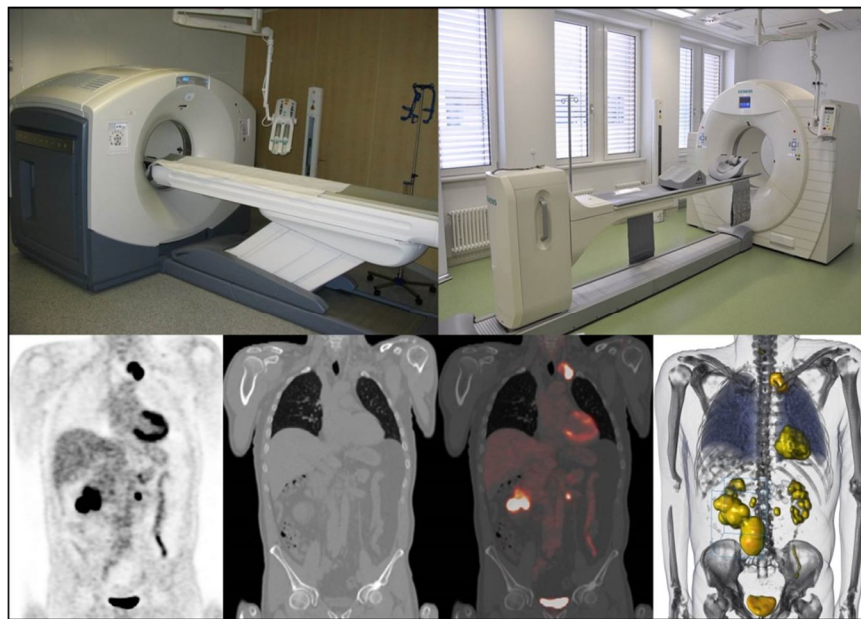
volumes are tracked and displayed under a consistent context, defined by the surrounding structures. This is an advancement in the visualization of temporal image volumes simultaneously where current approaches cannot provide consistent context among the volumes.

4. **An optimization of the visibility computation through the use of adaptive binning.** The proposed optimization method uses dynamically adaptive histogram bins to represent the distribution of voxel visibilities, thereby enabling real-time computation and interactivity during complex visualizations. Current approaches are typically limited to small image volumes with limited interaction.

1.4 Outline of this Thesis

The remainder of this thesis is organized as follows. An overview of the medical imaging volume visualization pipeline is given in Chapter 2. In Chapter 3, we discuss the medical image datasets being used and the pre-processing applied to these datasets as well as visualization environment for the development of the proposed methods. The next four chapters describe the core contributions of the thesis. An alternative to the 2D cross-sectional view planes is introduced in Chapter 4. Chapter 5 presents ROI-based visibility-driven DVR automation. Chapter 6 describes an automated visualization approach for temporal medical image volumes. Efficient computation for visibility and real-time visualization automation is described in Chapter 7. Finally, Chapter 8 summarizes the contributions of the thesis and presents directions for future work.

2. Background



Medical image acquisition and visualization

This chapter introduces the key concepts related to the volume visualization of medical imaging data. The presentation is not meant to be exhaustive, but rather, act as an introduction to the research area, with a focus on fundamental topics necessary for understanding the latter parts of this thesis. We recommend the following books for a comprehensive account of medical imaging visualization: *Visualization in Medicine: Theory, Algorithm, and Applications* [17] and *The Visualization Handbook* [18].

2.1 Volume Visualization Pipeline for Medical Imaging Data

Figure 2.1 shows the pipeline for the volume visualization of medical imaging data. The pipeline consists of the following sequence of steps: data acquisition, image processing, and volume rendering.

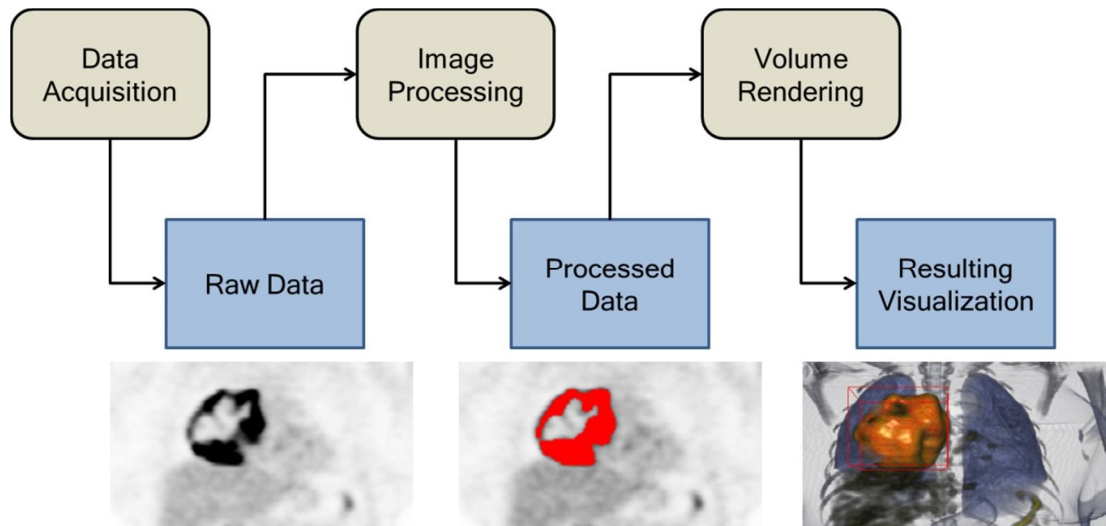


Figure 2.1: The volume visualization pipeline for medical imaging data. Raw data are acquired from imaging devices and processed for e.g., tumor segmentation. The processed data are then visualized via volume rendering techniques.

2.2 Medical Imaging Data Acquisition

This section provides a broad overview for different acquisition techniques and the data modalities, or data types, commonly used in clinical practice. Figure 2.2 shows the data acquisition process for volumetric medical imaging in which a cross-sectional image is generated by projecting the object at multiple angles. The cross-sectional image consists of discrete sample points, known as voxels, which are reconstructed on a regular 3D grid with a pre-defined resolution. Each voxel of this gray-scale image has a value that represents the intensity of structures in the object.

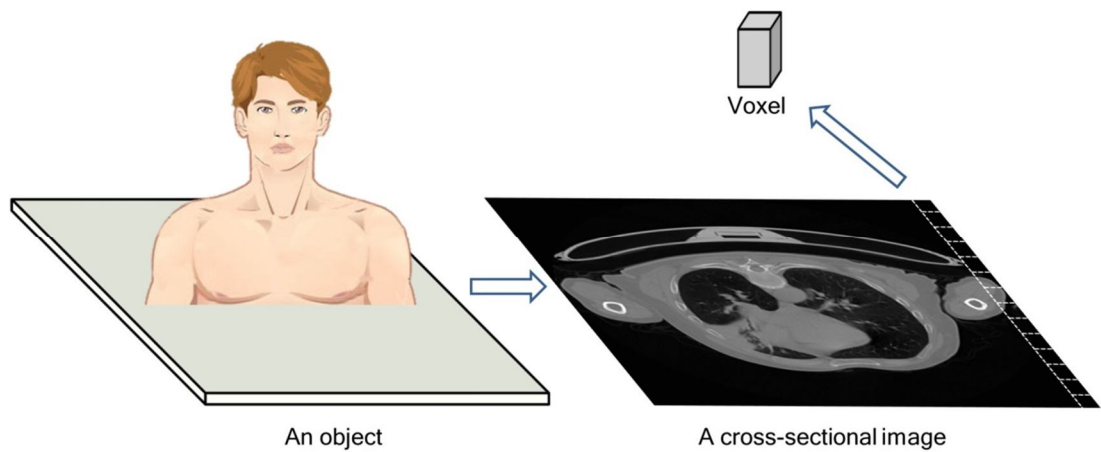


Figure 2.2: Medical imaging data acquisition. A gray-scale cross-sectional image consisting of voxels represents the intensities of structures in an object.

The voxel resolution of a volumetric image refers to the number of voxels in the image; this is usually represented as the number of voxels per dimension, e.g., $512 \times 512 \times 326$ voxels (width \times height \times depth). The spatial resolution of an image refers to the size of each voxel; for example, a voxel with the spatial resolution of $1.0 \text{ mm} \times 1.0 \text{ mm} \times 2.0 \text{ mm}$ depicts a region with volume 2.00 mm^3 . Images with higher spatial resolutions are capable of depicting finer details.

2.2.1 Anatomical Imaging Modalities

Anatomical imaging modalities capture images of the organs, skeleton, and tissues. One clinically important anatomical modality is computed tomography (CT), which is an advancement over traditional flat X-rays. CT produces high resolution volumetric images that are particularly well suited for inspecting dense structures [19], such as the bone or lung tissues, as shown in Figure 2.3. Different anatomical structures have highly predictable CT intensity range and is represented as Hounsfield Unit (HU) scale [20], thereby enabling the categorization of structures based on intensity information.

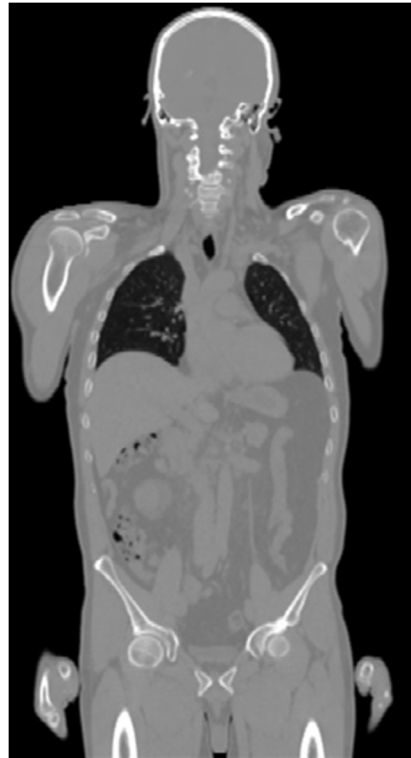


Figure 2.3: A whole-body CT image. The details of the bones, lungs, and other anatomical structures are clearly defined.

Magnetic resonance (MR) imaging is another volumetric anatomical imaging modality. Compared to CT, MR has a better separation of soft tissues [21]. Figure 2.4 shows a brain

MR image in which the internal tissues (white matter) are clearly distinguishable. The intensity value ranges of MR are usually less predictable than those of CT due to factors such as its dependency on the patient's body temperature [22].



Figure 2.4: A brain MR image. The details of the white matter (indicated by a white arrow) are clearly distinguishable.

Both modalities can be used with contrast agents to make certain structures easier to distinguish. CT angiography (CTA) is an example of the use of contrast agents with CT to enable the examination of blood vessels [23]. An X-ray contrast agent is injected into the patient, prior to CTA acquisition; the acquired images highlight the arterial and venous vessels throughout the body, as in Figure 2.5 that shows an abdomen CTA image.



Figure 2.5: An abdomen CTA image. The details of vascular structures (indicated by a white arrow) are clearly identifiable.

2.2.2 Functional Imaging Modalities

Functional imaging mainly focuses on capturing pathophysiological activities, such as metabolism or blood flow. Functional imaging modalities include single photon emission computed tomography (SPECT), perfusion imaging, functional MR (fMR), and positron emission tomography (PET). Figure 2.6 shows two slices from a PET image volume in which a lesion (indicated by the red arrows) is highlighted. Figure 2.6(a) is a slice from the image volume when viewed in the coronal (front-to-back) plane; Figure 2.6(b) shows the image in the sagittal (side-to-side) plane. In comparison to anatomical imaging modalities, functional imaging modalities generally have lower resolutions and Signal-to-Noise Ratio (SNR) but capabilities to detect pathophysiological activities [24].

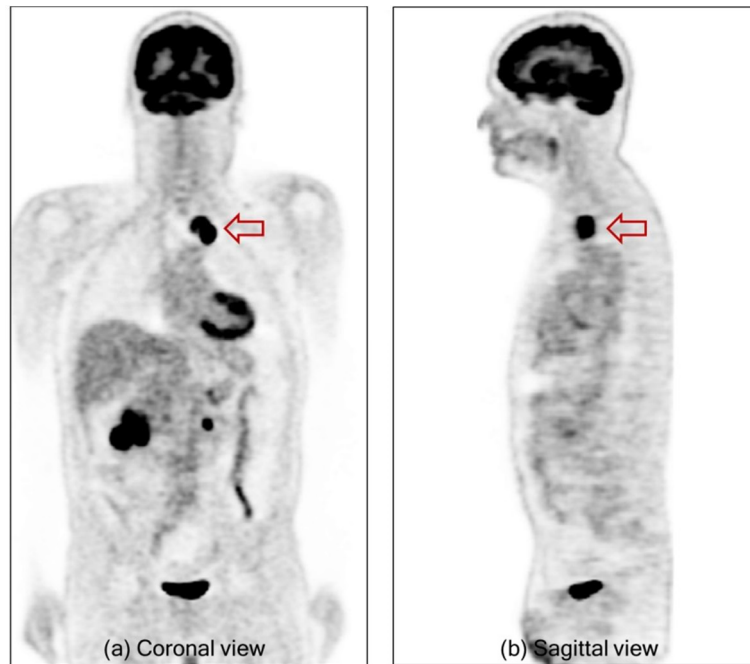


Figure 2.6: Slices from different planes of a whole-body PET image. The lesion (indicated by arrows) exhibits pathophysiological activities.

2.2.3 Multi-modality Imaging

Multi-modality imaging refers to the acquisition of multiple image types of the same patient. These multi-modality images were obtained as independent scans, but the advent of combined imaging scanners has enabled sequential acquisition of multiple image types during a single session [25, 26]. The acquired images are hardware co-aligned by the scanners. Each modality in such multi-modality images usually represents different but complementary information. Noticeable applications are seen in the combination of functional and anatomical modalities, such as multi-modality PET-CT imaging in which PET contains no anatomical information at all and CT has no functional information. It enables the visualization of pathophysiological activities with PET in the spatial context of anatomy provided by its counterpart CT, as shown in Figure 2.7. It allows the depiction of disease in structures that do not appear abnormal on CT [27].

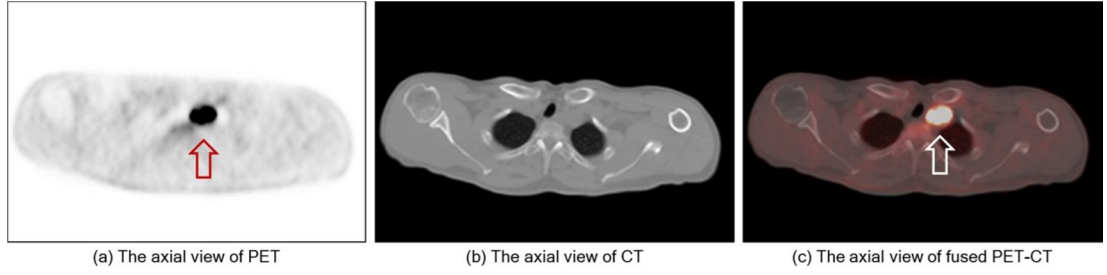


Figure 2.7: Axial views (top-to-bottom) of multi-modality PET-CT. (a) is the axial view of only PET; (b) is the axial view of only CT; and (c) is the axial view of fused PET-CT that depicts the lesion with PET (indicated by arrow) in the anatomical context provided by CT.

2.3 Image Processing

Segmentation is the process by which the pixels or voxels of an image are partitioned into different regions that share common characteristics [28]. It is generally used to identify boundaries, regions, or individual objects within an image. Pixel analysis is a core component of image segmentation. Common segmentation approaches include: pixel thresholding [9, 10], region growing [29], edge detection [30], fuzzy clustering [31], graph cuts [32], and statistical shape modeling [33]. The segmentation algorithms used in this thesis are mainly thresholding and region growing. Thresholding separates pixels into groups that have similar characteristics, such as intensities. Region growing analyses the neighboring pixels of one or more seed points (with the initial points usually selected manually) and recursively expands a region until the neighboring pixels share common characteristics.

Registration is the process of transforming two images of the same scene or object into the same coordinate space [12]. It is used to integrate information from images acquired from different devices, from different view-points, or at different times. A transformation matrix that maps pixels in the source image on the target images is generated during the procedure.

Registration is an optimization process that attempts to maximize the similarity of corresponding parts of the two images while minimizing the degree of transformation applied.

Registration algorithms can be classified according to the type of the transformation matrix. Linear registration algorithms apply global transformations for the mapping between two images, while non-linear registration algorithms are elastic and allow independent local morphing of different parts of the image [34, 35]. They are useful for medical image analysis where it is important to register different structures independently between images. This section was written based on [36]

2.4 Direct Volume Rendering

DVR is the process of presenting an entire 3D volume in a 2D visualization plane. This allows objects at all depths of the 3D data to be visualized at once. The term “direct” in DVR stems from the fact that the visualization is constructed directly from the data, as opposed to indirect approaches that generate an intermediate representation, e.g., a surface extracted from the data. The key advantage of DVR over other indirect volume rendering approaches is its ability to visualize the complete volume, thereby resulting in better visualizations of the interior of structures [4].

2.4.1 Optical Models

The DVR process imitates the functionality of a pinhole camera, with light passing through the data before reaching the viewer (camera). This process is based on a simplified model of the real physical phenomena that occur when light interacts with a participating medium. The optical models are often described as the net gain or loss (differential changes) of radiance (color and opacity) at any spatial location. Figure 2.8 shows how a ray of light is

affected when travelling through a volumetric data. Entry and exit points a and b on the surfaces of the cuboid are defined as the first and last intersections between the ray and the data. By evaluating the optical contribution of voxels along the ray, the initial light radiance I_0 is modulated to $I(b)$ at the exit point, i.e., the pixel value on the final visualization plane. This ensures that only those parts of the ray that intersect with the data contribute to the resulting visualization.

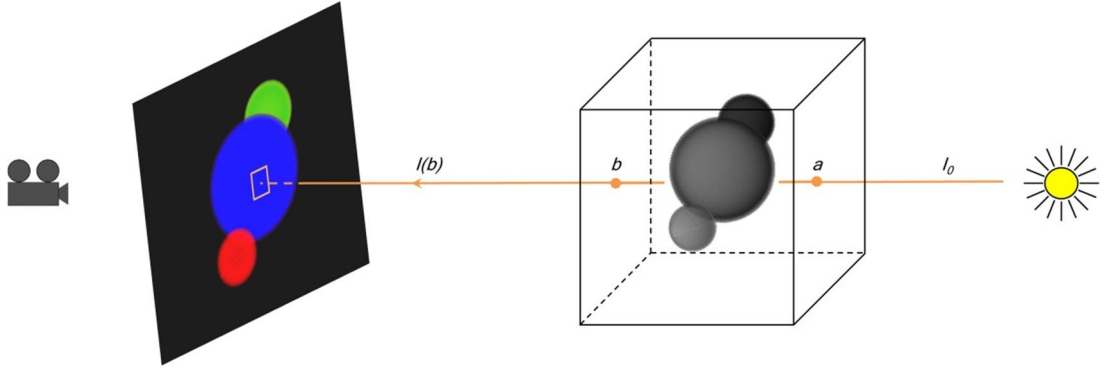


Figure 2.8: An overview of DVR light ray model. The color and opacity value of the pixel indicated by the orange rectangle is calculated as the radiance of a virtual light ray traversing the volumetric data. The initial value I_0 is modulated according to the optical properties of the volumetric data, with the resulting value $I(b)$.

The optical models commonly applied to DVR include emission and absorption, as well as scattering towards and away from voxels. For increased physical correctness, DVR equations need to be evaluated for all possible light directions and should consider all dominant optical models. Unfortunately, the evaluation of all the conditions is usually very computationally intensive and impractical. A good balance between the visual quality and computational cost is to limit the differential expression to the two models: emission ϵ and absorption κ [37]. Another simplification is to evaluate the DVR equation only for a single direction along the viewing ray. Let γ be the viewing ray. The simplified 1D radiance differential can be expressed as:

$$\frac{dI}{d\gamma} = \kappa(\gamma)I(\gamma) - \varepsilon(\gamma) \quad (2.1)$$

solving for I gives the following expression:

$$I(b) = I_0 + \int_a^b \varepsilon(\gamma) e^{-\int_0^\gamma \kappa(t) dt} d\gamma. \quad (2.2)$$

The expression in Equation 2.2 forms the volume rendering integral. It is presented here in its front-to-back form with the ray parameterized in the same direction. Most studies assume that there is no background radiance ($I_0 = 0$).

In general, the equation cannot be calculated analytically. Its numerical expression is derived by partitioning the ray to a large number of small segments $i \in [0, n]$. The following simplifications are also considered within each segment: emission is approximated as a function of absorption, $\varepsilon(\gamma) \approx c(\gamma)\kappa(\gamma)$; both color $c(\gamma)$ and absorption are assumed to be constant, $c(\gamma)\kappa(\gamma) \approx c_i\kappa_i$; and the resulting transparency expression is approximated by a Taylor expansion, $e^{-\kappa_i\Delta\gamma} \approx 1 - \kappa_i\Delta\gamma$. After partitioning and simplification, the integral in Equation 2.2 is transformed to the following sum:

$$I(b) \approx \sum_{i=0}^n (c_i\kappa_i\Delta x \prod_{j=0}^i (1 - \kappa_j\Delta x)) \quad (2.3)$$

Equation 2.3 can be, in turn, expressed as a set of blending operations that incrementally solves the ray casting integral along a single viewing ray:

$$c_{dst} = c_{dst} + (1 - a_{dst})c_{src} \quad (2.4)$$

$$a_{dst} = a_{dst} + (1 - a_{dst})a_{src} \quad (2.5)$$

where a_{src} and c_{src} are the opacity and color of the source, respectively, and a_{dst} and c_{dst} are the opacity and color of the destination.

While scattering models are not considered in this volume rendering integral, they can be approximated by applying local illumination models, such as *Phong* [38] or *Blinn-Phong* [39] models. This section only presents a brief derivation of the blending methodology (Equations 2.4 and 2.5) from the radiance differential (Equation 2.1); many notable assumptions have not been discussed in detail. Interested readers are directed to extensive literature that discusses both the above derivation and its alternatives [37, 40-43].

2.4.2 Volume Ray Casting

Volume ray casting is the most common implementation of the discrete DVR process given by Equation 2.3. The volume ray casting procedure sequentially consists of the following steps, as defined by Engel et al. [40]:

1. **Data traversal.** The positions where voxels will be sampled are determined.
2. **Sampling.** The voxels are sampled at the chosen positions. The sampling points typically do not correspond to discrete grid points and interpolation is performed to reconstruct the voxel value (intensity).
3. **Gradient computation.** The gradient of the sampled voxel values is calculated with additional sampling of neighborhood voxels. This gradient is the part of input to step 5.
4. **Classification.** The voxels are mapped to color and opacity values. This classification is used to visually distinguish structures in the volumetric image.

5. **Shading and illumination.** Shading and illumination effects are typically applied to enhance the visual appearance of the structures, e.g., increasing the impression of 3D by gradient-based shading.
6. **Compositing.** The pixels of the final visualization plane are computed by compositing the optical properties of the voxels along rays based on the volume rendering integral.

Volume ray casting can be intuitive and efficiently implemented in parallel on GPU architectures due to the separable ray-by-ray evaluation in the volume rendering integral [14-16, 44]. In the volume ray casting procedure, the compositing and classification steps are particularly important for the visual quality of the final visualization. The compositing step constitutes the optical foundation of the procedure; the contribution discussed in Chapter 4 is related to this step. The optical property mapping through classification will be addressed in Chapters 5 and 6. Further explanation of the other steps in volume ray casting is beyond the scope of this thesis but they are all active research areas.

2.5 Transfer Functions

Volume ray casting relies on the optical classification of the data. However, most medical imaging data are greyscale and do not hold information about the color and opacity values of structures to be visualized. Instead, a classification interface, which is known as the Transfer Function (TF), provides a mapping for voxel attributes into color and opacity values (cf. c_i and κ_i in Equation 2.3). The major role of TF is to allow the user to control what is shown and how it should appear. Realistic coloring is not a necessary objective. Rather, optimal visual separation among structures is the typical goal. The most typical way to work with TFs is through representative presets with the option of manual optimization [8].

In a typical scenario, a user selects an intensity range that corresponds to a certain structure, and then assigns the optical values for the structure to be used in the volume ray casting procedure. In general, the structure classification capability of a TF depends upon the attributes of the raw data and how they are considered. A greater number of attributes tend to lead to greater classification capabilities. The space constructed by the attributes is referred to as the TF space or the classification space.

2.5.1 Pre- and Post-classified TF

Classification from TFs (color and opacity mapping to structures) is most often applied after the sampling step of the volume ray casting procedure; this type of TF is known as post-classified TF. Alternatively, the classification can also be applied to discrete grid points prior to the sampling step; this type of TF is known as pre-classified TF. Under pre-classified TFs, the mapped optical values are interpolated, instead of the voxel value. This may result in noticeable artifacts and overly blurry final visualizations [13]. For these reasons, pre-classified TFs are used less frequently than post-classified TFs.

2.5.2 One-dimensional Transfer Functions

Figure 2.9 illustrates a standard 1D TF for CT imaging data; the horizontal axis represents the range of the intensity values while the vertical axis dictates the corresponding opacity values. In the TF space, a control line (red) is overlaid on a background showing the intensity histogram of the data (grey bars in the x-axis). The central role of the histogram is to detect and categorize structures through identifiable peaks and valleys. The peaks and valleys for certain structures, such as the lungs and muscle tissues, tend to be consistent across images and can be observed directly. In this figure, the control line is assigned to two opacity peaks with different colors; the first blue peak corresponds to the lungs and the second red peak to the muscles.

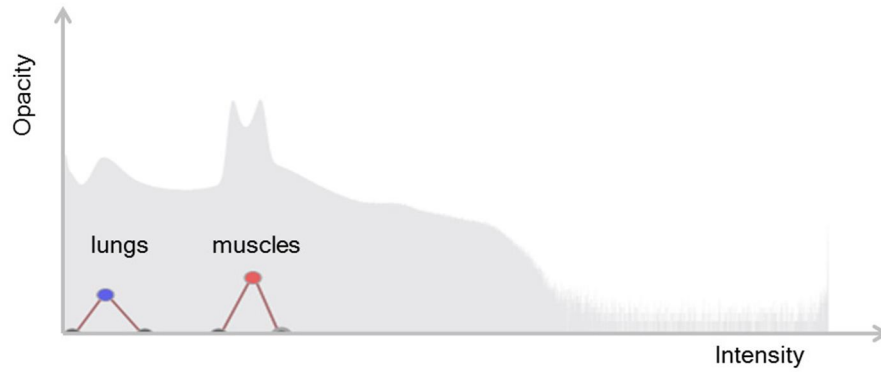


Figure 2.9: A standard 1D TF.

2.5.3 Multi-dimensional Transfer Functions

The 1D TF space can be extended to higher dimensions to improve the classification among different structures. Figure 2.10 shows a 2D TF [45] where the x- and y-axes correspond to the intensity and the gradient magnitude for the data, respectively. In the 2D TF, opacity and color are typically defined only through visual geometries on the TF space due to the y-axis dedicated to an attribute (gradient magnitude). Any TF with more than two attributes is referred to as a multi-dimensional TF. A major challenge with multi-dimensional TFs is the increased manipulation complexity that comes from the extended classification space.

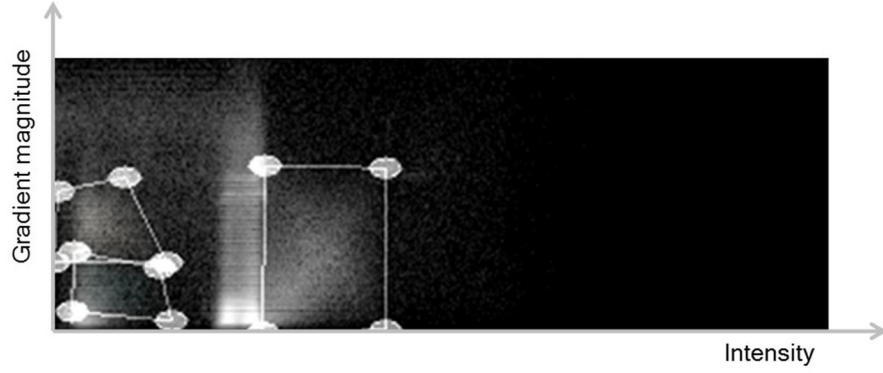
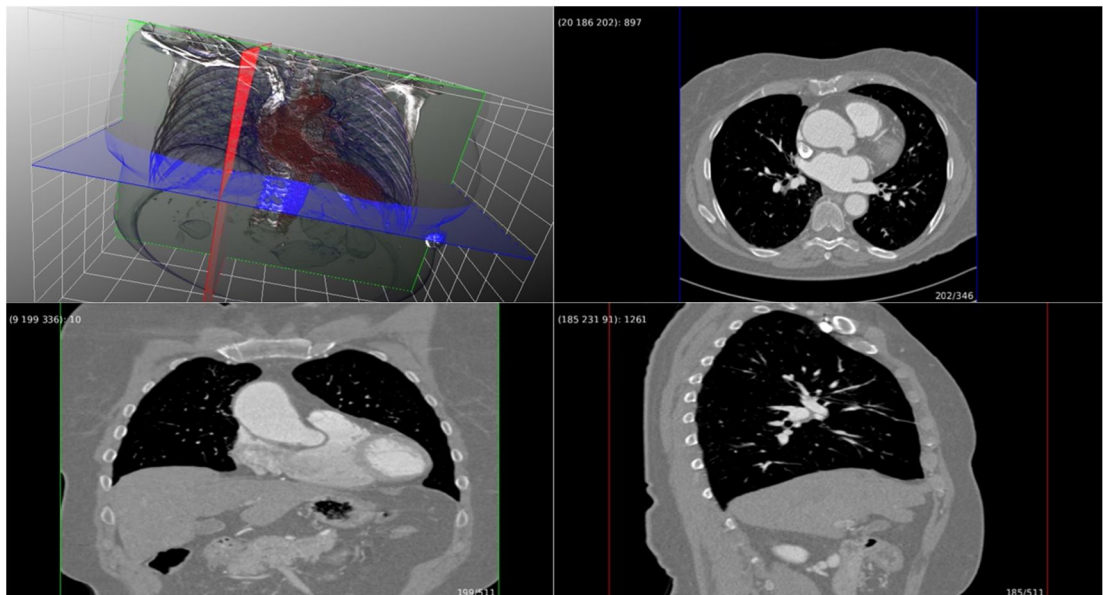


Figure 2.10: A multi-dimensional intensity-gradient-based TF. The 2D TF is used to improve the classification capability at the cost of interaction complexity.

2.6 Fused Volume Visualization for Multi-modality Images

Complementary information from multi-modality images can be fused at different steps of the volume ray casting procedure. Cai and Sakas [46] proposed three different types of data intermixing at the: illumination, accumulation (compositing), or image level. The intermixing at the illumination and accumulation levels is performed during the volume ray casting procedure while the image level intermixing blends the rendered visualizations. The illumination level intermixing uses a single illumination model for all imaging data. On the other hand, separate illumination models are applied at the accumulation level intermixing.

3. Datasets and Visualization Environment



A quadrant view of a high-resolution CT study of torso

3.1 Datasets and Pre-processing

In this thesis, a variety of medical imaging modalities, including single-modality high resolution CT and MR, and multi-modality PET-CT, are used to demonstrate the proposed visualization methods. Note that all patients were scanned on their back so the right side of the patients appears on the left of the image (mirror image).

PET-CT studies were acquired from a Siemens Biograph TruePoint PET (with a tracer fluorine-18 fluorodeoxyglucose)-CT scanner (Siemens Medical Solution, Hoffman Estates, IL, USA) at the Department of Molecular Imaging, Royal Prince Alfred Hospital, Sydney, Australia. All studies had 326 slices with slice thickness of 3 mm, covering the whole body from the top of the head to the upper thighs. PET image slices were reconstructed to 168×168 pixels at $4.07 \text{ mm}^2 / \text{pixel}$, and CT slices were reconstructed to 512×512 pixels at $0.98 \text{ mm}^2 / \text{pixel}$. The hardware co-registered PET was then resampled to the CT dimensions. The CT scans were processed to remove the background and bed/linen artefacts via adaptive thresholding and image subtraction from a bed template [47]. The voxel intensity of the CT was in Hounsfield Unit (HU) scale with intensity ranging from -1000 (air) to about +2000 (bone/contrast media); this was mapped to 0 to 4095 (12 bits) for rendering. For PET, a linear intensity normalization was applied to match the 12 bit intensity range of the CT.

Four T1-weighted brain MR studies were obtained from the open access series of imaging studies (OASIS) [48]. These studies had 128 slices at 1.25 mm thickness; each slice had a resolution of 256×256 pixels at $1.0 \text{ mm}^2 / \text{pixel}$. We also used a high-resolution CT study of the head from Osirix [49], which had 260 slices at a resolution of 512×512 pixels at $0.49 \text{ mm}^2 / \text{pixel}$. The intensity ranges of all the studies above were linearly mapped to 0 to 4095 prior to rendering.

3.2 Visualization Environment

All visualizations in this thesis were performed using a PC with nVIDIA GTX 590 1.5G GPU, Intel i7 CPU @ 3.20 GHz, and 64-bit Windows 7 Operating System. We used the GPU optimized Voreen [50] as an implementation platform. Voreen is a rapid-prototyping environment for GPU-based volume visualization. Voreen is an open source C++ framework consisting of processors-autonomous functional components each of which performs a specific task. The component-based architecture allows the users to exploit the realized techniques in interactive visualization applications without any performance penalty. The users can flexibly combine the processors into data-flow networks. Different volume rendering and image processing techniques are implemented as built-in processors. Voreen also supports several file formats for volume data, e.g., Digital Imaging and Communications in Medicine (DICOM), Tagged Image File Format (TIFF), or raw voxel volumes. The users are able to easily control the properties of processor, e.g., rendering parameters, through automatically generated Graphical User Interfaces (GUIs).

Another key benefit of using Voreen is the flexibility of integrating new algorithms and optimizations. Figure 3.1 shows one of the proposed visualization methods implemented in Voreen. A substantial number of new visualization methods have already been developed using Voreen and their usefulness has been demonstrated for various application domains, including medical domain [51-54].

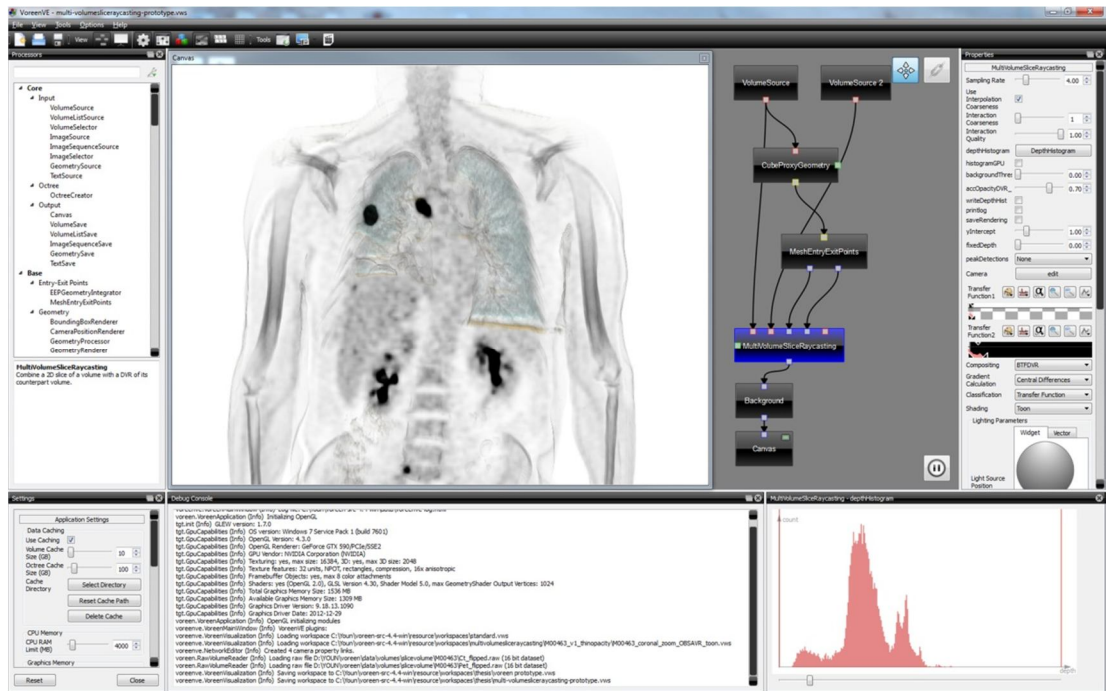


Figure 3.1: The component-based GPU visualization framework of Voreen showing one of the proposed visualization methods. We developed the proposed visualization methods by developing new *processor* components, in this case, MultiVolumeSliceRaycasting, and also by optimizing existing processor components.

4. Augmentation of 3D Contextual Information on 2D Medical Image Slice Views



Augmentation of 3D vascular structures on 2D CTA image slice

This chapter describes an alternative to 2D cross-sectional view planes which automatically augments 2D slice of interest (SOI) with the relevant 3D structural context without impairing the view of the SOI. In the conventional 2D methods, the users rely on their mental reconstruction to obtain the contextual information. The difficulty of such mental reconstruction is especially obvious when medical image volumes are used for the diagnosis of disease in which its 3D spatial localization and relationship with the surrounding structures are the primary feature that needs to be analyzed and visualized. The key capabilities of the approach are demonstrated in its application to multi-modality positron emission tomography and computed tomography (PET-CT) image volumes. The clinical utility of this approach is also evaluated by conducting a user study with a clinical expert. It led to the following publications:

- **Y. Jung**, J. Kim, M. Fulham, and D. Feng, "Occlusion-based volume rendering augmentation for slice of interest (SOI) visualization," *Computer Graphics International*, short paper, 2014.
- **Y. Jung**, J. Kim, M. Fulham, and D. Feng, "Opacity-driven volume clipping for slice of interest (SOI) visualization of multi-modality PET-CT volume," *IEEE Engineering in Medicine and Biology Society*, pp. 6714-6717, 2014.
- **Y. Jung**, J. Kim, M. Fulham, and D. Feng, "Occlusion-based slice of interest (SOI) augmented with volume rendering for PET-CT visualization," *IEEE Transactions on Visualization and Computer Graphics*, under revision, 2015.
- **Y. Jung**, J. Kim, M. Fulham, and D. Feng, "Volume Rendering Augmentation on Slice of Interest (SOI) For Visualisation Of Thoracic PET-CT," *International Journal of Computer Assisted Radiology and Surgery*, Vol 10 (supplement1), accepted, 2015

4.1 Introduction

Direct volume rendering (DVR) has been used for clinical diagnosis [2, 3]. Most clinical image interpretation, however, still reading two-dimensional (2D) cross-sectional image slices that are analyzed slice-by-slice in transaxial / coronal / sagittal planes, and this approach is referred to as cross-sectional view planes. Figure 4.1 shows an example of a positron emission tomography (PET) and computed tomography (CT) dataset in cross-sectional planes. PET-CT is a dual-modality imaging technology where PET is combined with CT in a single device. PET-CT is routinely used in the evaluation of malignancy, in particular, in staging disease and in the assessment of response to treatment [27]. PET-CT enables the visualization of pathophysiological function with PET on an anatomical template provided by CT. Importantly PET can detect sites of disease in structures that do not appear abnormal on CT. Ideally for PET-CT visualization, a region of interest (ROI) on PET, such as a tumor, is shown while the underlying anatomy from CT is preserved, without compromising the focus of interest, to provide precise localization of the tumor. Although it may seem counter-intuitive, the effective assimilation and visualization of these two large data volumes are non-trivial.

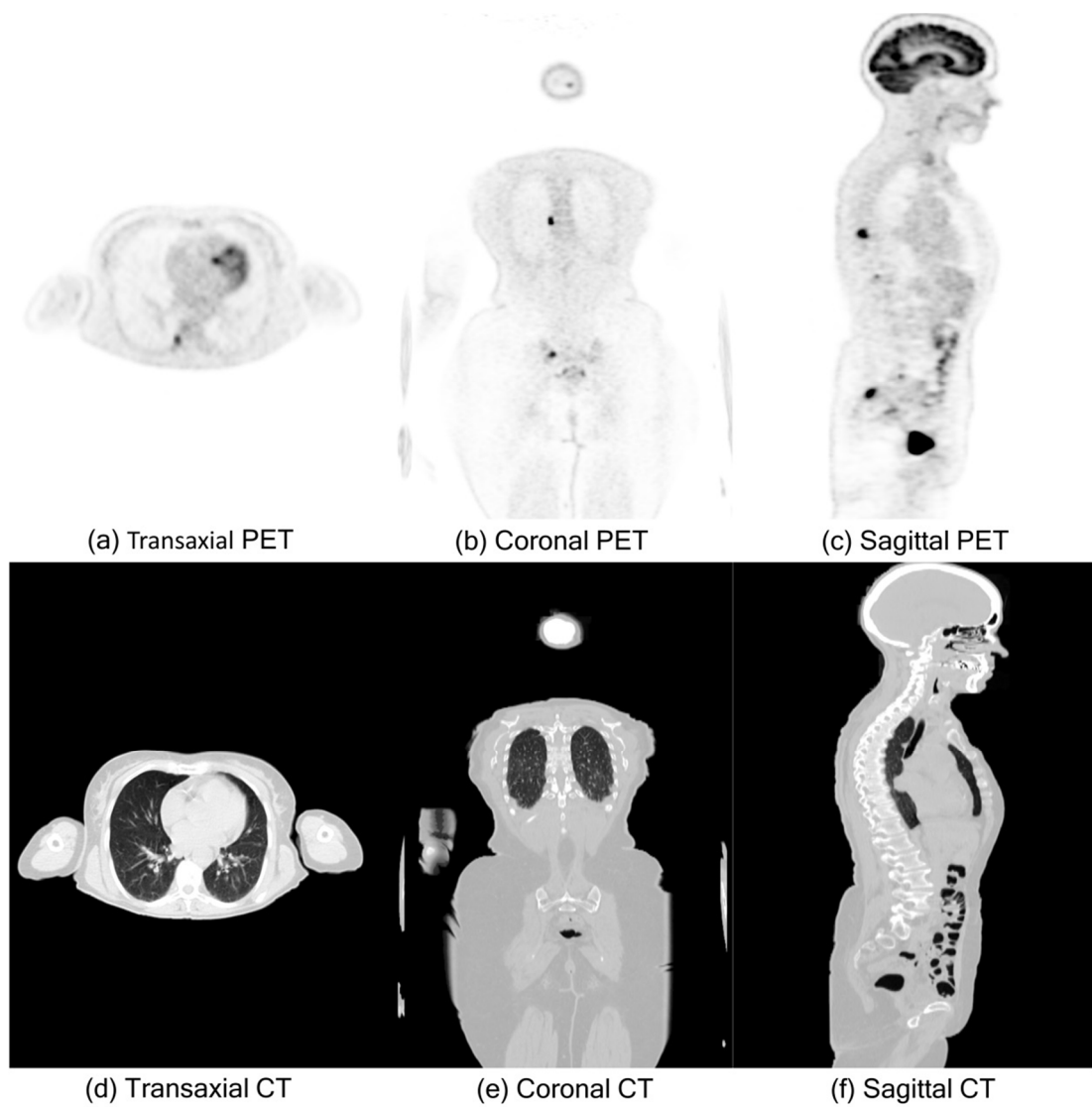
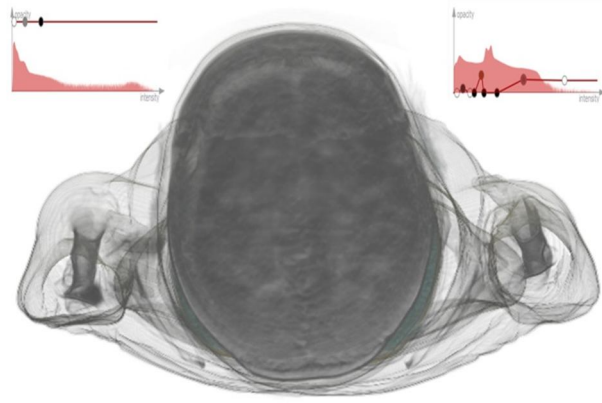


Figure 4.1: Cross-sectional view planes of PET-CT data of a patient with disseminated lung cancer with skeletal metastases. The PET (top) and CT (bottom) are individually rendered in cross-sectional views: transaxial (left column), coronal (middle) and sagittal (right) views. An inverted gray-scale 1D TF was applied to PET whereas a normal gray-scale TF was applied to CT.

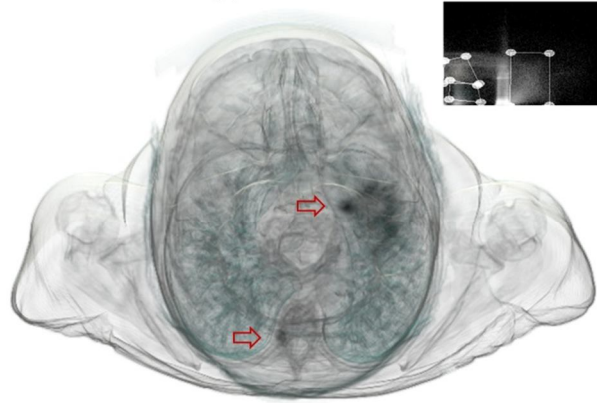
DVR can display the entire volumetric dataset across multiple dimensions and a specific ROI such as a tumor in a PET image volume is readily discerned relative to surrounding structures. The reasons for the lack of a more generalized use of volume rendered images in

routine clinical image reading are complex and they relate to the established habits of image readers, the occlusion inherent to volume rendering where some structures can be obscured and a lack of suitable easy-to-use software. These limitations are exacerbated when more than one modality is used as shown in Figure 4.2(a) where a DVR of a PET-CT data is visualized in a transaxial view. All the body structures from the PET-CT volumes are rendered in the order of its distance to a view-point and therefore, ROIs such as lesions from the PET data are occluded by the structures that are closer to the view-point. Volume clipping is a common approach to remove unwanted objects that may occlude a ROI in DVR. The clipping cuts away the obstructing elements of the volume but its major drawbacks are the time taken to select the right depth to cut and then the information that is lost from the clipped volume. This data loss can remove valuable contextual cues.

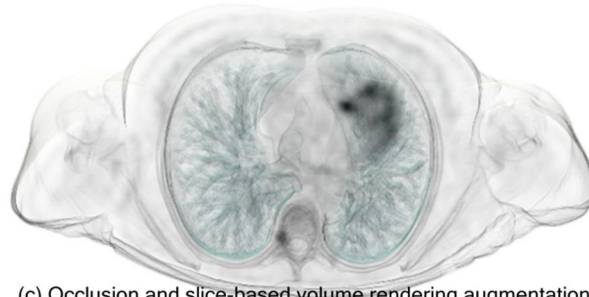
An alternative approach to rendering the PET and CT image volumes simultaneously is to augment a DVR of the CT image volume onto a 2D slice of interest (SOI) of the PET image volume, which we refer to as slice-based volume rendering. This can localize 2D pathophysiological information within a 3D anatomical context and thus provide additional visual *cues*, for the localization of the critical lesions and their relationship to adjacent structures, as shown in Figure 4.2(b). This slice-based volume rendering, however, inherently occludes the ROI, e.g., in Figure 4.2(b) the skull on CT is occluding lesions in the PET slice (see arrows). A common approach to reduce occlusion in DVR is to apply a transfer function (TF) that allows the user to manipulate opacity and color of the voxels in an image volume. The TF can control the amount of volumetric occlusion to the ROI. Conventional one-dimensional (1D) or multi-dimensional TFs [55-58], however, can only be applied to the entire volume and not to individual structures and therefore it is difficult to localize the ROI within a volumetric context.



(a) DVR of PET-CT



(b) Slice-based volume rendering of PET-CT



(c) Occlusion and slice-based volume rendering augmentation of PET-CT

Figure 4.2: Different volume rendering visualizations applied to PET-CT image volumes in transaxial views. In all the renderings, the same inverted gray-scale TF (top-left in (a)) was applied to the PET and a 1D or 2D TF was applied to the CT. In (a) the PET PET-CT image volumes are simultaneously rendered with a 1D TF for CT (top-right); in (b) a SOI of the PET is fused with the DVR of the CT with 2D TF on CT (top-right); and in (c) the same data and TF as in (b) but with our visualization, which enhances the 3D contextual cues from the

DVR of the CT, which is relevant to the ROIs in the PET slice, such as lesions, (see red arrows in (b)) while also preserving its visibility.

Newly developed semi-automated TFs improve localization of ROI, but they still typically demand additional pre-processing of the image volume, for example, labeling the ROIs (image segmentation) prior to rendering [59, 60]. Instead of manipulating the TFs, occlusion may be removed by identifying and enhancing the most important elements of the image volume to be rendered during volume ray casting using approaches such as maximum intensity difference accumulation (MIDA) [61] and depth-based feature enhancement (DFE) [62]. These ray casting based DVR approaches are also applied to the entire image volume and therefore cannot ensure that the ROIs remain visible.

The current work suggested in this chapter was motivated by the need to present complex clinical imaging data, such as PET-CT, in a format that is more intuitive and easy to assimilate by the medical imaging specialist, other clinicians involved in patient management and by patients themselves. Hence we propose a new visualization approach that augments the SOI from a PET volume with volumetric contextual information derived from the DVR of the counterpart CT volume. Our approach uses the occlusion information derived from the CT voxels in front of the PET slice to automatically calculate an *augmentation depth* parameter and we refer to it as OSVRA for occlusion and slice-based volume rendering augmentation. During the depth computation, we take advantage of voxels that belong to the same CT structure and are likely to have consistent intensity and opacity values, and thus can be grouped into an occlusion distance histogram. This enables the occlusion information of voxels to be analyzed at a structure-level rather than at a voxel-level. The depth parameter is used to derive a weight function that controls the amount of augmentation produced by the DVR of the CT to provide 3D contextual cues without impairing the visibility of the slice. In this process, all ROIs that are present in the slice are

preserved. Figure 4.2(c) shows our visualization where the slice is clearly visible and unnecessary structures, e.g. skull, brain, and spine, are removed when compared to Figure 4.2(b).

We evaluated the approach in a large group of multi-modality PET-CT patients with non-small cell lung cancer (NSCLC) of varying stages and complexity and lymphoma. We also conducted evaluation of its performance when compared to two ray casting based DVR approaches that rely on occlusion information in the rendering, MIDA [61] and DFE [62]. The two approaches have been upgraded to support multi-modality image data.

4.2 Related Work

In the following paragraphs we outline the relevant developments in ROI-based visualization, volume clipping / ray casting and multi-modality visualization that are pertinent background for our work.

4.2.1 ROI-based Visualization

ROIs in volume visualization provide points of focus and therefore allow the users to prioritize their viewing process. Viola et al. [63] introduced an importance-driven volume rendering where an *importance* value was assigned to the pre-segmented ROIs. The importance assignment was used to generate a cut-away view, which revealed important ROIs by reducing the occlusion of contextual regions that were assigned a lower importance value. Burn et al. [64] divided areas surrounding the ROIs into three clusters of importance for rendering. Diaz et al [65] used the region growing algorithm to manually annotate volumetric structures that were then embedded onto a ROI of the same image volume. Other investigators used context-preserving volume rendering [66] and distance-based TF approaches [67, 68] with rendering environment parameters, such as with lighting and

viewing distances to enhance the contextual information. The occluding structures were ghosted and/or faded to reveal the underlying ROIs. In these approaches, segmentation of ROI was a necessary pre-process and the selection of ROIs and assignment of importance values were manually defined.

4.2.2 Volume Clipping

Volume clipping is an interactive technique that is used to navigate a 3D image volume by cutting away parts of the image volume to inspect the internal components. It is achieved by defining a clipping plane, moving it through the image volume, and removing parts of the image volume on a pre-defined side of the plane. Rectangular planes are typically used but more complex clipping geometries may be applied as reported by Weiskopf et al. [69] and Islam et al. [70]. The other approaches have improved the usability of volume clipping by incorporating additional information from an anatomical atlas, to allow the user to adaptively place axis-aligned clipping planes [71], a deformable clipping plane to perform virtual resections [72], and editable clipping planes to create custom cross-sectional views [73]. These approaches employ sophisticated methods to select the clipping plane, however, their main drawback is the inherent loss of contextual information from the clipped image volume that may result in misleading visualizations and confusion [4]. Birkeland et al. [74] recently used an elastic *membrane* to reduce the visual loss of contextual information. The membrane was guided by the definition of a *potential field* and adapted to the anatomical structures in the neighborhood of a clipping plane. This approach, however, required that the boundaries of the structures were well-defined and the indirect manipulation of a complex deformable membrane plane was carried out through non-intuitive and time-consuming parameter tweaking where intensive user involvement was required.

4.2.3 Volume Ray Casting

The general concept of volume ray casting has been discussed in Section 2.4.2. In this Section, we outline the recent developments of volume ray casting to improve DVR visualization. The key strength of volume rendering lies with volume ray casting that allows a visualization to depict an entire image volume at once. In this way, the optical contributions of every voxel along viewing rays are accumulated to the final visualization, subject to the optical mapping by TFs. Recently, the MIDA approach proposed by Bruckner et al. [61] used the maximum intensity values in each of the viewing rays to adaptively control the accumulation of the optical values along the rays. This control allowed contextual cues in front of a structure with the maximum intensity value to be better preserved when compared to the traditional DVR approach. Liang et al. [75] extended single structure maxima in MIDA to support multiple local maxima corresponding to structures identified along a ray. Marchesin et al. [76] defined a gradient-based relevance function to quantify the relative importance of each voxel to the final visualization. The function was integrated to volume ray casting to ensure that contributions from all the voxels (structures) were rendered according to importance. Pinto et al. [77] generalized the relevance function with other attributes derived from voxels e.g., a silhouette or a shading level. Similarly, Tang et al. [62] proposed DFE that assigned a distance-based opacity function (weight) to voxels in the ray such that the occlusion of the voxels closer to the view-point were reduced; this enabled all the voxels in the ray to contribute to the final rendering. These DVR approaches modified the opacity accumulation from conventional volume ray casting to allow multiple structures, such as ROIs, to be displayed in a single visualization. Nevertheless, they cannot ensure that the visualization of the ROIs are retained since the optical contributions of ROIs localized further along the viewing ray may be attenuated by the less important structures preceding them. In the studies by Rezk-Salama et al. [78] and Malik et al. [79][x], volume ray casting analysis has been used to visualize volumes in a *layered* manner. Here, the voxels in a ray were partitioned into layers according to their opacity [78] or their intensity [79] values to

represent different structures. Such analysis allows users to navigate these layers without having occlusions from other layers. These analytic approaches grouped voxels into a layer without spatial coherence and the voxels then had different depth levels to one another. This grouping then prevents them from being applicable to slice-based volume rendering in which all the voxels need to be at the same depth e.g., in the same cross-sectional slice from a volume.

4.2.4 Multi-modality Medical Imaging Visualization

In pioneering work on multi-modality visualization, Rik et al. [80] proposed an integrated volume rendering of co-registered single photon emission computed tomography (SPECT) and magnetic resonance (MR) imaging of brain. This dual-modality visualization allowed depiction of changes in function from SPECT and the anatomy from MR imaging in frontal lobe damage. The MR image acted as a primary visualization, and regions were substituted by corresponding parts from SPECT. Peter et al. [81] generalized the integrated volume rendering with a variety of imaging modalities. Rik et al. [82] further proposed an integrated volume rendering of functional data with surfaces extracted from anatomical data. In recent work, Bramon et al. [83] suggested an information-theoretic approach to automatically select the most *informative* voxels from two overlapping volumes. In these approaches, only one voxel per location was visualized and these approaches were not designed to fuse information available from the voxels in the same location.

There have been many other contributions to multi-modality visualization. Cai and Sakas [46] reported a data intermixing algorithm to fuse multiple image volumes to visualize the information contained in the multiple volumes simultaneously. Hauser et al. [84] proposed two-level volume rendering where structures from each image volume were visualized individually by using different rendering algorithms and the visualizations were then

combined into a single scene. Kim et al [85] used a PET-CT visualization where segmented ROIs from PET were embedded on PET or CT renderings. Kim et al. [58] also reported using a pair of 1D TFs for PET and CT image volumes, in which the resultant visualizations of the two image volumes were intermixed. Alternatively, Haidacher et al. [86] used a 2D fused TF space (with a single value and a single gradient magnitude as parameters) based on the information contained in the distribution of voxel values in both input image volumes. A measure for the complementary information of both image volumes was used for a better separation of different structures. Unfortunately, the TFs in these approaches were applied to the entire image volume and it was often difficult to obtain an appropriate TF to visualize a specific ROI while maintaining the details of surrounding structures. Furthermore, such approaches relied on the availability of the ROI, which usually involved pre-processed segmentation of the ROI.

4.3 Methods

4.3.1 Overview

Our method has six steps as shown in Figure 4.3. In (a), in the initial step, a SOI (255th slice) from a PET image volume is selected by the user. Using the concept of opacity accumulation in volume ray casting, we compute the *occlusion distance* of each sample in the SOI (see the red arrows in (b)), which is the distance where CT information relevant to each sample is maximally visible without impairing its view; here, the CT image volume is represented by a cube. Pre-defined TFs for the PET and CT image volumes are used: in PET, the TF reveals the abnormal structures and in CT, the TF depicts the anatomical structures. The same TFs as shown in Figure 4.1(a) were applied instead. In (c), we construct a map to represent the occlusion distances of every sample in the SOI (rendered in green). Prior to the mapping, the background samples are removed. In (d) the creation of a histogram for the occlusion distance map, which is then used to calculate the augmentation depth parameter (D) is shown.

This parameter controls the amount of CT DVR to be rendered while avoiding the occlusion of the SOI. As a default, the first peak of the histogram is used; in this figure it is set to $D = 33$. We then generate an opacity weight curve with shape of a logistic function using D as its inflection point as in (e). This curve is then used with the CT TF to improve the contextual cues from the CT DVR in a way that emphasizes the relevant anatomy before D as well as de-emphasizing other structures occurring after D . The CT image volume is rendered with the CT TF and the derived opacity weight curve and is then embedded onto the PET SOI. In (f) the resulting visualization is shown; it enables augmentation of the lung tissues and bony structures in the form of the 3D spatial cues while minimizing the obtrusiveness to the view of the SOI (see lesions in the lung and pelvis). The figure shows an equal amount of visual information between the PET slice and CT DVR, commonly referred to as the 50 percent fusion ratio between the two renderings.

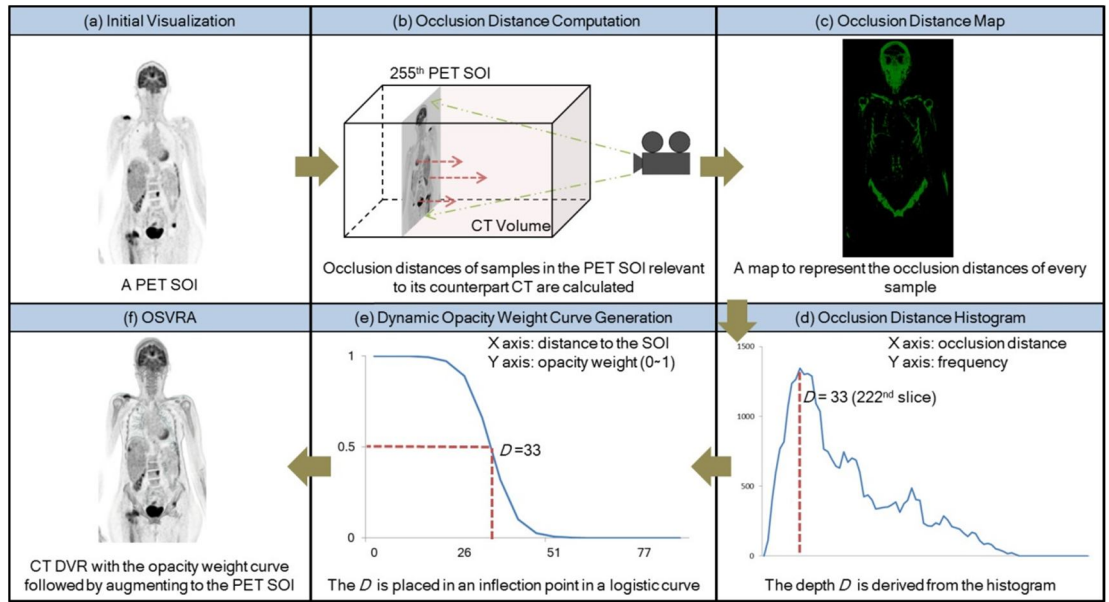


Figure 4.3: An overview of the OSVRA with PET-CT image volumes.

4.3.2 Occlusion Distance Histogram Generation and Augmentation Depth Computation

We adopted the concept of opacity accumulation in back-to-front volume ray casting for computation of the depth D . Each sample from a PET SOI casts a ray to the view-point. The opacities of CT voxels along these rays are then accumulated according to:

$$a_i = (1.0 - a(s(i))) \times a_{i-1} + a(s(i)) \quad (4.1)$$

where a_{i-1} is the accumulated opacity, $s(i)$ is the intensity value of the i^{th} voxel of the CT image volume along the viewing ray, and $a(s(i))$ is the opacity value of the i^{th} voxel, defined by a TF. Once the accumulated opacity's contribution becomes negligible (reaches the fusion ratio), the ray is terminated and the Euclidean distance from the terminated ray to its sample location is then calculated as the occlusion distance.

The voxels belonging to the same structure are expected to have consistent values (intensity and opacity accumulation), meaning that the occlusion distances of rays casted from the structure should have similar values. This permits grouping of these voxels for structure-level, rather than voxel-level, analysis. The voxels are then used to compute an occlusion distance histogram.

Figure 4.4 shows the construction of the occlusion distance histogram for structure-level depth analysis. In this example, all voxels belong to one of 3 structures S_1 , S_2 , and S_3 , and we consider S_1 to be a ROI. The voxels are then used to compute the occlusion distance histogram with three peaks representing different distances D_1 to D_3 . Different structures are emphasized in the final visualizations depending on the selection of the D . In D_1 (first peak), structure S_1 is rendered fully while S_2 is rendered partially. With D_2 (second peak), S_1 and S_2

are fully visualized while some of the renderings from S_3 are visualized, thereby partially occluding S_1 and S_2 . Although D_3 (third peak) allows all the structures to be visualized, the rendering of S_3 prevents the other structures from being visible. Our computation will automatically select D_1 , which typically corresponds to the group of voxels that are identified to the same CT structures and have the closest distance to the SOI. We integrated a user interface into our visualization to enable users to select other peaks from the occlusion distance histogram (see Figure 4.8).

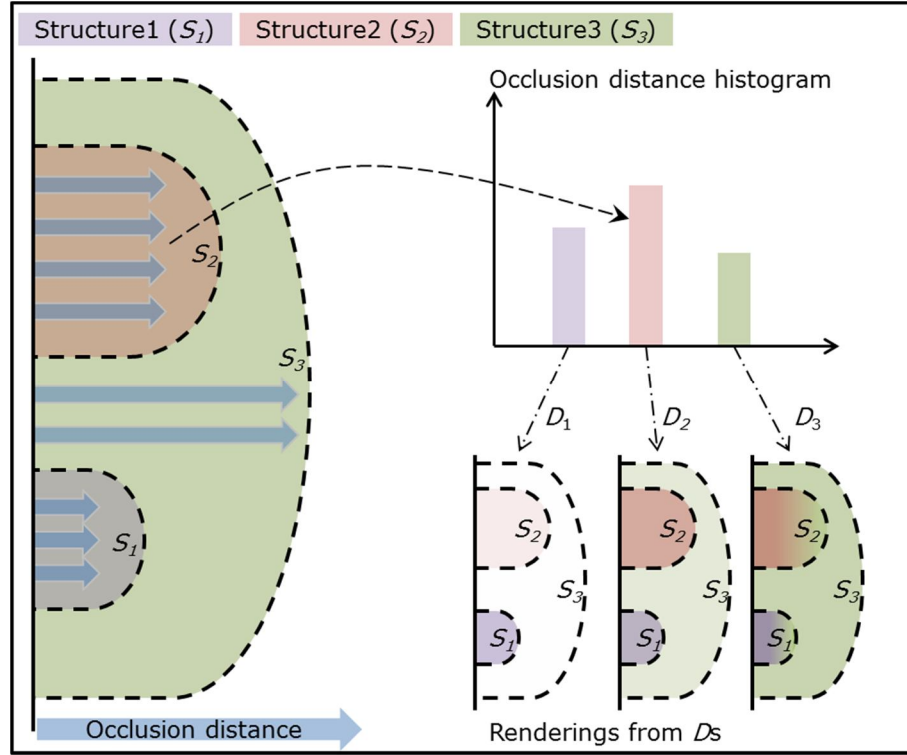


Figure 4.4: Construction of the occlusion distance histogram allows for structure-level depth D analysis.

4.3.3 Dynamic Generation of Opacity Weight Curve

An opacity weight curve was generated based on the calculated D with a logistic function as illustrated in Figure 4.5. We adopted a logistic function from Hay et al [87], which is a

sigmoid S shape where the initial stage of growth is approximately exponential and as saturation begins, the growth slows; at the end, the growth stops. We used Y-axis inverted logistic function as the opacity weight curve, which enabled the preservation of the contextual information by adding the information further from D as a compensation for the loss of the information prior to D . The location of D is used as the inflection point (I) and used to calculate the curve:

$$f(x) = \frac{C}{(1+Ae^{Bx})} \quad (4.2)$$

where x is the distance to a SOI, A and C represent the opacity weight range, and B is calculated as $(\ln A)/D$. We empirically set A to 0.0001 (the minimum weight value) and C to 1.0 (the maximum weight value) to ensure that all structures could contribute to the final visualization depending on the distance from the SOI.

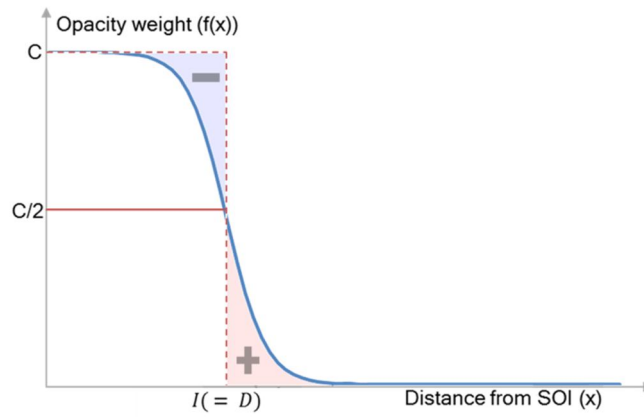


Figure 4.5: Opacity weight curve generation based on a logistic function.

4.3.4 Fusion of a PET SOI and a CT DVR

We integrated the opacity weight curve (Section 4.3.3) to back-to-front volume ray casting to adjust the optical contributions of the voxels from a CT image volume, based on the distance to a SOI of its counterpart PET image volume as follows:

$$c_i = (1.0 - a(s(i)) * w(d_i)) * c_{i-1} + c(s(i)) * a(s(i)) * w(d_i) \quad (4.3)$$

$$a_i = (1.0 - a(s(i)) * w(d_i)) * a_{i-1} + a(s(i)) * w(d_i) \quad (4.4)$$

where c_{i-1} is the accumulated color, $c(s(i))$ is the color value of the i^{th} voxel (defined by a TF), d_i is the Euclidean distance of the i^{th} voxel to the PET SOI, and $w(d_i)$ is the modulation coefficient from the opacity weight curve. Volume ray casting of the CT image volume was performed in the same way as in the occlusion distance computation, together with the derived opacity weight curve. Resulting CT rendering was augmented onto the PET SOI by applying voxel-level intermixing (fusion) [46]. An equal fusion ratio was used to ensure that the resulting DVR and the SOI contributed equally to the final visualization.

4.4 Implementation

Real-time performance for our approach was achieved by using the programmability and massive parallelism of the modern graphics processing units (GPUs). In the following sections and Figure 4.6, we explain how our proposed occlusion distance map and histogram can be computed efficiently using a two-pass execution in GPU to avoid the computer intensive execution on the CPU.

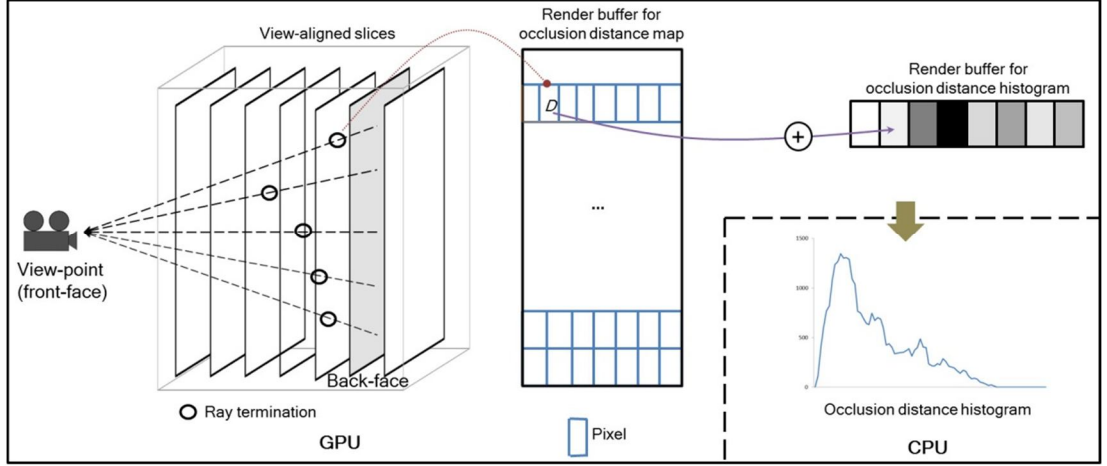


Figure 4.6: Efficient computation of the occlusion distance map and resulting histogram, using parallel GPU architecture.

4.4.1 Occlusion Distance Map Generation

A 2D PET SOI was used as a back-face for volume ray casting. In the fragment shader, samples from this back-face cast rays to the front-face of the view-point with the opacity values of the CT voxels along the rays being accumulated according to Equation 4.1. Once the accumulated opacity reached the fusion ratio between the two image volumes, ray traversal was terminated (see black circles in Figure 4.6). The occlusion distances of the terminated rays to the back-face were then transferred to the corresponding pixel in a 2D graphical render buffer that was read back to the CPU.

4.4.2 Occlusion Distance Histogram Generation

We exploited the scattering operation of the vertex shader that was reported by Scheuermann and Hensley [88]. The occlusion distance map was initially loaded as a 2D texture. Point primitives were generated by the vertex shader (one per pixel texture) and then translated to the corresponding bins in a 1D graphical render buffer. Using the hardware-supported fusion

operation of the fragment shader, all the distance contributions translated from the 2D texture were accumulated, and the resulting 1D histogram was transferred to the CPU.

4.5 Results

We applied our approach to 6 patient studies, where the underlying diagnosis was NSCLC and lymphoma, to render the figures presented in this chapter. For the clinical domain expert user study, we used another set of 46 patient studies with NSCLC at varying disease stages that included regional nodal disease in thorax and more widespread metastatic disease outside the thorax. NSCLC was chosen because of the importance of accurate staging on patient management. Stage I and II disease, where mediastinal lymph nodes are not involved, can be treated effectively with surgery. Stage III is generally treated with a combination of chemotherapy and radiotherapy or chemotherapy and then surgery, if the mediastinal nodal disease is confined to the thorax and is ipsilateral to the primary tumor. In Stage III the accurate delineation of the regional nodal disease is critical for surgical and radiotherapy planning. The depiction of the sites of disease on PET relative to the adjacent anatomy offered an opportunity to assess the utility of our approach.

In the Result section, all visualization results were made with a single default CT TF definition, (as in Figure 4.2 (a)) in which the lungs and the bony skeleton were emphasized more than the skin tissues and the lung boundaries; the TF setting can be readily adjusted, either in 1D- or multi-dimensional variants [56, 57] by manipulating the opacity values corresponding to each of the structures for emphasizes, as consistent with the process in existing literatures [8, 55, 89].

4.5.1 OSVRA Visualization

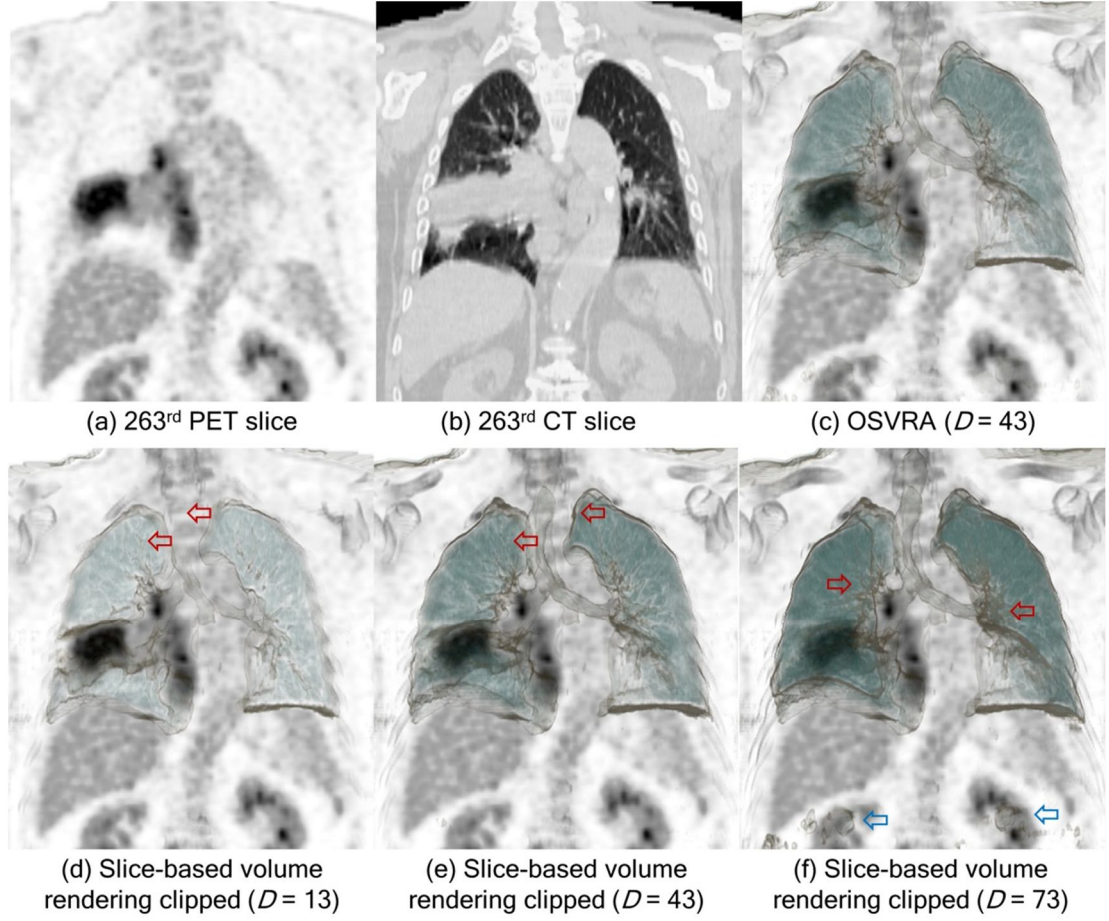


Figure 4.7: An example of our OSVRA and conventional slice-based volume rendering with manual clippings at various depths. A PET-CT study with a large tumor in the right lower lobe of the lung was visualized using both methods. 2D PET and CT renderings ((a) and (b)) are shown as the reference function and anatomical information for the patient study.

Figure 4.7 shows our OSVRA when compared to conventional slice-based volume rendering with manual volume clipping at various depth levels. The objective in this example was to accurately visualize the tumor and its surrounding anatomy. (a) shows the visualization of a tumor on the 263rd PET SOI and (b) shows the visualization of anatomical structures on the corresponding CT SOI without any volumetric augmentation. (c) shows the visualization with OSVRA using the automatically derived depth ($D = 43$) and the opacity weight curve.

In comparison, (d) shows the visualization with a clipped slice-based volume rendering with a thinner depth ($D - 30$) from the SOI in which the details of the lungs and also the trachea (indicated by red arrows) were less visible, suggesting that too much volume was clipped. In (e) the slice-based volume rendering was set to the same depth (D) calculated by the OSVRA as in (c); and (f) shows that the thicker depth ($D + 30$) produced strong occlusion from the outer parts of the lungs and it subsequently occluded the view of the tumor and the lung parenchyma adjacent to the midline representing respiratory bronchioles and bronchi, (indicated by red arrows). The resulting visualization also rendered irrelevant sub-diaphragmatic bowel, overlying the kidneys, to the slice (indicated by blue arrows). In (e), we note that simply using the D was able to produce relatively good visualization when compared to (d) and (f) but the overall shape of the lungs was not clearly portrayed when compared to OSVRA (see arrows indicating the parts of the volume that were clipped). This also demonstrates the importance of automatic generation of the weight function that was applied in the OSVRA, which in this example, allowed only the adjacent structures to be depicted in the resulting visualization. This demonstrates the importance of selecting the right depth for volume clipping. Selection of the correct depth relies on tedious tweaking of the depth (slice) position until a desired visualization is found e.g., several minutes as measured in a single-modality tooth CT data with volume dimension of 256^3 [90].

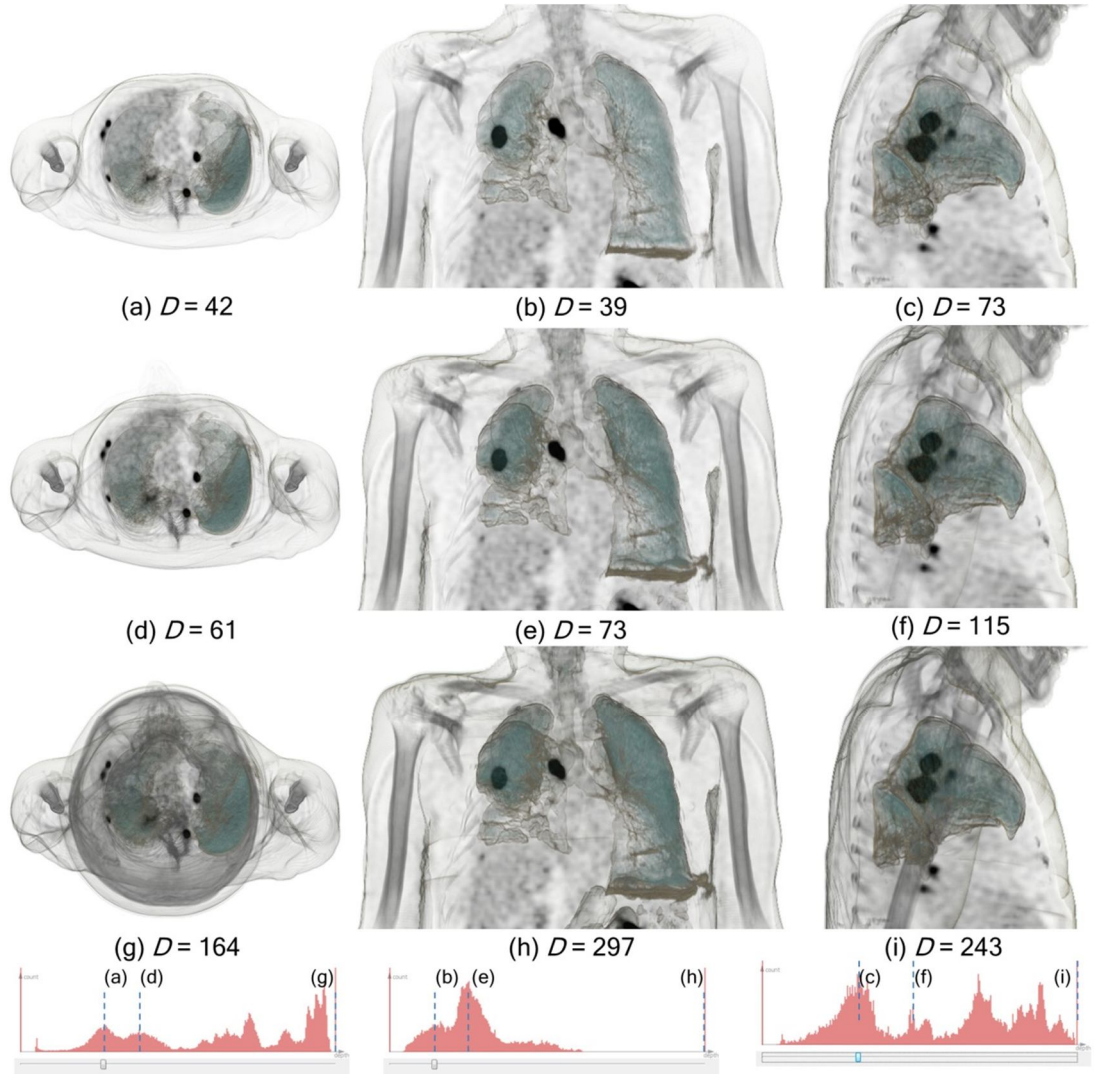


Figure 4.8: OSVRA results using various D values. The first three rows correspond to the cross-sectional views of PET-CT data at different depth augmentation and the fourth row is the occlusion histograms of the data. In the first row, D was derived from the first peak from the histograms; the second row from the second peak; and the third row from the last peak. Each column depicts different views: transaxial in left column looking from below, then coronal in middle column, and sagittal views in right column. Note a gradual increase in the occlusion of the DVR as the value of D increases.

Figure 4.8 shows the impact of depth D on the amount of augmentation of volumetric context. In the transaxial view of (a), the OSVRA visualization with $D = 42$ derived from the

first occurring peak in the occlusion distance histogram (fourth row) revealed the details of the lung parenchyma. Further lung detail was introduced in the depth ($D = 61$) from the second peak in (d). In (g) with the entire depth ($D = 164$), irrelevant structures, such as the skull outline, were introduced causing unnecessary occlusions to the SOI. Note that the histogram and the depth D were re-computed based on the viewing angles. Consistent with the transaxial views, we can see that the D selections in other two views were an influential parameter that controlled the level of augmentation from the DVR. In all our visualizations, including this figure, we found that the D derived from the first occurring peak in the histograms was an appropriate depth to augment relevant structures onto each SOI without impairing its view.

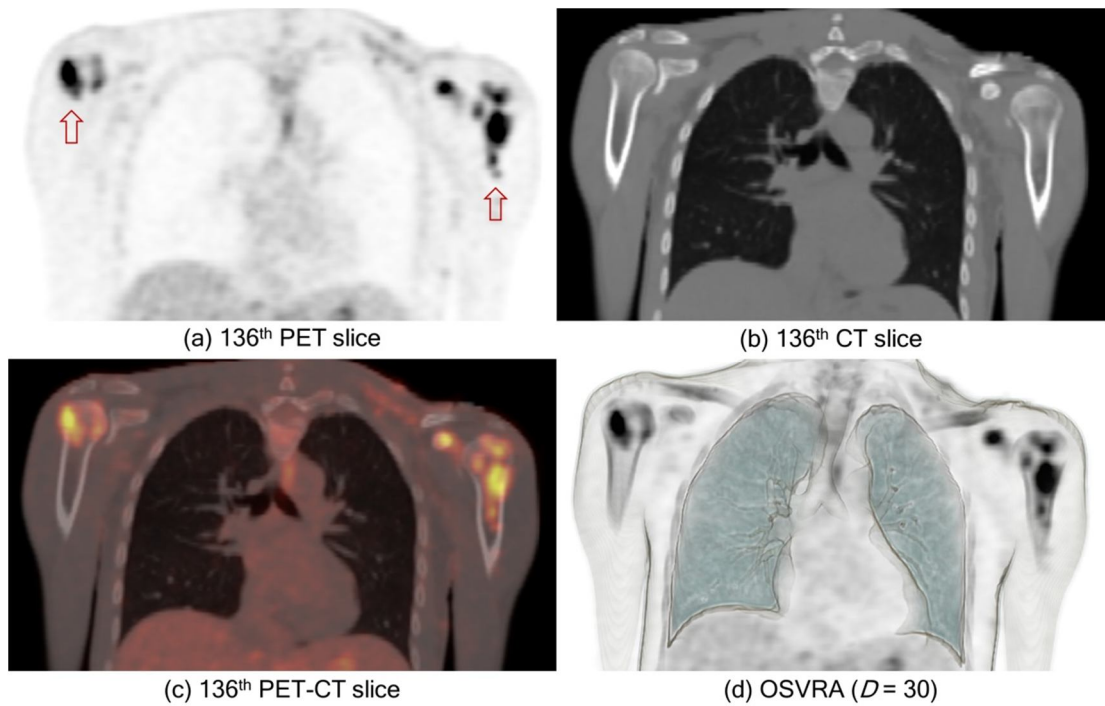


Figure 4.9: A patient study with the bone marrow involvement of the proximal humeri (see arrows in (a)). Comparison of OSVRA with typical coronal view planes used in PET-CT imaging interpretation in routine clinical practice comprising of (a) PET, (b) CT, and (c) fused PET-CT, where PET data are overlaid or ‘fused’ onto CT and the colored regions reflect areas of abnormalities on the PET data.

Figure 4.9 shows the typical coronal view planes used for PET-CT imaging interpretation when compared to OSVRA. The patient had bone marrow involvement of the left proximal humerus (see red arrows in (a)). Typical coronal view planes using the slice-by-slice approach show (a) the PET, (b) the CT, and (c) the fused PET-CT, which is commonly used in routine clinical practice. In (c), a color-scale TF ranging from red to white color was applied to the PET and then was fused onto the CT so that colored regions reflect areas of abnormality on the PET. Since the PET and CT were typically rendered using two individual gray-scale TFs, the information from the PET and CT are problematic to interpret. It is important to note that these 2D visualizations do not provide 3D anatomical contextual cues; clinical experts rely on scrolling through multiple coronal slices and their expertise and experience to mentally reconstruct the 3D information. Our visualization in (d), augments anatomical structures onto the 2D SOI in a more readily assimilated package than the individual coronal planes and the fused plane.

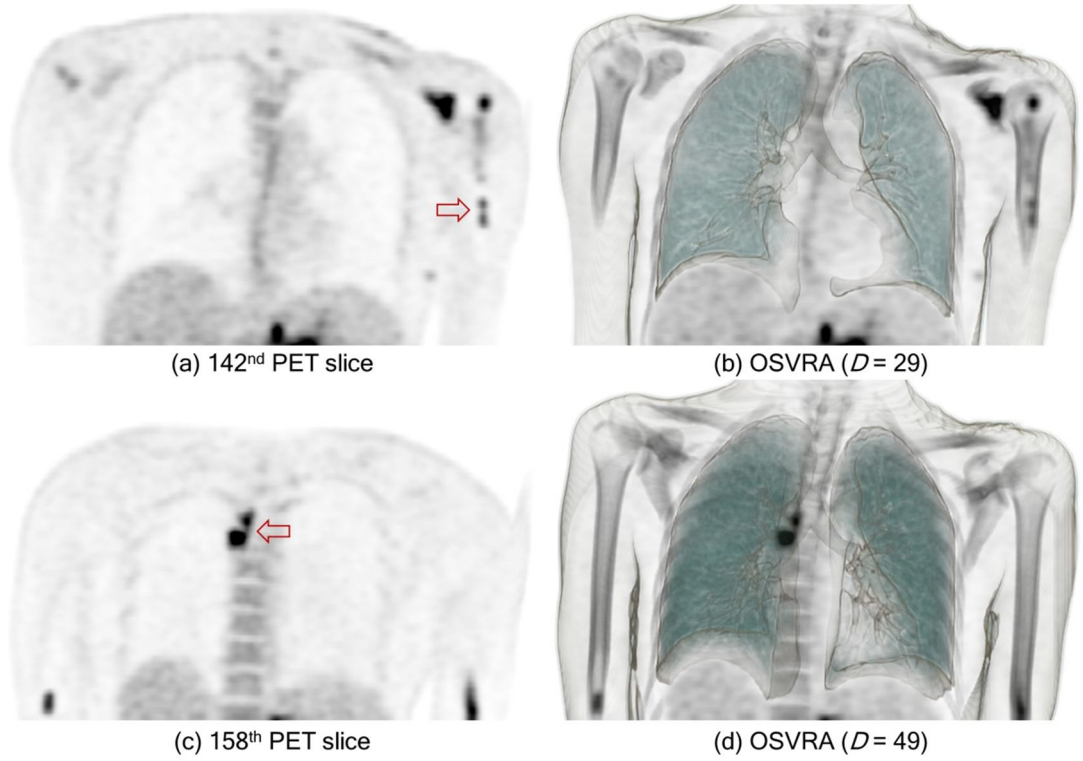


Figure 4.10: Slice-by-slice image volume navigation with OSVRA in comparison to coronal view planes of PET, applied to the same PET-CT patient study as in Figure 4.9.

Figure 4.10 shows OSVRA visualizations applied to different slices of the same PET-CT patient study used in Figure 4.8. The figure shows that the D and opacity weight curve in OSVRA were dynamically calculated during the slice-by-slice image volume navigation. This allowed different structures to be augmented onto different slices, e.g., the proximal humeri in (b), and the lung parenchyma and the bronchial tree in (d). These anatomical cues were not available in the coronal view plane equivalents in (a) and (c).

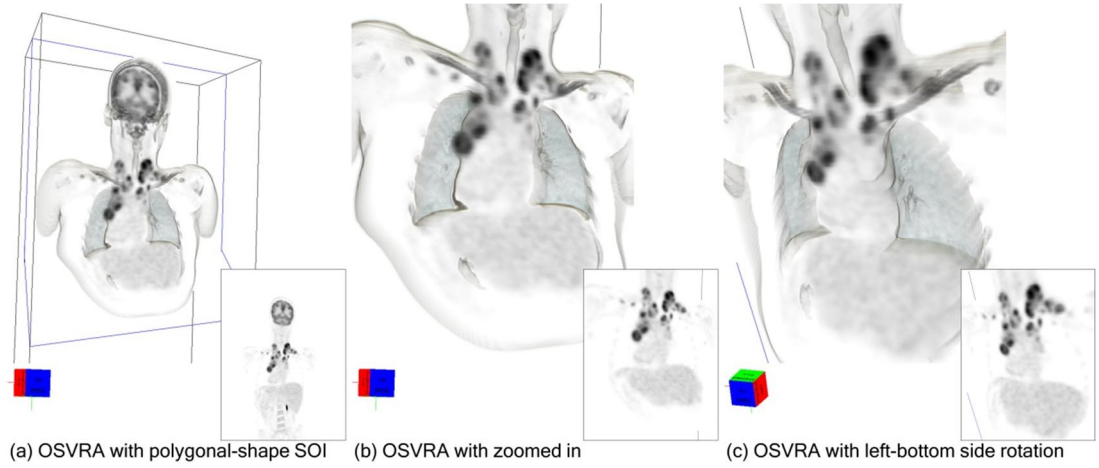


Figure 4.11: A patient with lymphoma at the base of the neck and in the mediastinum. (a) is a visualization with an arbitrary polygonal-shape SOI (indicated by the blue lines); (b) is a zoomed in visualization; and (c) is an oblique visualization rotated to the left-bottom side from (b). The D derived from (a) is applied to the visualizations of (a) and (c).

In Figure 4.11, we show OSVRA visualizations during view-point navigations in a patient with. (a) is the resulting visualization from the application of a polygonal-shape SOI (indicated by the blue lines), which shows that any arbitrary SOI shape could be used to compute D and produce the subsequent augmentation of volumetric context, e.g., lungs and clavicles. In (b), the view-point was zoomed with the same D as in (a) which resulted in relatively consistent contextual information. Rotation of the view-point in (c) shows a new visualization with different contextual information, where the lung fields with the adjacent involved mediastinal nodes are shown.

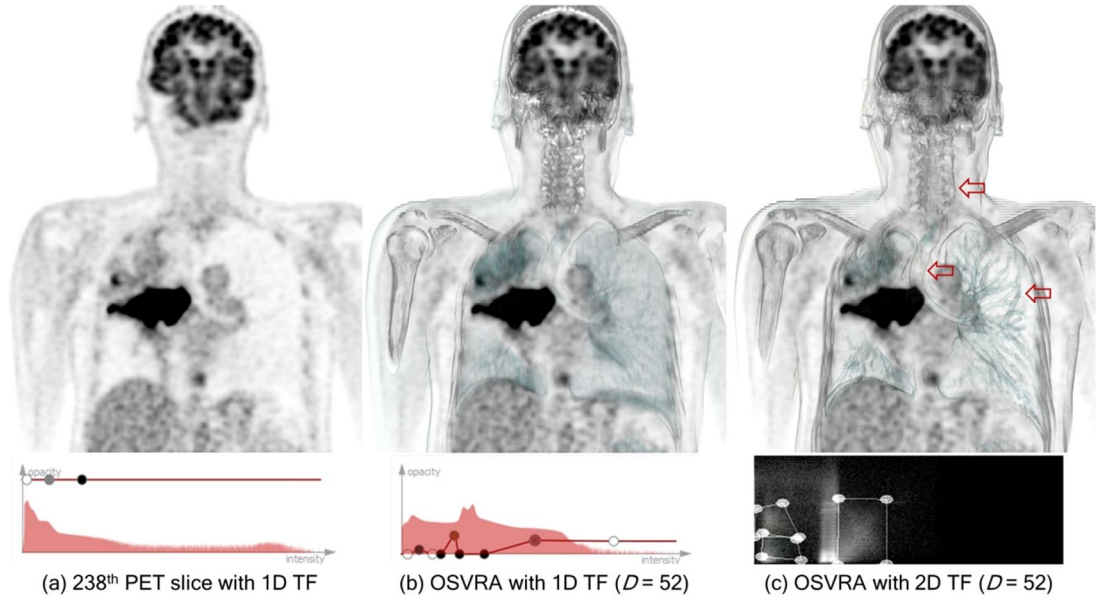


Figure 4.12: A PET-CT study in a patient with a large right lung tumor showing different TFs to OSVRA.

Figure 4.12 shows the application of different TFs to our method in a patient with a large right lung tumor. In (a) the PET SOI that was rendered with a default inverted-grayscale TF; in (b), a DVR of the CT with an intensity-based 1D TF was augmented with the PET SOI; and in (c), the same CT was rendered using an intensity-gradient-based 2D TF [55]. Both the TFs were set to highlight lungs and the bony skeleton. As expected, our method better differentiated the bronchi, trachea, and cervical vertebrae using the 2D TF (indicated by the arrows).

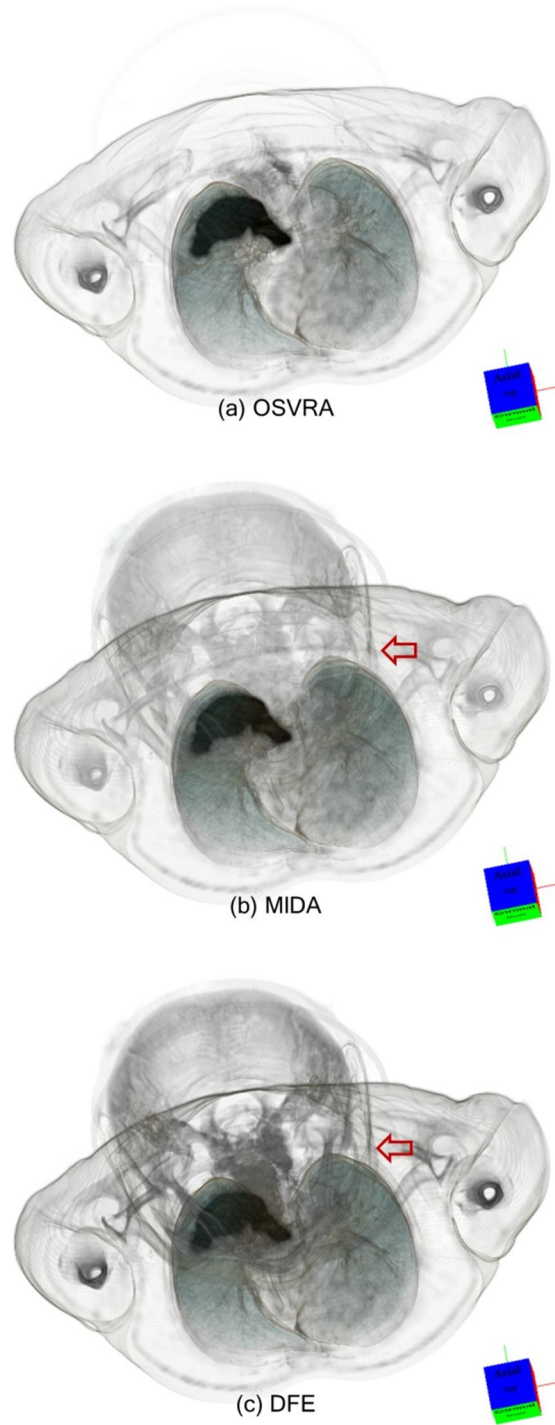


Figure 4.13: A comparison of OSVRA with MIDA and DFE DVR methods. The view-point is tilted slightly at an angle to show the 3D shapes of structures that are in front of the SOI. The same patient as in Figure 4.12 is applied to all the methods.

Figure 4.13 compares OSVRA with the MIDA [61] and DFE [62] methods. For this comparison, the volume rendered images from the two methods were combined with the SOI using the same fusion way as with OSVRA. Further, the volume rendered images were computed only for the structures between the SOI and the same depth was assigned as derived from OSVRA. In this example, we note that the two methods could visualize all the structures in front of the SOI, via manipulation of the opacity values. However, the view of structures which were distant from the SOI, e.g., the skull (see the red arrows), were dominant and this compromised the view of the most relevant structures to the SOI, including the lungs and vertebral column. Our method emphasized only the relevant structures and thus preserved the contextual cues between the SOI and its surrounding structures. Such visual improvements from OSVRA were more evident when the default full DVR renderings (without depth computation) of the MIDA and DFE were applied.

4.5.2 Computational Performance of OSVRA

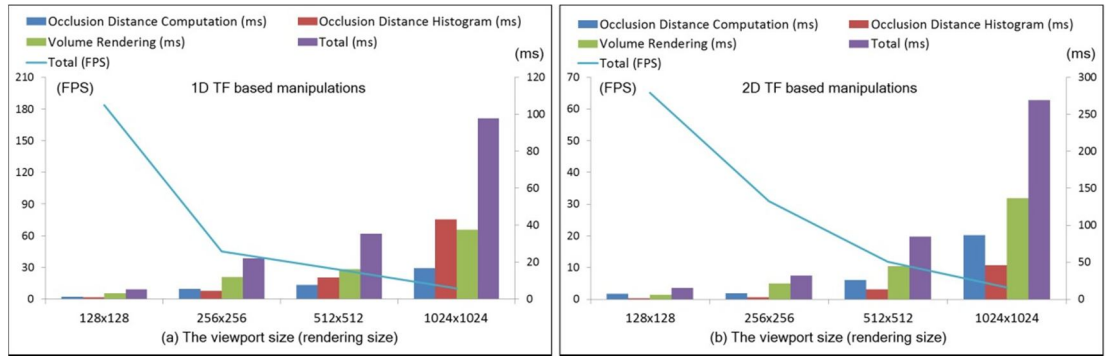


Figure 4.14: Processing times (ms) and frame rates (FPS) for OSVRA during typical volume manipulations in various viewport sizes.

Figure 4.14 is a plot of the computational performance of OSVRA. For each process, computation time was measured in milliseconds (ms); and for interactive visualization, the frame rate was measured in frames per second (FPS). All measures were applied during

typical user volume manipulations that involved rotation, panning, and TF manipulations. Four different rendering viewport sizes were used for the evaluation, ranging from 128×128 to 1024×1024 . Even in the higher resolution (1024×1024) rendering, OSVRA achieved an interactive rate > 10 FPS under 1D TF. As expected, due to greater computation demand with 2D TF manipulations, FPS was reduced from 28.11 to 11.84 in 512×512 rendering but still within an interactive rate.

4.5.3 A User Study using Clinical PET-CT Studies with Lung Cancer

We conducted a user study to investigate the clinical utility of OSVRA applied to clinical PET-CT lung cancer patient studies with a senior medical imaging specialist who has read over 63,000 PET-CT studies. We followed an evaluation procedure based on multi-dimensional in-depth long term case studies [91-93] in which a senior physician's experience and expertise formed the basis for the evaluation of clinical utility.

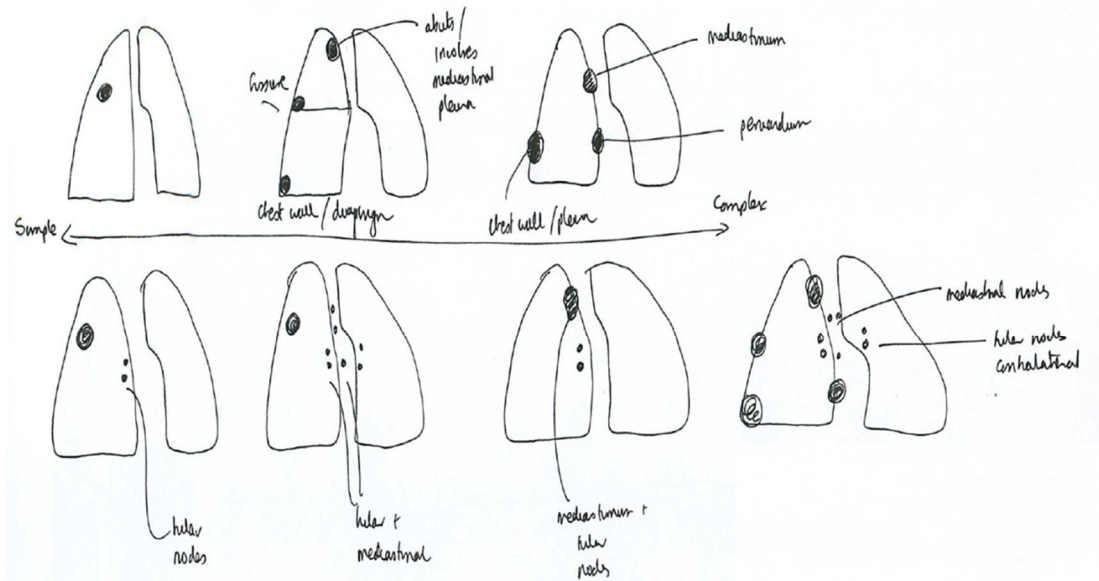
For the user study, we developed a viewing software with three view panes: (i) OSVRA visualization of each patient; (ii) corresponding diagnostic report; and (iii) semi-quantitative questions and general feedback. For the visualization, three depth levels, respectively of the first, second and last peaks from the occlusion distance histogram, were used to render the PET-CT patient study in the coronal and the sagittal views. Forty six patient studies were examined. The software allowed for slice-by-slice navigation of the PET-CT renderings and also adjustment to the window level of the PET data (via the TF). The imaging specialist was asked to interpret the patient study with OSVRA visualizations and to provide feedback on three aspects: (i) the most appropriate depth level (peak from the occlusion distance histogram) for assimilating the PET-CT data; (ii) the benefits provided by OSVRA which are not available with conventional 2D vendor software for PET-CT data; and (iii) general comments about the visualization.

(i) *Depth Level*: In 42 (91%) studies, the first peak was preferred as most appropriate visualization of PET-CT data, reflecting that the minimum DVR depiction (like silhouette) was the preferred visualizations for PET-CT image interpretation as it did not greatly impair the view of the SOI. The second and third peaks meanwhile produced renderings that occluded important contextual details and were the preferred peaks in only 4 (9%) studies. In these studies, the abnormal regions of interest did not have anatomical structures in front of them and therefore did not require occlusion distance analysis. As expected, for these cases, the structures visible from the peaks were not relevant to the ROIs and therefore preferences were given to peaks that visualize additional structures.

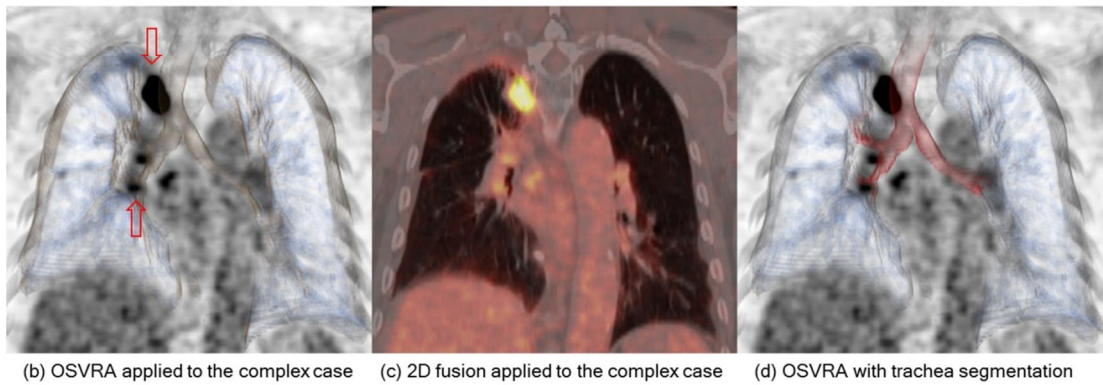
(ii) *Benefits*: In the 42 cases, the key clinical feedback was that the contextual information derived from the CT (visualized in DVR) was useful in accurately localizing the PET abnormalities (visualized in SOI), in particular, where there was regional nodal disease and where the tumor was more central. Central tumors make a surgical approach more problematic as a pneumonectomy may need to be considered to entirely remove the tumor and a pneumonectomy has significant morbidity and mortality. The involvement of regional, in particular, mediastinal nodes, affects surgical options and the radiation planning treatment fields. The imaging specialist provided a hand-drawn schematic (see Figure 4.15(a)) to explain the varying degrees of the complexity in the expression of NSCLC and the importance of the localization of the PET abnormalities in determining the disease stage. Figure 4.15 (b) and (d) show that the OSVRA visualization better outlines the primary tumor and its relationship to the mediastinum and trachea and the lymph node involvement relative to the hilum and the carina when compared to the 2D fusion equivalent.

(iii) *General Comments*: The imaging specialist suggested that OSVRA visualization could supplement the current clinical practice as a rapid overview visualization where the OSVRA could be used as a *fly* through the PET-CT data to quickly identify ROIs of the imaging

study for further detailed interpretation using conventional 2D view planes. Further, the imaging specialist suggested using OSVRA visualization in the context of the multidisciplinary team (MDT) meetings. In MDTs, all the various clinicians (imaging specialists, thoracic surgeons, pulmonologists, medical oncologists, radiation oncologists, nurse specialists, palliative care clinicians, pathologists) involved in a patient's care contribute to the discussion about the best management for the patient [94, 95]. MDTs are considered best clinical practice for patient management. He suggested that the OSVRA would provide a much simpler and rapid display of the relevant data for the non-imaging specialists in the MDT and this would enhance communication and understanding of the imaging findings. Although the trachea is augmented using OSVRA, due to the limitation of the TF it cannot be distinctively identified and our imaging specialist recommended the inclusion of a segmentation label of the trachea and the proximal bronchial tree (shown in Figure 15(d)) given the important impact of central sites of disease to management decisions



(a) A schematic of the varying degrees of complexity in localizing lung cancer for PET-CT imaging



(b) OSVRA applied to the complex case

(c) 2D fusion applied to the complex case

(d) OSVRA with trachea segmentation

Figure 4.15: The issues in accurately staging NSCLC in the thorax from a PET-CT study. In (a) there is a hand-drawn schematic from the imaging specialist outlining the critical elements in staging NSCLC in the thorax. In (b) OSVRA is applied to a complex case with disease in right hilar and subcarinal lymph nodes where the primary tumor is located in the right upper lobe abutting the trachea; (c) is the fused view plane equivalent; and (d) is the inclusion of the segmentation of the trachea outlined in red and the depiction of the tumor in relation to the trachea and the involved lymph nodes in the mediastinum.

4.6 Discussion

Our method offers a multi-dimensional adjunct to conventional slice-based volume rendering methods. Slice-based volume rendering methods require manual volume clipping with each

SOI or view-point change. A key feature of our method is the automated depth computation to produce visualizations that enhance manual volume clipping. Our method, which resulted in contextual information from the DVR (CT) and the retention of the view of the SOI (PET), was consistently better than conventional slice-based volume rendering. We suggest that our method can be applied to a clinical imaging workflow in lung cancer PET-CT patient studies. Although our method was applied only to PET-CT lung cancer patient studies, it does not require any modality-specific or disease-specific parameter settings and so we suggest it can be applied to any dual-modality data that can be visualized in slice-based volume rendering, for example, PET-MR and SPECT-CT. Further, it is feasible for single-modality data such as angiography image volumes (in this case, DVR and SOI are from the same volume).

The value of the depth D parameter in our method was derived by analyzing our proposed occlusion distance histogram. The histogram grouped voxels, which exhibited similar values (intensity and opacity accumulation), together into structures for structure-level analysis. Intensity is the most basic visual yet robust attribute of a voxel and has been widely used in image processing applications, including CT data [28, 96, 97]. However, our method is not limited to any particular voxel attribute and can be adapted to use modality-specific attributes, for example, texture attribute in brain MR imaging [57]. Image segmentation approaches can also be used to construct labels for the structures in defining the TF in our method. An occlusion distance histogram for each segmented structure labels can be generated and used to assign individual depth parameters. We incorporated a segmented structural label to outline the trachea. The trachea was semi-automatically segmented using an active contour approach [98] that uses spatial neighboring information of the voxels in addition to its intensity attribute. The segmentation label was able to differentiate the trachea from the lung tissue, which was not possible with a TF alone in 1D or 2D variants and it can aid localization of the tumor ROI. Such segmentation labels can be particularly useful when applied to MR data where there is inherent intensity inhomogeneity, i.e., the intensity of the

same tissue varies with the location of the tissue within a volume [99], which often prohibits TF from depicting adequate labels.

In all of our visualizations, we avoided potential bias from TF manipulations when comparing our method to slice-based volume rendering by using a set of default TFs for both PET and CT image volumes. For a similar reason, we set the fusion ratio between the two volumes to equal weights. The value of the depth D parameter was derived using the first peak from occlusion distance histogram and was used for all the visualizations. Subtle variations (± 10 slices) from the peak did not greatly affect the resulting visualization. Nevertheless, this parameter can be manually adjusted for user-specific optimizations. The use of the dynamic weight curve in OSVRA, estimated from the automatic computation of the depth D , resulted in a gradual decline in the occlusion of the DVR as its distance from the SOI increased. A static curve function without the depth D could be applied to the manually clipped image volume but this will mandate the adjustment of the TF whenever the clipping depth changed and would add further complications to the clipping process.

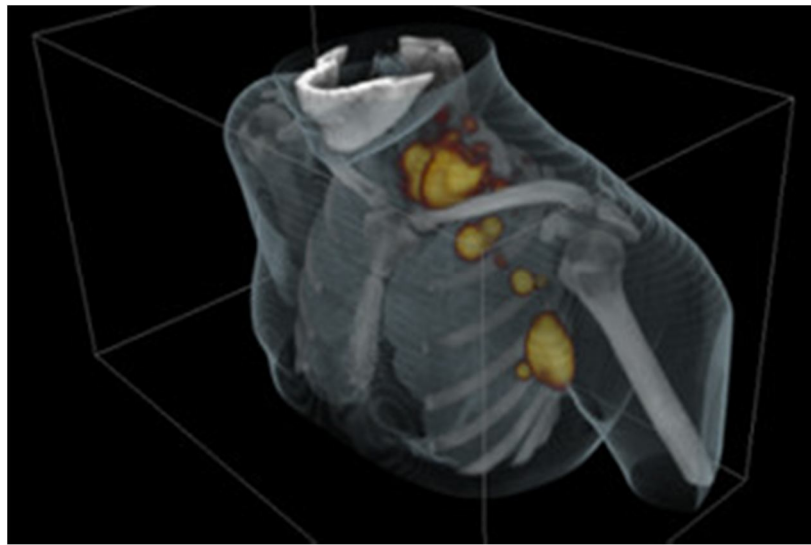
In all the renderings, we employed a TF that was defined to best depict the thorax – soft tissues, the lung fields and the bony skeleton from CT. This setting was optimized for lung cancer studies but for diseases which may involve other anatomical structures, a different TF can be employed and this is not unusual for medical imaging as a disease specific TF is a common requirement.

4.7 Conclusions

We present a new visualization method that automatically augments 2D SOI with the relevant 3D contextual information. The contextual information is calculated based on estimating the occlusion from the voxels (structures) residing in front of the SOI and

rendered by incorporating DVR with an opacity weight curve derived from the occlusion estimation. Our experiments with PET-CT image volumes show that our method was able to augment the 3D structural context onto the PET SOI and avoid the occlusion of the PET SOI, thereby leading to improved visualization when compared to the conventional slice-based volume rendering methods together with volume.

5. An Automated Region of Interest -based Visibility-driven Direct Volume Rendering Technique



PET-CT visualization of a lymphoma patient study

This chapter describes an automatic direct volume rendering (DVR) method that visualizes 3D regions of interest (ROIs), while preserving the surrounding structures, without compromising the visibility of the ROI. In DVR, internal ROIs such as disease often become obstructed by non-relevant structures that are closer to the view-point as DVR renders all structures at once. Under current techniques, the elimination of this occlusion inevitably requires laborious user involvement. The key capabilities of the method are demonstrated in its application to multi-modality positron emission tomography and computed tomography (PET-CT) image volumes. The diseased areas will be the ROIs in this chapter. It resulted in the following publications:

Y. Jung, J. Kim, and D. Feng, "Dual-modal visibility metrics for interactive PET-CT visualization," *IEEE Engineering in Medicine and Biology Society*, pp. 2696-2699, 2012.

Y. Jung, J. Kim, S. Eberl, M. Fulham, and D. Feng, "Visibility-driven PET-CT visualisation with region of interest (ROI) segmentation," *The Visual Computer*, 29(6-8), pp. 805-15, 2013.

5.1 Introduction

Transfer Functions (TFs) are commonly used with DVR to manipulate the image volumes and play a crucial role in generating satisfactory visualizations [45, 55-57, 100, 101]. In practice, the definition of specific TFs is not a trivial task due to the lack of any objective feedback mechanism to quantitatively measure the influence of the TF manipulations on the resulting visualization. As such, users in the current workflow inevitably engage in the unintuitive and iterative tweaking of the TF parameters until they obtain a visualization that is sufficient for their task.

The complexity of defining TFs is compounded when multi-modality image volumes such as PET-CT are considered since they require the combined manipulation of a pair of TFs. In a typical multi-modality visualization [46, 58, 83, 86], TFs are defined independently on the individual image volumes and the resulting image volumes are intermixed (fused). For example, the user may initially define a PET TF and then manipulate its counterpart CT TF to visualize corresponding anatomical regions while minimizing occlusion of the PET. Unfortunately, such individual TF manipulations are complicated and time-consuming. Pre-defined TFs also do not sufficiently cater for inter-patient variation and variations with different pathologies.

In this chapter, we propose a new multi-modality visibility-driven TF for PET-CT visualization where we employ the *visibility* property to measure the level of occlusion caused by CT structures in front of and/or overlapping the PET ROIs. The use of visual cues, such as visibility, has provided useful assistance in DVR processes [102-105]. The Visibility histogram (VH) proposed by Correa and Ma [102] used the level of visibility of all voxels along a view-point as a visual feedback attribute in real-time DVR. They showed that the

VH could help discover occlusion patterns and provide a powerful feedback mechanism to guide and automate the TF manipulation.

We extend the visibility calculations into multi-modality image volumes to provide a mechanism for visual feedback of the occlusion, in this case, of PET by its counterpart CT, and vice versa. Furthermore, we introduce an automatic visibility-driven TF optimization for PET-CT visualization. In PET-CT it is necessary to separate ROIs from non-relevant regions for further analysis. As an example, abnormalities in PET image volumes, including tumors, can occupy the same intensity ranges as normally occurring structures in the body such as the liver, kidneys, bladder, and brain (see Figure 5.1). In such cases, the TF manipulations (in one or more dimensions) are unable to depict all the tumors seen throughout the body even with the aid of the visibility property. This means that the visibility property by itself is incapable of separating ROIs from other non-relevant regions. We thus integrate an automated segmentation algorithm to our visualization framework to allow ROIs from PET to be intuitively selected. The visibility of the ROIs can then be used as an optimization constraint to derive optimal CT TFs. We present the capabilities of our algorithm in the visualization of clinical PET-CT studies with several different anatomy and disease types.

5.2 Related Work

We divide the works related to this chapter into three categories: (i) TF manipulation; (ii) Visibility-driven TF; and (iii) segmentation-based ROI visualization.

5.2.1 Transfer Function Manipulation

The most common TF (1D) has been discussed in Section 2.5.2, which uses voxel intensities to classify the ROIs. A number of multi-dimensional TFs have been proposed to improve the manipulation capabilities. The basic idea is to incorporate varying voxel properties derived

from the image volume into the TF manipulations. In a pioneering study, Kindlmann et al. [45, 100] introduced 2D TFs based on first- or second-order derivatives of voxels within an image volume, thereby enabling users to emphasize the boundaries of adjacent anatomical regions. Kniss et al. [55] suggested a set of widgets to interactively manipulate these TFs. Caban and Rheingans [57] used local statistical texture properties to distinguish ROIs from regions with the same intensity and gradient. Recently, Correa and Ma [56, 101] used spatial voxel properties, i.e., size and occlusion in TFs to manipulate ROIs in complex datasets. However, these studies were inherently designed for single-modality image volumes, and their application to multi-modality image volumes was often restricted to the manipulation of the TF for individual image volumes in isolation.

TF manipulation algorithms for multi-modality image volumes have also been developed and the details have been already discussed in Section 4.2.4. In all prior related studies, TFs were applied to individual image volumes and therefore disregarded how a change in the TF of one image volume could affect the second image volume. Our motivation for this work stemmed from a lack of occlusion feedback from spatially-aligned multiple image volumes in the manipulation of multi-modality TFs. We use the visibility property, which represents how much of each voxel in an image volume is visible to the user, to equip the user with a feedback mechanism for the TF manipulation process.

5.2.2 Visibility-driven Transfer Function

Visibility is a fundamental optical property and its manipulation has been widely used to enhance volume rendering processes by ensuring the observability of ROIs independent of view-point [59, 106, 107] and guiding the identification of the optimal view-point [108-110]. Correa and Ma [102] proposed the construction of VFs that represents the distribution of all the voxels' visibility in the rendered volume. The VF enables users to explore the volume

with real-time feedback about occlusion patterns among spatially related structures during volume rendering manipulations. In addition to introducing the VH, Correa and Ma [102] suggested automatic TF manipulations: view-independent TF definition and TF optimization based on user-defined initial TFs. The former was capable of guiding TF definition to guarantee the visibility of ROIs independent of the view-point by providing a summary of the visibility distributions from all possible view-points. The latter enabled the automated specification of optimal TF parameters (opacities) to maximize the visibility of each ROI. Ruiz et al. [103] proposed another automatic TF optimization scheme, where the visibilities of ROIs (targets) were assigned either by the user or based on the level of importance, e.g., the occurrence of each intensity bin. User-defined initial TFs were automatically optimized towards matching resulting visibility distributions with the ROI targets. Cai et al. [111] improved the matching performance between two visibility distributions by using the Jensen-Shannon distance instead of the Kullback-Leibler distance that was used in Ruiz et al [103]; this improved TF optimization through a faster convergence of the visibility distribution matching. Wang et al. [104] used the visibility property to introduce the concept of *feature visibility* in which the visibility was computed for every *feature* in an image volume. The features were user-selected visual attributes in the intensity-gradient-based 2D TF space and were used to manipulate the volume rendering. These algorithms above, however, were inherently optimized for single-modality image volumes. Their applications to multi-modality image volumes resulted in a lack of the visibility feedback among multi-modality image volumes, which is our motivation of this work.

5.2.3 Segmentation-based Region of Interest Visualization

This content has been already discussed and readers can refer to Section 4.2.1. In this chapter, we have used automated segmentation to select the ROIs for use in visibility-driven TF manipulation. Segmentation enables separation of different structures in PET, which can then be used for ROI-based analysis and visualization. This is different to approaches that

only use the VH, which are unable to provide a visibility property only for the ROIs, since they cannot separate the visibility of ROIs from non-relevant regions [8].

5.3 Methods

5.3.1 Overview

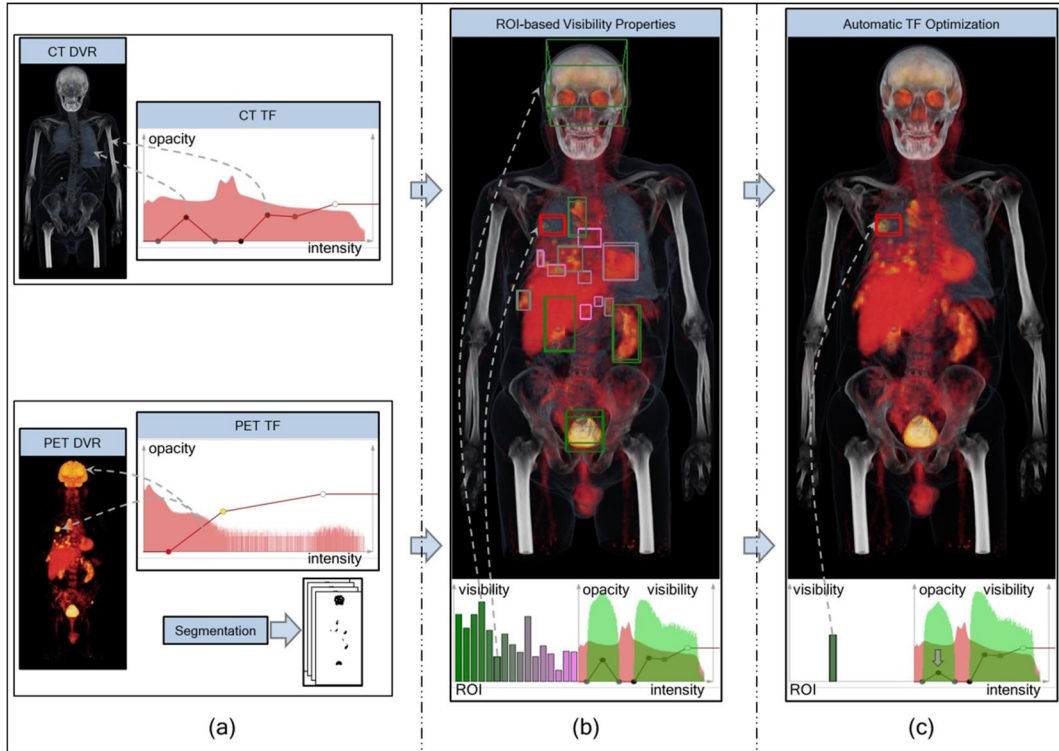


Figure 5.1: An overview of our ROI-based visibility-driven visualization framework applied to multi-modality PET-CT image volumes.

Our PET-CT visualization framework consists of three major components as shown in Figure 5.1. First, individual PET and CT image volumes are rendered with their own TFs (Figure 5.1(a)). The CT TF control line is assigned to two opacity peaks corresponding to the lungs and skin (first peak) and the bones (second peak), as indicated by the arrows. Similarly, a control line is defined for PET to allow the selection of high functional activities, which includes the tumor but also other non-relevant structures. Prior to rendering, the PET image

volume is automatically segmented into ROIs to separate high uptake structures. Note that this segmentation takes only a few seconds and does not have to be performed in a pre-process.

The two image volumes are intermixed into a single visualization (Figure 5.1(b)). The VH is then computed for the PET and CT image volumes by taking into account the overlapping voxels from the two image volumes as well as their opacity mappings. ROI-based VHs (green-pink bars) are calculated for each ROI; for CT, the VH (green bars) is calculated using its intensity range and drawn on top of its intensity histogram. As the user redefines the opacity mapping from one of the TFs, the VHs are recalculated, thereby showing the user the effects of the changes on the PET and CT VHs.

Finally, our TF of the CT is automatically optimized based on the user ROI selection to minimize the occlusion of the selected ROI (Figure 5.1(c)). In this example, the selected tumor ROI (red box) in the lung is made more apparent compared to the rendering in Figure 5.1(b), with increased visibility of the PET ROI (compared to Figure 5.1(b)) and reduction in the CT visibilities belonging to the lung structures (first peak).

5.3.2 Regions of Interest Segmentation

We have adopted an automated PET thresholding segmentation algorithm [112] to construct our ROIs based on the PET response criterion (PERCIST) [113]. PERCIST is an approach to derive metabolic changes in malignant lesions. It uses a reference region placed on the right lobe of the liver (or the descending aorta when there is an abnormality in the liver); the metabolism of this region is used to calculate a threshold value for PET segmentation. However, as a thresholding approach, it includes, in addition to the tumors, other non-

relevant regions that are above the threshold (typically consisting of the brain, bladder, and kidneys). In our experiments, we defined groupings of more than 10 voxels as separate ROIs.

5.3.3 Regions of Interest-based Multi-modality Visibility Histogram

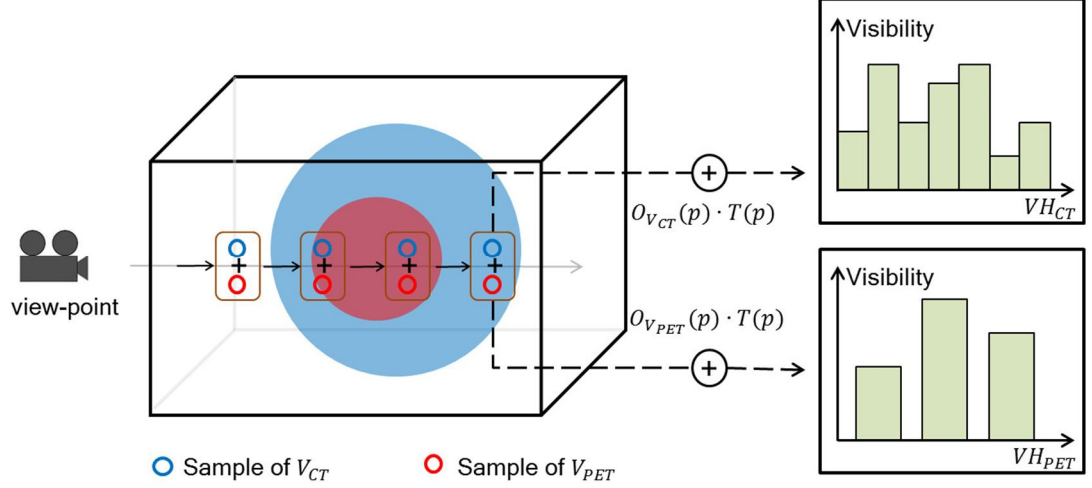


Figure 5.2: Calculation of the ROI-based multi-modality PET-CT VHs.

VHs can be used to guide TF manipulation by showing the user the opacity contribution of particular intensity value to the rendered visualization. In this chapter, we have extended the VH calculation into two overlapping image volumes (as illustrated in Figure 5.2), in which the ray passes through voxel pairs in the PET and CT image volumes, V_{PET} and V_{CT} . The combined visibility for a coordinate position p , $T(p)$, is the accumulation of the opacity contributions of all the voxel pairs starting from a view-point E to p (front-to-back composition) according to:

$$T(p) = e^{-\int_P^E A(t)dt} \quad (5.1)$$

$$A(p) = A(p - \Delta p) + (1.0 - A(p - \Delta p)) * O(p) \quad (5.2)$$

where $A(p)$ is the composition of opacities from the voxel pair, $O(p)$ is the voxel's opacity, and Δp is the size of the sampling step. The visibilities of the voxels, computed as the product of the voxels' opacities, were then added into the corresponding bins of the visibility histogram $VH[x]$ with x as the bin number such that:

$$VH[x] = \sum_{p \in x} O(p) \cdot T(p). \quad (5.3)$$

The VH for a CT image volume VH_{CT} was constructed with N bins representing the entire intensity range; we used a fixed number of bins (256) by uniformly partitioning the intensity range. Each PET ROI occupied a bin in the VH, VH_{PET} . We truncated low count intensity ranges (less than 10 voxels) and normalized our histograms into a logarithmic scale to better accommodate the large dynamic range of the visibility distributions.

5.3.4 Automated Transfer Function Optimization

Our multi-modality visibility-driven TF enabled automated optimization of the CT TF by maximizing the visibility of ROIs from its counterpart PET. We formulated the manipulation of the CT TF as an energy minimization problem. The set of opacity parameters θ of an initial CT TF (preset) was optimized by minimizing an energy function E consisting of: (i) tolerance of PET ROIs visibility (E_T) and (ii) freedom of TF movements for CT (E_F). The tolerance of ROI visibility was used to control how much of a ROI is to be made visible in the resulting renderings. It was calculated by a sum of the squared differences between user-defined visibility V_D and resulting visibility V_R for the individual ROIs:

$$E_T(\theta) = \sum_{b=1}^B (V_{D_b} - V_{R_b})^2 \quad (5.4)$$

where B is the number of ROIs. The value of V_D could be specified by either the user or through automated approaches, e.g., probability-based data importance [103]. The freedom of the opacity parameters is used to control the minimum θ_n^{min} and maximum θ_n^{max} of the n^{th} opacity parameter in the final TF such that:

$$E_F(\theta) = \sum_{n=1}^N |\theta_n^{min} - \theta_n|_+^2 + |\theta_n - \theta_n^{max}|_+^2 \quad (5.5)$$

where N is the total number of the parameters and $[x]_+$ is a clamping operator such that $[x]_+ = x$ if $x > 0$ or 0 otherwise. The freedom of TF movements was necessary to ensure that unimportant structures were not unintentionally made transparent, i.e., they remained somewhat visible to provide context to the ROI. Finally, the optimal CT TF was generated with an iterative manner satisfying:

$$argmin_{\theta} wE_T(\theta) + (1 - w)E_F(\theta) \quad (5.6)$$

where w is the weight for visibility tolerance. The weight is set to 0.9 for higher priority of visibility tolerance in TF optimization as well as to suppress less important structures. We used a downhill simplex optimization method [114][23] to solve the minimization problem. This method was chosen for its effectiveness in non-linear optimization with multiple local minima [115]. The method was less dependent on the initial TFs [116][25] compared to gradient-based approaches [117, 118], which was an important characteristic to ensure convergence.

5.3.5 User Interaction for Regions of Interest Definition

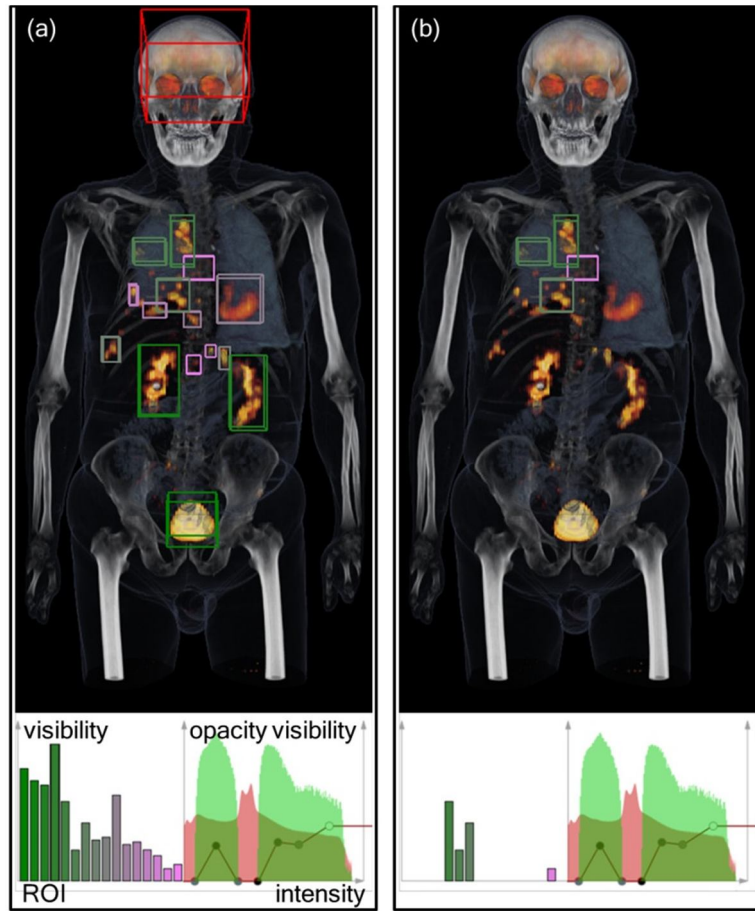


Figure 5.3: An example of ROI selection in multi-modality visibility-driven visualization.

A key requirement for any ROI-based visualization is an intuitive and simple method to select ROIs. In our visualization approach, we used PET segmentation to automatically derive ROIs and then to construct a ROI-based VH in which the visibility of each ROI was represented by a bar. These bars were then sorted according to intensity and distributed in a color range spanning from green to pink (left to right in Figure 5.3). The ROIs in the rendering were represented by a bounding box with the same color code as its corresponding visibility bar. The users could select the ROI by clicking on its corresponding bar as shown in Figure 5.3(a). Non-relevant regions could be selected and then removed. The bars of all

non-relevant regions were removed from the ROI VH shown in Figure 5.3(b). Note that the ROIs in 5.3(b) are not fully visible from this view-point.

5.4 Implementation

We needed to compute multi-modality visibility-driven TF during the interactive volume renderings in order to use the TF as a visual feedback mechanism. In our graphics processing unit (GPU) implementation, we used a vertex shader to calculate the visibility of the voxels from the two image volumes with a single ray casting. Parallel processing, together with a fragment shader was used to calculate the visibility of several volume slices simultaneously in a single-pass.

5.5 Results

5.5.1 Synthetic Image Volumes

The multi-modality VH represents the visibilities of the composited voxels from multiple image volumes. As such, this VH considers *composite dependency*, which measures the occlusion of voxels in an image volume to its counterpart voxels, in addition to the existing opacity and view dependencies. Figure 5.4 demonstrates the application of our proposed multi-modality VH on two synthetic image volumes.

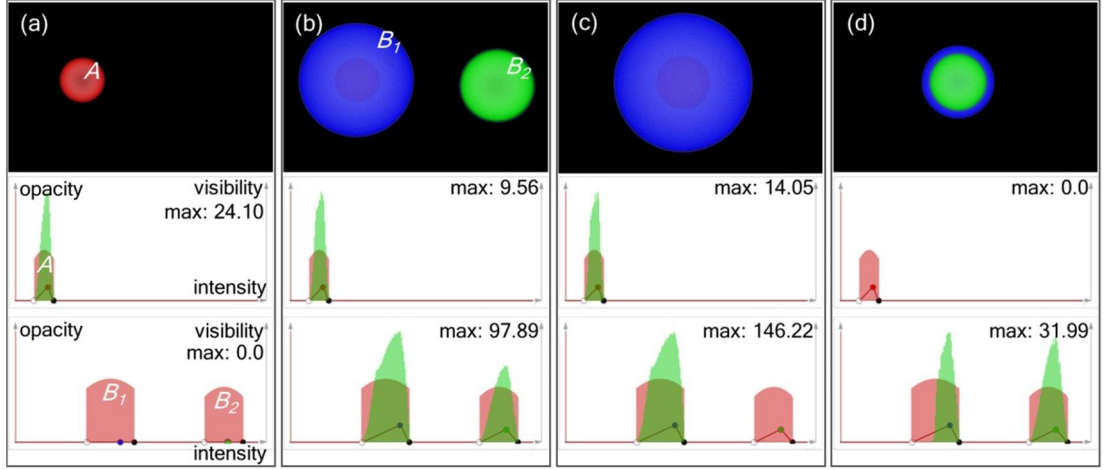


Figure 5.4: Illustration of composite and view dependencies of multi-modality VHs on two aligned image volumes.

In this scene, three colored spheres were rendered with low-to-high intensities spread out in Gaussian distributions from the center to its outer rim. Here, image volume A (red) consisted of a small sphere and image volume B consisted of two larger spheres, B_1 (blue) and B_2 (green), where B_1 had the same center but larger radius compared to A and therefore completely encapsulated the sphere. These spheres were all assigned to the same opacities and were controlled by a pair of 1D TFs. In Figure 5.4(a) only A was visible with the opacities of B_1 and B_2 set to zero. The increase in the opacities of B_1 and B_2 resulted in their visibility increasing while lowering the visibility of A (maximum visibility decreased from 24.10 to 9.56 (60.33%)), as in Figure 5.4(b), affecting both its rendering and its VH. In Figure 5.4(c), the two image volumes were rotated such that the overlapping A and B_1 were now closer to the view-point and completely in front of B_2 . This resulted in zero visibility for B_2 , even though its opacity was unchanged from Figure 5.4(b), while we see a large increase in the visibilities of the overlapping A and B_1 (46.97% increase for A and 49.37% for B_1). The opposite of Figure 5.4(c) was Figure 5.4(d) where B_2 occluded A completely and B_1 partially. Here, the visibilities of the two overlapping A and B_1 were at their lowest, due to them being occluded from B_2 , while B_2 was at its highest visibility due to it being closer and

fully visible in the current view-point. Note the zero visibility in the lower intensity ranges of B_I in Figure 5.4(d), which represented the voxels closer to the occluded section of the sphere.

5.5.2 Whole-body PET-CT Studies

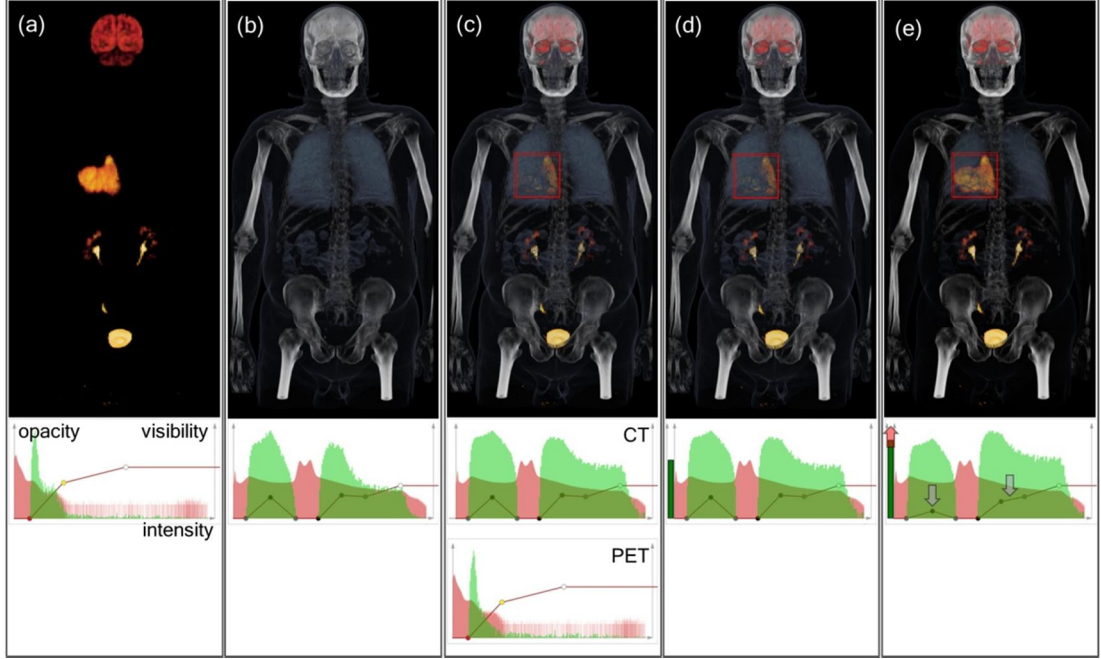


Figure 5.5: PET-CT visualizations using a pair of single-modality visibility-driven TFs ((a) and (b)) compared with multi-modality visibility-driven TF ((c) to (e)). A PET-CT patient study with a large tumor in the right lung was used.

Figure 5.5(a) shows a PET visualization and Figure 5.5(b) shows a CT visualization; the VHs and TFs of each visualization are also shown. The VHs were individually calculated for each image volume. The two image volumes were intermixed into a single scene as shown in Figure 5.5(c); the VHs were recalculated based upon the overlapping voxels. Individual PET and CT image volumes were manipulated by using the TF pair, while observing the effect of the visibility from changes in e.g., PET on the CT counterpart. However, a limitation was the inability of the TF to differentiate the tumor ROI in the PET image volume, in this case the large mass in the right lung, from other non-relevant regions (such as the kidneys, bladder

and brain) that were also visible in the resulting visualization. This made all the structures share the same visibility, thus making the VH irrelevant to the tumor ROI. We used PET segmentation to isolate the ROI and then compute the VH only for the ROI as shown in Figure 5.5(d). The visibility of the PET was then recalculated to represent only the visibility of the ROI. In this visualization, the tumor's visibility was not high due to the occlusion from the lung tissues and the rib cage (bones) in front of and/or overlapping the ROI. We reduced such occlusion by adjusting the CT opacity corresponding to the occluding structures. Figure 5.5(e) shows that this adjustment resulted in reduced opacities for the lung structures and also the bone structures (see grey arrows) while increasing the visibility of the PET ROI (indicated by red arrow).

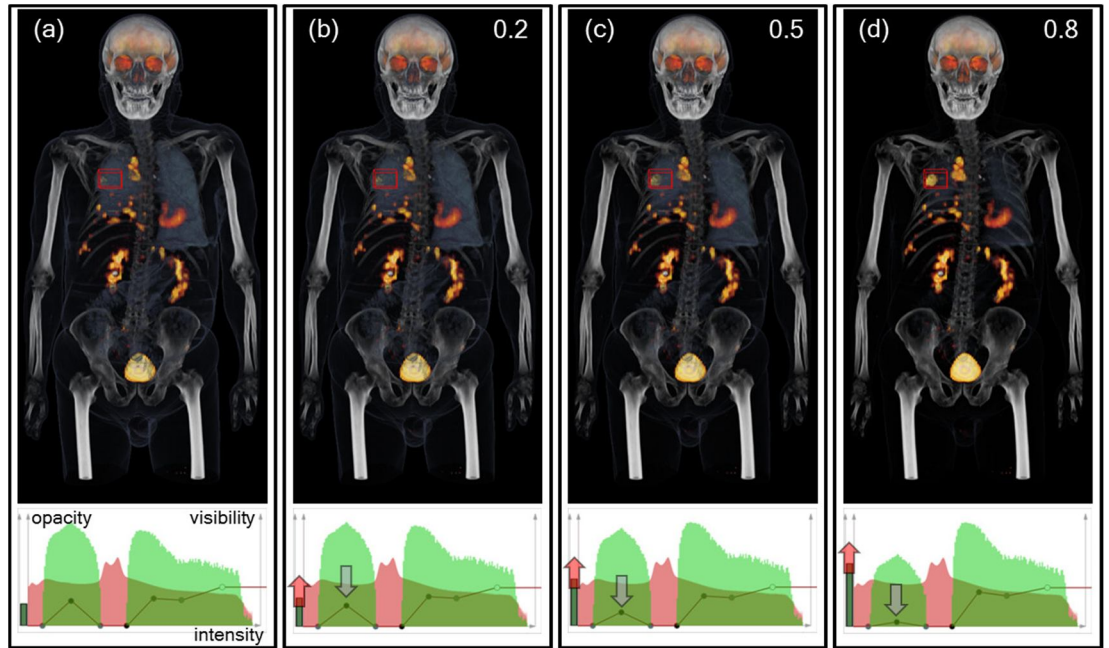


Figure 5.6: Automatic CT TF optimization according to varying constraint of PET ROI's visibility tolerance from low (0.2) to high (0.8).

Our automatic multi-modality TF optimization is shown in Figure 5.6. A tumor in the right lung, which was faintly visible in Figure 5.6 (a), was selected as an ROI (from the ROI-

based VH). Based on this selection, Figures 5.6(b) to (d) represent the visualizations according to varying user-defined constraints for ROI's visibility tolerance. In Figure 5.6(b), a low tolerance of 0.2 was set for the visibility of the ROI, resulting in CT structures dominating the visualization. The reduction of opacity of the lungs in the CT and an increase on the visibility of the PET ROI could be clearly noticed when the tolerance was increased to 0.5 (Figure 5.6(c)), and then to 0.8 (Figure 5.6(d)). In this example, the constraint of the CT TF freedom was set to 0.9 for all variations to give higher degrees of movement.

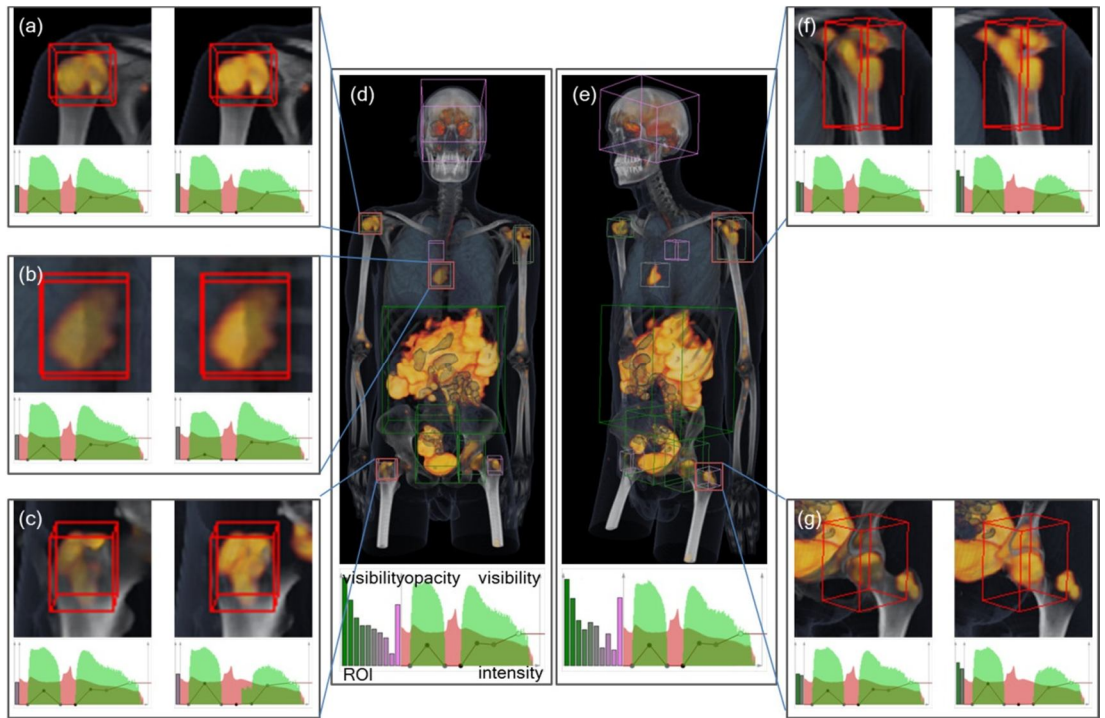


Figure 5.7: Optimized visualization results for a PET-CT study consisting of multiple ROIs across the whole body. Our TF optimization was used to visualize the different ROIs based on user selections in (a) to (c) of a view-point (d), and (f) and (g) of the rotated view (e). The initial visualization (left) of each ROI was to be made more visible (see the corresponding optimized visualization (right)).

Figure 5.7 demonstrates the application of CT TF optimization on multiple PET ROIs. A whole-body PET-CT study of a patient with widespread disease is shown. The two center images (Figure 5.7(d) and (e)) show the same PET-CT study in a coronal view and a rotated view, respectively. The PET TF was set to visualize the segmented ROIs. These ROIs could be selected individually or as a set, and used to automatically optimize the initial CT TF. A powerful feature in the VH is its ability to calculate the visibility according to the user's view-point. Figure 5.7(e) shows the changes in the PET ROI visibility from the rotation with only a small difference in the CT. The constraint of the CT TF freedom was set to the same value as in Figure 5.6.

5.5.3 Computational Performance

Figure 5.8 shows the computational performance, using various volume sizes, for the following interactions: (i) the calculations of VH from random interactive volume manipulations including view-point rotations, panning, and TF changes, measured by frame rate (Frames per Second (FPS)); (ii) interactive calculations of view-independency VH based on averaging 6 rotations as in [102], measured by frame rate (FPS); and (iii) single ROI-based TF optimization, measured by time (seconds). For PET-CT studies with 2 image volumes with dimensions of $256 \times 256 \times 256$ voxels, which is an approximation of a typical study used in this work, we measured 10.14 fps for various random volume manipulations, thus providing interactive volume rendering with real-time feedback of the manipulations. As expected, the interactivity decreased based on the image volume dimensions; we measured 3.446 fps when manipulating 2 image volumes with dimensions of $512 \times 512 \times 512$ voxels. It is interesting to note that regardless of the image volume size, the computation time of TF optimization was relatively similar (from 1.020 to 0.426 seconds). We observed negligible differences when varying numbers of ROIS (1 to 16) was selected. This was because the VH construction in TF optimization was only based on the ROIs of

PET which occupied far less bins when compared to the full PET intensity histogram. The reduction of the bins enabled the computation to be performed in a single rendering pass.

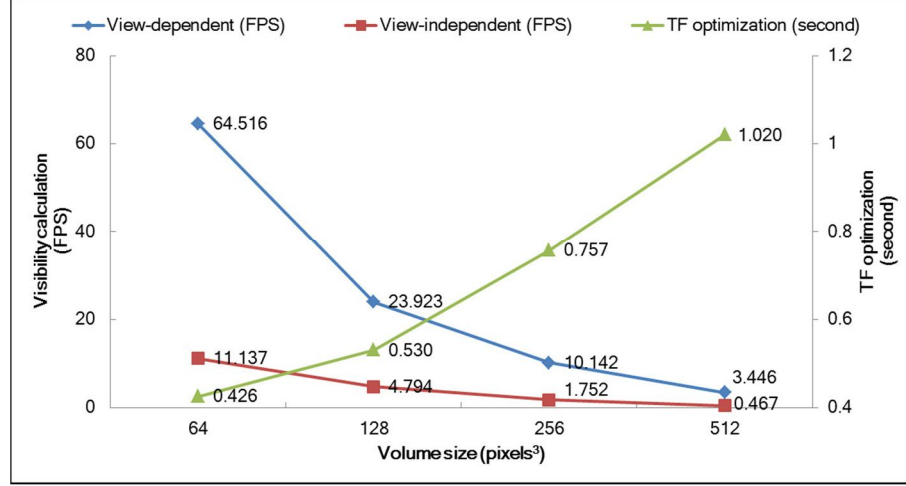


Figure 5.8: The computational performance of ROI-based visibility-driven multi-modality PET-CT visualization. The frame rate (FPS) for visibility calculation (both view-dependent and -independent) and time (seconds) for TF optimization are given in relation to the different size of PET-CT image volumes.

We enabled view-independency by computing the visibility from six different view-points (y-axis rotation) [102]; this extends the ability of VH to guiding TF definition to guarantee the visibility of ROIs independent of the view-point. We achieved 1.752 fps using 2 image volumes with dimensions of $256 \times 256 \times 256$ voxels and 0.467 fps for 2 image volumes with dimensions of $512 \times 512 \times 512$ voxels. These results show that our multi-modality ROI-based visualization could easily compute the view-independent VH after changes to its TF.

5.6 Discussion

This chapter presented a PET-CT visualization method that used the visibility derived from multi-modality ROIs to manipulate the TF. We also presented an optimization of this visibility-driven TF. While we have presented our results designed specifically for PET-CT visualization, we suggest that our approach is applicable to any other co-aligned multi-modality image volumes suitable for ROI-based visualization. This alignment can be derived from a combined modality scanner or through software registration algorithms [119].

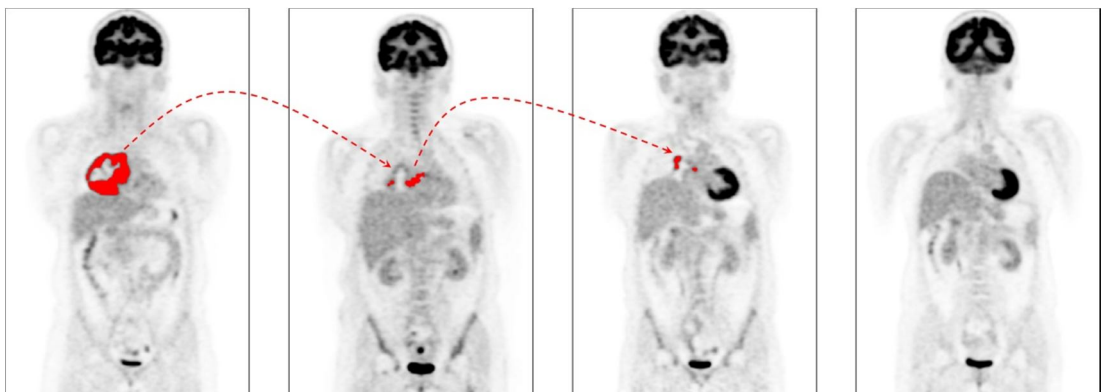
In our results, we used a pair of 1D TFs for PET and CT image volumes. We demonstrated that the use of 1D-based VH, together with ROI segmentation, was able to provide an efficient approach to visualizing PET-CT image volumes. Nevertheless, our visibility calculation is not restricted to 1D TFs and can accommodate multi-dimensional TFs, such as the intensity-gradient-based TF [45].

In our experiments, we adopted the PERCIST algorithm to automatically derive a threshold value to separate malignant tumors from normally occurring structures. PERCIST has the advantage of being a simple yet robust algorithm on inherently noisy and low Signal-to-Noise Ratio (SNR) PET image volumes [113]. Our use of a fully automated approach meant that users were able to interactively select the ROIs to visualize without relying on a complex and manual ROI segmentation process. Our visualization is not restricted to the PERCIST algorithm. It can also support algorithms that are disease / modality specific, e.g., using region growing algorithm for brain PET tumor ROIs [120].

5.7 Conclusions

We proposed a new visualization for multi-modality PET-CT image volumes by integrating visibility-driven TFs together with interactive ROI selection from PERCIST thresholding segmentation. Our visualization experiments with clinical PET-CT studies demonstrated that segmented ROIs from PET could be used to calculate the visibility-driven TF automatically based on occlusion information from the counterpart CT. The TF could then be used for fused PET-CT DVR visualizations.

6. Tracking and Visualizing the Changes in Regions of Interest over Temporal Image Volumes



Temporal tracking of PET abnormalities

This chapter describes a method for automatically tracking and visualizing region of interest (ROI) changes in temporal image volumes under the consistent depiction of the surrounding structures. Visualizing temporal changes in ROIs is essential to assimilate the response to treatment for disease. However, the complexity in generating satisfactory temporal visualizations is much greater when compared to the visualization of a single image volume. The key capabilities of our method are demonstrated through its application to multi-modality positron emission tomography and computed tomography (PET-CT) image volumes. The diseased areas will be the ROIs in this chapter. This chapter led to the following publication:

Y. Jung, J. Kim, L. Bi, M. Fulham, and D. Feng, “A Temporal Visualisation Framework for Multi-modality Medical Images,” in preparing for *IEEE Journal on Biomedical and Health Informatics*, 2015.

6.1 Introduction

The assessment of treatment response can be conducted by viewing a series of temporal scans acquired at different points in time. Multi-modality biomedical imaging devices such as positron emission tomography and computed tomography (PET-CT) have introduced new capabilities for this assessment [27]. The routine approach to evaluate response in imaging is to identify regions of interest (ROIs), in particular sites of abnormality from PET, and then to manually track changes in size and localization across multiple scans over time. This is usually performed by viewing the temporal PET-CT scans side-by-side and manually navigating through each scan. Figure 6.1 is an example of the traditional method for tracking tumors change; it consists of side-by-side 2D cross-sectional view planes for PET, CT, and fused PET-CT image volumes, alongside a 3D direct volume rendering (DVR) of the fused PET-CT.

A key advantage of DVR over 2D visualizations in PET-CT is in its ability to accurately localize ROIs from a PET image volume in relation to the anatomical counterparts from the co-registered CT image volume. These ROI localizations can be visualized via the manual manipulation of Transfer Function (TF) that adjusts opacity and color of the voxels in a single image volume. However, this is not a trivial task as the TF for each individual scan may contain a large number of optical parameters that need to be adjusted from the standard TF settings. The complexity of manual adjustments of the TF parameters is compounded when multi-modality PET-CT image volumes are considered. In a typical PET-CT visualization, the PET TF is initially used to define the ROIs and the counterpart CT TF is then adjusted accordingly to maximally visualize its surrounding anatomical structures while ensuring the visibilities of the ROIs.

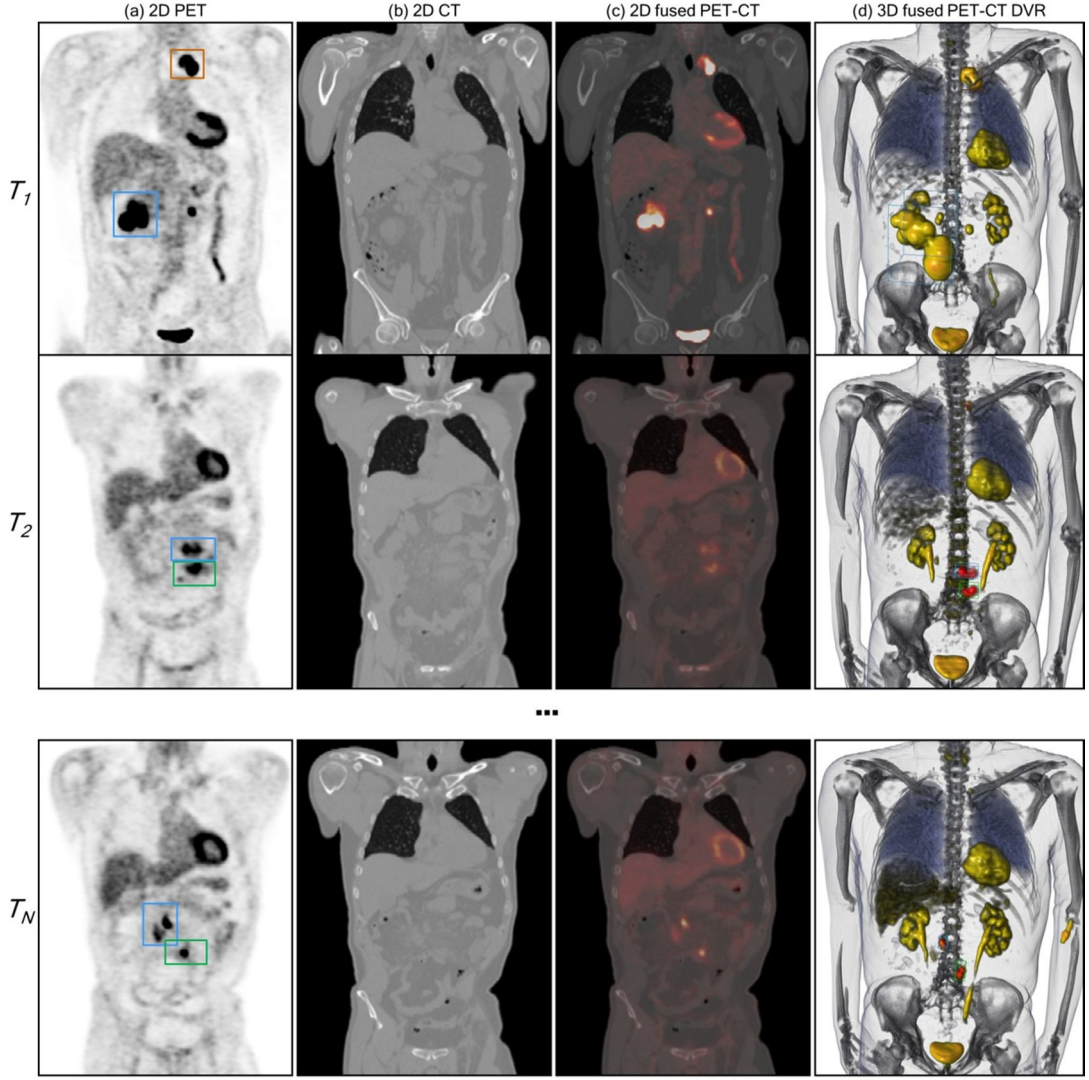


Figure 6.1: Tracking tumor changes using a combined visualization of PET-CT image views. Multiple sites of disease in a patient with lymphoma (enclosed by 2D bounding boxes in (a)) are shown across N temporal scans (T_1 to T_N). The columns show (a) 2D coronal PET; (b) 2D coronal CT; (c) 2D coronal fused PET-CT; and (d) 3D DVR of the fused PET-CT.

Automatic TF optimization has been shown to be valuable in various volume rendering applications, e.g., magnetic resonance (MR) [103] and PET-CT [121] because it alleviates the complexity in manual TF manipulations. To date, however, automatic TF optimization algorithms were only applicable to a single scan (*per-scan* optimization). Thus in application to temporal scans, each scan's TF had to be optimized independently. Such per-scan

optimization becomes problematic as it cannot ensure consistency of the TFs among the scans, which is an important requirement when assimilating the responses to treatment, e.g., tracking changes in tumors in the consistent context of its surrounding anatomical structures across all temporal scans. We term this requirement *temporal consistency*.

In this chapter, we propose a new temporal visualisation framework for PET-CT image volumes in which we introduce a *temporal* optimization algorithm that takes into account the TFs from all the temporal scans simultaneously. Our optimization guarantees temporal consistency and is capable of ensuring the visibility of ROIs across all the temporal scans, while maximally visualizing the surrounding anatomical structures. This is a new visualization approach to temporal PET-CT scans that enables the ability to visualize changes in ROIs (from PET) within a consistent anatomical context (from CT), across multiple scans. Our framework comprises of three key components: (i) a new interactive temporal ROI segmentation method to semi-automatically detect the ROIs from a particular PET scan and to track the corresponding ROIs on the follow-up scans; (ii) a temporal visibility-driven TF optimization algorithm that ensures the visibilities of all the segmented ROIs among the scans; and (iii) a real-time volume rendering and temporal optimization using MRT to compute the large image volumes efficiently. We evaluate our framework using 8 clinical whole-body PET-CT patient studies, each comprising of 4 or more scans.

6.2 Related Work

We divide the works related to this chapter into three categories: (i) temporal volume visualization; (ii) automatic visibility-driven TF optimization; and (iii) temporal segmentation of abnormalities in PET image volumes.

6.2.1 Temporal Volume Visualization

Scientific simulation data such as quantum dot simulation [122] are often temporal in nature since a complex model of many physical phenomena changes over time. Therefore, generating good visualizations for temporal image volumes is one of the key challenges in the visualization community [123]. Jankun-Kelly and Ma [124] proposed the use of a *summarized* TF by merging user-defined TFs among all time points. TF summarization was extended to automatic generation of TFs for all time points by the interpolation of user-defined TFs on key time points [125]. Akiba et al [126] proposed a temporal TF space by combining 1D TFs from all the time points; in the temporal TF space, multiple time points could be manipulated simultaneously. However, in these approaches, the users inevitably needed to manually assimilate all time points, imposing a large mental workload. To simplify the user involvements, several studies proposed a semi-automatic clustering of temporal TF spaces. Maciejewski et al. [127] treated a series of 2D intensity-gradient-based TF spaces for individual time points as a 3D space and clustered the space using kernel density estimation. Wang et al [128] similarly presented an *incremental clustering* that locally clustered the TF space of each time point with the cluster results generated from previous time points. Instead of clustering the TF space, Woodring and Shen [129] suggested a temporal clustering and sequencing of the data to identify objects that had similar changes in data value over time to generate the corresponding TFs. All these visualizations were demonstrated using large-scale simulation data with long time periods; the primary aim was to visualize the changes between two consecutive time points. The requirements for temporal medical image volume visualization differ largely because unlike the methods for simulation data, it is necessary to detect and then track the ROIs across the entire temporal series (all time points). To the best of our knowledge, our study is the first attempt at tracking and visualizing ROIs changes among temporal DVRs of medical image volumes.

6.2.2 Automatic visibility-driven Transfer Function Optimization

This content has been already discussed and readers can refer to Section 5.2.2. Chapter 5 introduced the application of the VH to multi-modality medical image volumes by computing the VH for the two image volumes, and guiding the TF definition of one image volume, while observing the effects of the TF definition on the visibility of its counterpart image volume. Chapter 5 also proposed an automatic multi-modality TF optimization method in which the initial TF of one image volume was automatically optimized as a way of maximizing the visibilities of the ROIs from its counterpart image volume. The optimizations presented in all prior studies were only for a single time point, e.g., a single image volume. The research into its extension to temporal time points to maintain temporal consistency among all time points is one of the motivations for this chapter.

6.2.3 Temporal Segmentation of Abnormalities in PET Image Volumes

In this chapter, our focus is to segment and track PET ROIs across temporal scans. There have been many published works that aim to automate the segmentation of ROIs from PET. However, due to the inherent noise and non-homogenous tracer uptake in PET, abnormal regions often cannot be automatically differentiated from normal structures (e.g., heart and kidney structures can have the same imaging attributes as tumors). Thus interactive segmentation algorithms are often preferred to overcome these limitations of automated algorithms [130]. Few studies have investigated the application of interactive segmentation to detect ROI changes in temporal PET scans. Region-based algorithms have been used for interactive ROI segmentation and tracking changes due to their simplicity and robust performances [131-133]. Opfer et al. [134] presented a ROI tracking algorithm that combined rigid registration, block matching, and region growing methods. Nyirenda et al. [133] used confidence connected region growing (CCRG) with curve fitting algorithm on Rodbard function to track the ROI changes. Although these region-based algorithms were

applied to temporal image volumes, they were not optimized for real-time computational performance and their application to ROI-based temporal volume visualization and TF optimization was therefore restricted. Furthermore, these studies did not investigate the relationship between the segmentation accuracy and its effect on TF optimization, which is an important requirement in medical image visualization.

6.3 Methods

Figure 6.2 illustrates our temporal visualization framework as applied to a patient study consisting of N temporal PET-CT scans (T_1 to T_N). As a pre-process, we calculate the spatial transformation indices among all temporal PET-CT image volumes via automated image registration [135]. These indices show the transformation of points in one image volume to the corresponding points in other temporal image volumes. We provide the user with temporal views for the N PET-CT scans (Figure 6.2(b)) consisting of three 2D orthogonal visualizations of the PET (P), CT (C), and fused PET-CT (F), and a 3D DVR of the fused PET-CT. A pair of TF presets can be applied to all the temporal PET-CT image volumes. We applied a typical CT TF that visualizes major anatomical structures, including the lung, skins, muscles, and bones; and a ramp shape PET TF that is defined to depict regions with high functional activity, such as tumors and lymphomas. Using the 2D PET visualizations, a user selects one of the temporal scans, which is used as an initial time point to track a ROI. The user then draws a 2D bounding box enclosing the ROI on the time point, as shown by the red box surrounding lymphoma in the neck on T_1 scan (Figure 6.2(c)). Our proposed temporal segmentation algorithm automatically detects the corresponding ROIs across all temporal PET scans. Finally, the initial CT TF is then optimized to ensure the visibility of all the segmented ROIs while retaining temporal consistency of anatomical structures via visibility-driven TF optimization. The resulting visualization is shown in Figure 6.2(c); the ROIs (abnormal lesions) are clearly visible in the optimized DVR of the fused PET-CT.

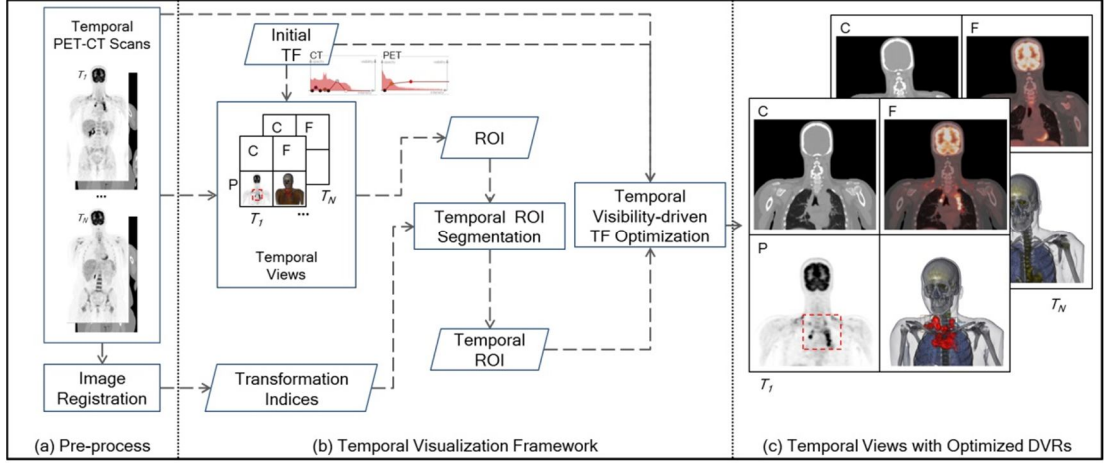


Figure 6.2: An overview of our temporal visualization framework.

6.3.1 Transformation Indices Generation via Temporal Image Volume Registration

For each temporal PET-CT scan $T_i = (T_i^{PET}, T_i^{CT})$ for $i = 1, \dots, N$ where ($T_i^{PET} \in \mathbb{R}^3$ and $T_i^{CT} \in \mathbb{R}^3$), all T_i^{CT} for $i \neq 1$ image volumes were registered to T_1^{CT} . The resulting transformation parameters were then used in the construction of the transformation indices $I_{1 \leftarrow i}$. Affine followed by non-rigid B-spline registration algorithms [135] were used to automatically transform the CT image volume pairs. The CT was hardware co-registered with its counterpart PET, meaning that the CT transformation indices could be directly applied to the PET counterpart. The CT was used in the registration due to its better anatomical definition and higher resolution compared to the PET. We used the indices $I_{1 \leftarrow i}$ to find the reverse transform of any user-selected point p , which could be in either a PET or CT image volume. This provided a set of the points P , one for each point corresponding to p in other temporal image volumes.

6.3.2 Temporal Region of Interest Segmentation

We adopted a PET ROI segmentation algorithm based on cellular automata (CA) theory model [136] and PET response criteria in solid tumors (PERCIST) image thresholding [113] to interactively detect and track the ROIs. Our method was designed to counter the low Signal-to-Noise Ratio (SNR) in PET and enable segmentation of small and low-contrast ROIs. The CA model has been previously used for interactive region-based segmentation in medical images due to its tolerance to noise and image pattern complexities [17, 137, 138]. It is based on a lattice of cells (pixels), which are assigned as either foreground or background pixels. In each iteration, the cells propagate across the whole lattice according to the cell's features e.g., pixel's intensity. PERCIST thresholding is a robust PET intensity-based thresholding method where a single threshold value was derived as the averaged SUV from a volume of interest (VOI) reference placed in either the liver or thoracic aorta. We used as ROIs the group of pixels that had high SUVs within the thresholded results

The user was initially required to select a bounding box β which enclosed a ROI on a scan (T_i). This bounding box was then mapped to all other scans using the transformation indices. The bounding box was enlarged by 10% on all other scans (β^+) to account for possible changes in the ROI over time. We checked whether β^+ contained regions having similar characters as the original ROI. This was done by checking the overlapped regions within β^+ with the PERCIST thresholding results. No overlapping regions indicated an absence of ROIs in a scan. Otherwise, the ROI within β^+ was segmented using the CA model.

The CA model can be defined as a triplet $A = (S, N, \delta)$ where S is a non-empty state set, N is the neighborhood set, and $\delta: S^N \rightarrow S$ is the transition function. The transition function defines the rule for calculating the cell's state at iteration $i + 1$ based on the states of its

neighborhood cells at iteration i . In our study, pixels from PET images were considered as cells and we used Moore's neighborhoods, J , set to 26 pixels:

$$N(p) = \{ q \in Z^J : \|p - q\|_\infty := \max_{j=1,J} |p_j - q_j| = 1 \} \quad (6.1)$$

where pixel q is a neighbour of pixel p where $p \in P$. The cell state S_p is a triplet (l_p, μ_p, f_p) , where the state of p is defined as the label l_p , which is set to 1 for the foreground and 2 for the background; μ_p is the strength, where $0 \leq \mu_p \leq 1$; and f_p is the feature vector, the intensity value of p . We initially set the state of each seed p_{seed} as:

$$l_{p_{seed}} = \begin{cases} 1 & \text{if } p_{seed} \in \text{foreground} \\ 2 & \text{if } p_{seed} \in \text{background} \end{cases}, \mu_{p_{seed}} = 1. \quad (6.2)$$

The segmentation assigns unlabelled pixels based on the transition function [139]. Peak intensity was derived from the mapped enlarged bounding box. Pixels were then assigned as the foreground seeds set if their intensity were $\geq 50\%$ of the peak. Finally, the 26 pixels belonging to the corners, the midpoints of the edges, and the center of the faces of the box, if not already assigned as the foreground, were added to the set of background seeds.

6.3.3 Automatic Visibility-driven Transfer Function Optimization for Temporal PET-CT Image Volume

Our temporal optimization was based on the visibility-driven TF optimization for a single PET-CT scan as given earlier in Section 5.3.4. We expand upon our temporal optimization by taking into account the TFs from all the temporal scans simultaneously, which ensures the visibility of PET ROIs across all temporal scans while preserving temporal consistency of the surrounding CT structures. An initial preset CT TF is optimized towards minimizing an energy function consisting of the visibility tolerance of temporal ROIs and the freedom of

TF movements as in Section 5.3.4. Finally, all temporal scans were visualized with the optimized TF.

6.4 Implementation

We introduce a novel approach of using multiple render targets (MRT) extension in graphics processing units (GPUs) to efficiently calculate the visibilities of ROIs across the temporal image volumes and therefore enable the computation to be performed in real-time volume rendering. MRT improves graphic processing capabilities by permitting the programmable rendering pipeline to simultaneously write and render data to multiple (up to 8) rendering plane buffers, consisting of per-pixel red-green-blue-alpha (RGBA) components. We allocated each component of the buffers to the ROI visibilities, e.g., 4 ROIs in 8 temporal scans to RGBA components in 8 buffers. Figure 6.3 illustrates the visibility calculation for temporal ROIs using MRT. On the GPU side, N temporal image volumes were rendered from the same coordinates (the same view-point) using their view-aligned temporal slices: each sampling point (S_i) had n voxels of the temporal slices (V_N). The visibility of the voxels was computed on a per slice basis.

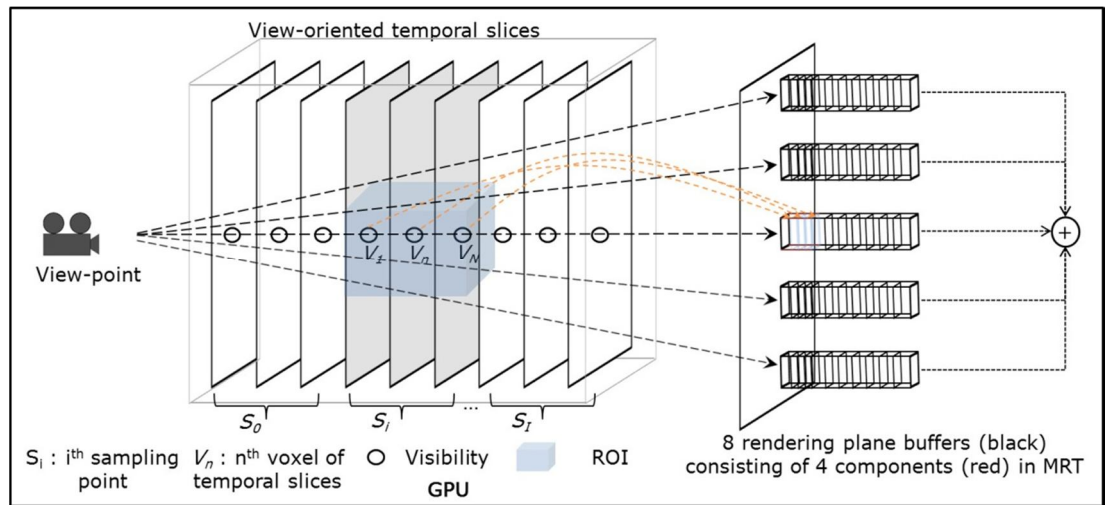


Figure 6.3: GPU-based visibility computation among the temporal ROIs using MRT.

All the visibilities (indicated by the black circles) starting from a view-point to each pixel on the rendering plane buffer were accumulated into the corresponding ROI components. The temporal segmentation results were loaded as a 3D GPU texture to provide the spatial locations of ROIs (the blue cuboid in Figure 6.3). The resulting visibility rendering plane buffers were transferred to CPU memory. We were able to compute the visibilities of 32 ROIs per rendering pass.

6.5 Results

6.5.1 Temporal Visualization Using Clinical PET-CT Studies

Figure 6.4 shows the results from temporal ROI segmentation and subsequent optimization, applied to a high-grade lymphoma patient study comprising of 4 temporal PET-CT scans (T_1 to T_4). Column (a) shows the coronal 2D view of PET scans and column (b) shows the corresponding optimized DVR of the fused PET-CT scans. After the selection of a 2D bounding box encapsulating the lymphoma in the T_1 PET scan (marked by the red box), our segmentation algorithm was able to detect the lymphoma and then track and segment the corresponding ROIs on the following temporal scans (see the red boxes in the T_2 and T_3 PET scans). This segmentation results corresponded to the patient’s clinical diagnostic report in which the lymphoma on the lung became smaller during treatment and was absent on the T_4 scan. In column (b), all the ROIs (enclosed by the red cuboids) were visualized without their view being impaired the surrounding structures. It is also important to note that our method was able to provide the consistent visualization of the neighboring CT anatomy across all the temporal scans (in this example, the lungs and bone). The anatomy was even preserved in the T_4 scan, where the ROI was absent.

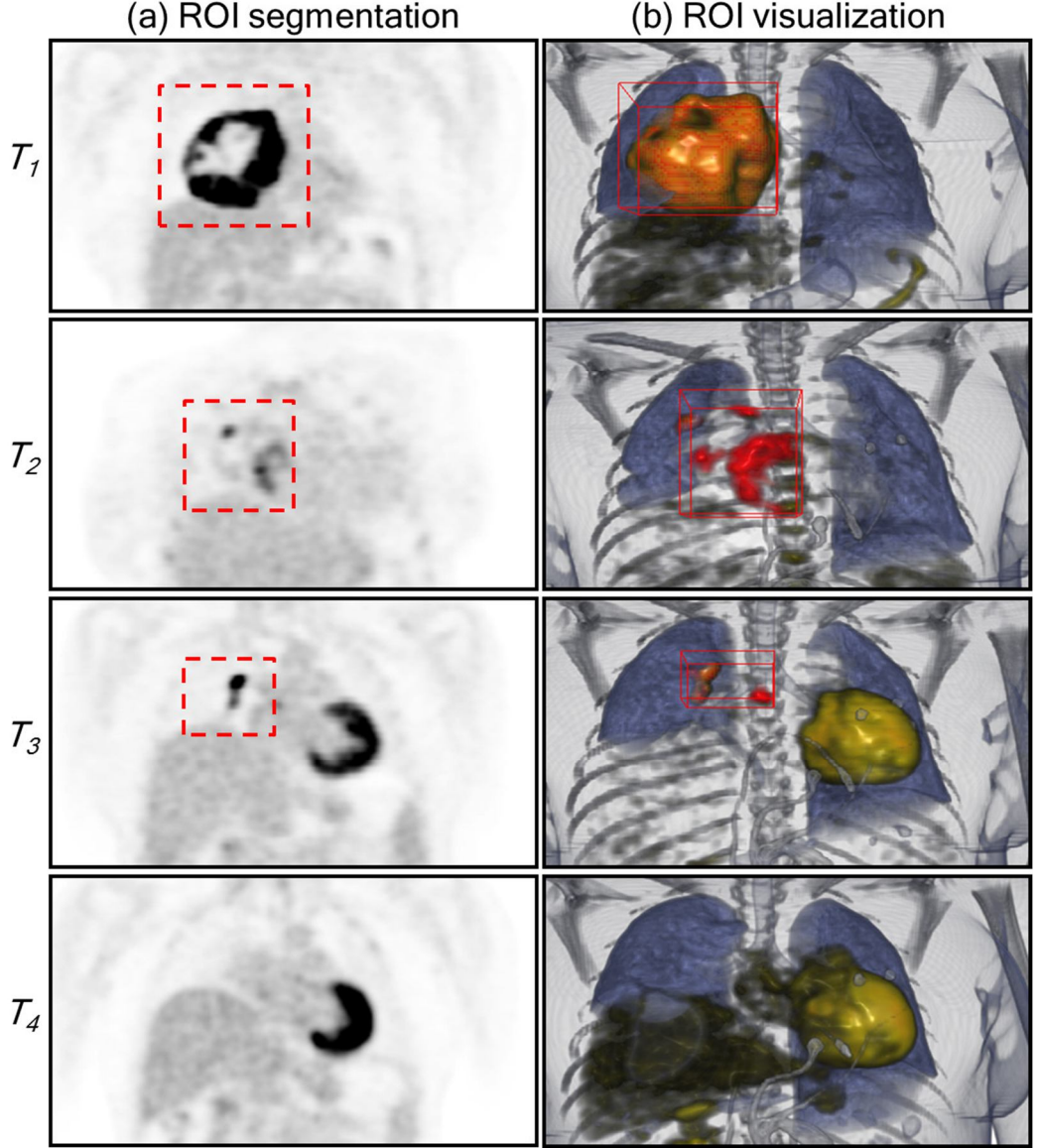


Figure 6.4: Temporal segmentation and visualization on a patient study diagnosed with lymphoma. The patient study consists of 4 temporal PET-CT scans (T_1 to T_4). Column (a) is the temporal segmentation results of the lymphoma ROI (red boxes) and (b) is the optimized visualizations that ensure their visibility (red cuboids). Note the consistent visualization of the ROIs among the scans in respect to its relevant anatomy (the lungs and bone).

An important characteristic of our temporal optimization is the capacity to ensure the visibilities of ROIs across all temporal scans. We numerically evaluated this capability by measuring the visibility error: the sum of differences between $V_D - V_R$ for individual ROIs

divided by the sum of V_D after the optimization, which ranged from 0.0 to 1.0. We observed that only minor errors were obtained among all studies used in Figures, e.g., 0.017 of a lymphoma ROI in Figure 6.4.

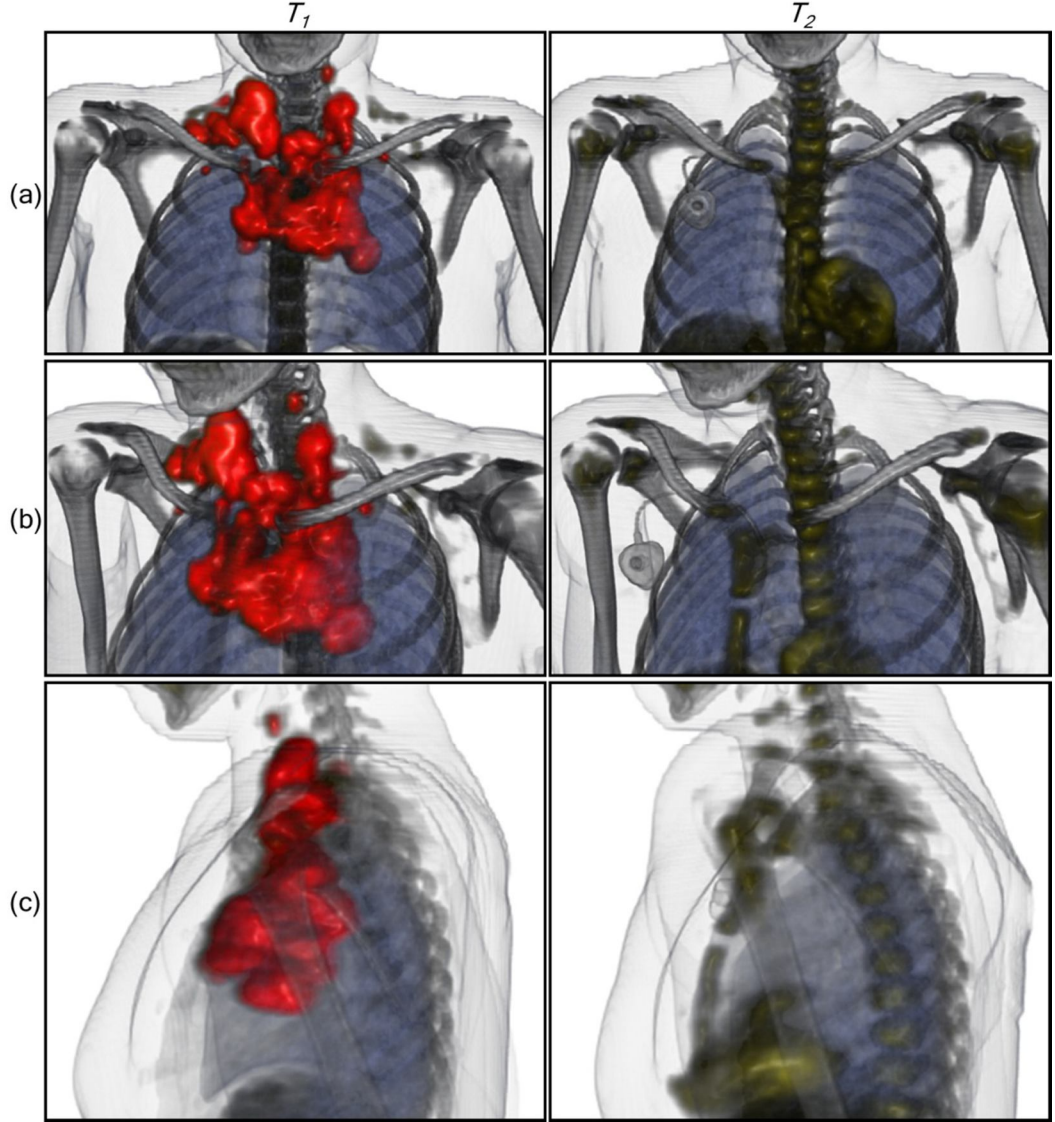


Figure 6.5: Optimized visualization results during view-point rotations for a PET-CT patient study with a lymphoma in the neck. Our TF optimization identifies the anatomical structures occluding the ROI in each view-point and reduces their opacities.

Figure 6.5 shows the optimized visualizations of PET-CT image volumes of a patient with a lymphoma in the neck (T_1) that has responded well to treatment (T_2); the visualizations are shown from different view-points. Our optimization was able to identify anatomical structures that occluded the ROIs from the user-defined view-points and reduce the opacities of the occluding structures to ensure the visibilities of the ROIs. For example, in row (c), the shoulder bone in front of the ROI became semi-transparent, whereas the lungs behind the ROI were still opaque; this provided accurate localization of the ROI.

Figure 6.6 compares the default visualizations from per-scan optimization (row (a)) with the visualizations resulting from our temporal optimization (row (b)). We used a PET-CT patient study consisting of three temporal scans (T_1 to T_3). The patient in this figure had a large lymphoma in the abdomen on the T_1 scan, which was divided into two smaller regions in the following scans; another separate tumor adjacent to the lung was absent in the final T_3 scan. As expected, tracked ROI results from our interactive temporal segmentation algorithm were in accordance with the changes documented in the clinical diagnostic report of the patient study. For instance, the large blue cuboid in the T_1 scan, which corresponds to the lymphoma in the abdomen, was split into two smaller cuboids in the T_2 scan. In the per-scan optimization result in row (a), TFs were individually optimized by taking into account only the ROIs in each scan. All the ROIs were clearly visible in the resulting visualizations. However, as expected, the per-scan optimization resulted in varied visualizations of the same anatomical structures among the temporal scans and failed to provide the temporal consistency for the anatomical structures. For example, in the T_3 scan (row (a)), the tumor adjacent to the lung was absent and the muscles, which highly occluded the tumor, were not fully optimized. In comparison in the T_2 scan, the muscles became transparent to ensure the visibility of the tumor. Our temporal optimization (row (b)) was able to retain the temporal consistency and thus facilitated visual tracking of the ROI changes.

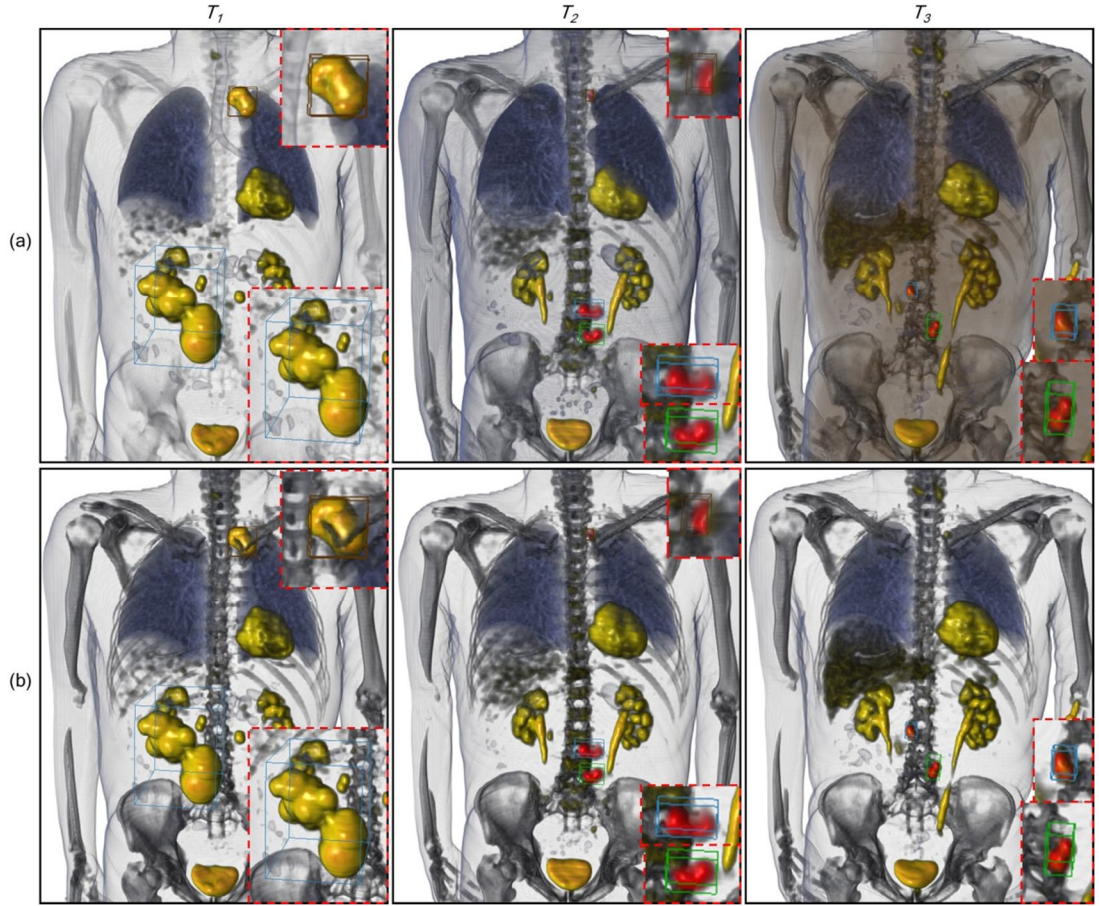


Figure 6.6: A comparison of our temporal optimization to per-scan optimization using a PET-CT patient study with multiple abnormalities (encapsulated in cuboids) in different sites across three time points (T_1 to T_3). Row (a) is the default result of the per-scan optimization and (b) is the result from our temporal optimization. The temporal consistency of the anatomical structures in (b) makes it easy to identify the changes in the ROI when compared to (a), which lacks such consistency.

6.5.2 PET Region of Interest Segmentation Performance

Our dataset consisted of 8 whole-body PET-CT patient studies; 7 patients with 4 temporal scans and 1 patient with 6 temporal scans. We identified 35 temporal ROIs among these studies (including tumors and lymphomas): 1 ROI appearing across 5 scans; 1 ROI across 3 scans; 2 ROIs across 4 scans; 31 ROIs appeared on one scan but not on any others.

We evaluated our CA segmentation algorithm by comparing the segmentation labels with the ground truth (GT) segmentation results. The GT segmentation results were manually constructed using PERCIST thresholding with corrections and refinements by referring to the abnormality findings in the clinical diagnostic reports. We used the dice similarity coefficient (DSC) [140], a well-established method for evaluating segmentation, to measure the overlap between the two segmentation results according to:

$$DSC = \frac{2|A \cap B|}{|A| + |B|} \times 100 \quad (6.3)$$

where A and B represent the set of pixels in the segmentation result and the GT, respectively, and $|\cdot|$ measures the number of pixels in the corresponding set.

We compared our CA algorithm with well-established interactive PET segmentation algorithms; seeded region growing (SRG) [29] and CCRG [131]. We set the size of pixel neighborhood to 26 in all segmentation algorithms. We evaluated and compared different parameters for the standard deviation of the convergence criteria for SRG, ranging from 1 to 3, with increment of 0.1. We found that 1.5 gave the best results and thus set the standard deviation to this value.

Table 6-1: DSC results of PET ROI segmentation using our algorithm (CA) in a comparison with region-based (CCRG and SRG) algorithms.

	CA	CCRG	SRG
Mean	78.29	37.25	55.93
SD	12.84	28.68	27.57
Max	98.21	94.23	98.13
Min	47.01	0.01	0.01

Table 6.1 summarizes the segmentation results of the 55 ROIs from our 34 clinical PET scans. CA had the best accuracy compared to the other algorithms, with the highest mean DSC of 78.29, the lowest standard deviation (SD) of 12.84, the best maximum (Max) of 98.21, and the best minimum (Min) of 47.01.

Figure 6.7 visualizes our CA segmentation results on three varying abnormalities cases. In all the cases (rows), the segmented ROIs from our CA algorithm were the most similar to those of the GT. The higher performance is clearly depicted in Figure 7(c) where there were multiple separated regions belonging to a lymphoma site on the neck. We can observe that both the CCRG and SRG algorithms failed to detect most of the lymphoma; this was attributed to the fact that these algorithms relied on the correct placement of seed points for every separated region. CA did not depend on seed points per region and therefore was able to produce superior segmentation results.

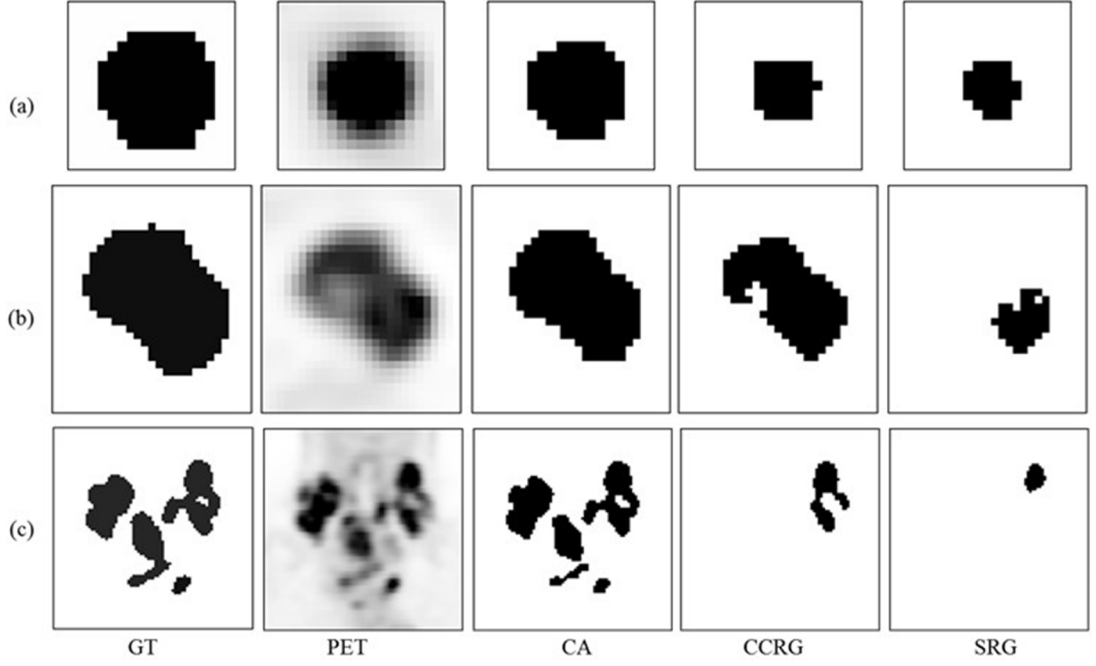


Figure 6.7: Segmentation results on three different types of ROIs: (a) a small tumor ($8\times\text{zoom}$); (b) a middle sized tumor ($6\times\text{zoom}$); and (c) a lymphoma of multiple separated regions ($2\times\text{zoom}$). The GT was constructed by segmenting the PET image volumes manually and was used to compare our algorithm (CA) to other popular region-based algorithms (CCRG and SRG).

Our optimization was highly reliant on the robustness of the CT segmentation algorithm. Thus, we investigated how our visibility-driven TF optimization was able to tolerate errors in ROI segmentation. We simulated segmentation errors by either shrinking or enlarging the normal ROI by morphological operations with radius sizes of 1 to 3 pixels. In total, six variations from the ROI were created with 3 shrunk (S1 to S3) and 3 enlarged (L1 to L3) ROIs. These ROI variants were applied to the TF optimization and the resulting TFs were then compared to the TFs from using the normal ROI. The tolerance was measured by summing the absolute differences between the optimized three TF parameters, ranging from 0.0 to 1.0, where 0.0 means identical results. Figure 6.8 shows the results of the tolerance for the three patient studies having ROIs with different sizes and localizations. The results

indicate that the TF optimization was able to retain good accuracy, even when applied to ROI variants that had large errors, e.g., for S3 in Patient1, where the ROI was reduced to 20% of its normal size, the tolerance in the optimization result was small 0.045 (4.5%). The high tolerance to segmentation errors were attributed to the fact that our optimization relied on the spatial relationships between ROIs and its surrounding structures and therefore had little reliance on the segmentation accuracy of the ROI as long as the relationships were maintained.

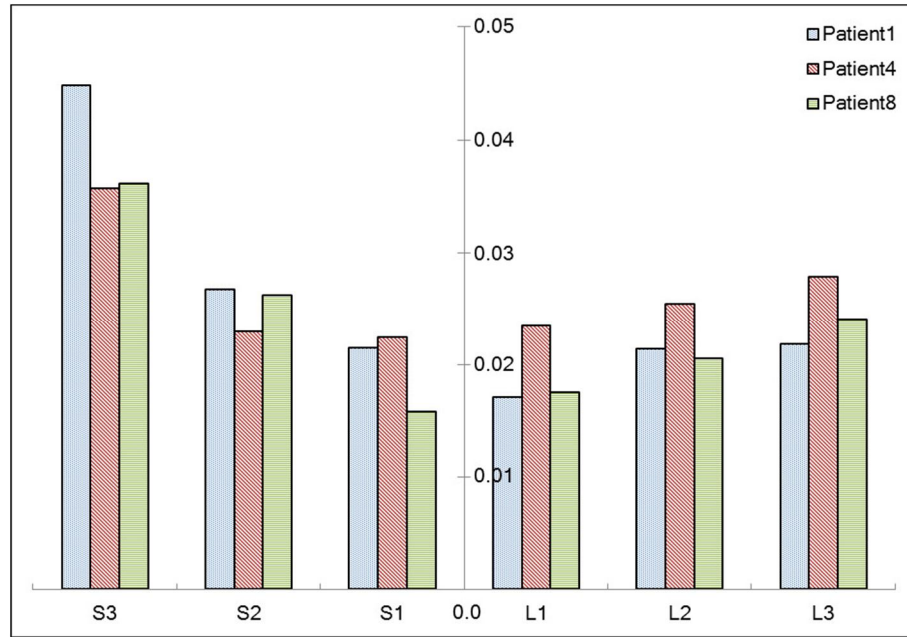


Figure 6.8: The tolerance of our visibility-driven TF optimization to errors in ROI segmentation. The y-axis of the tolerance represents the differences between TF parameters after optimization (ranging from 0.0 to 1.0 where 0.0 means identical results) according to different volume sizes for ROIs in three different patient studies.

6.5.3 Computational Performance

The temporal ROI segmentation was performed in 0.324 seconds for a median box size of 3718 voxels ($11 \times 26 \times 13$). Figure 6.9 shows the computational performance on temporal

visualizations, using the various number of PET-CT scans, for the following interactions: (i) the calculation of the visibility of ROIs from typical volume manipulations, measured in Frames per Second (FPS); and (ii) TF optimization, measured in seconds. We achieved an interactive rate of > 18.53 FPS for the visibility-driven PET-CT visualization. The temporal TF optimization was computed in almost real-time, even with the high-end requirements of 4 temporal PET-CT scans (1.35 seconds). Our method enabled the calculation of the visibility of ROIs over multiple scans simultaneously, allowing us to obtain significant computational improvements when compared to the per-scan optimization counterpart, e.g., 69.03% decrease in the optimization using 4 scans (4.36 versus 1.35 seconds).

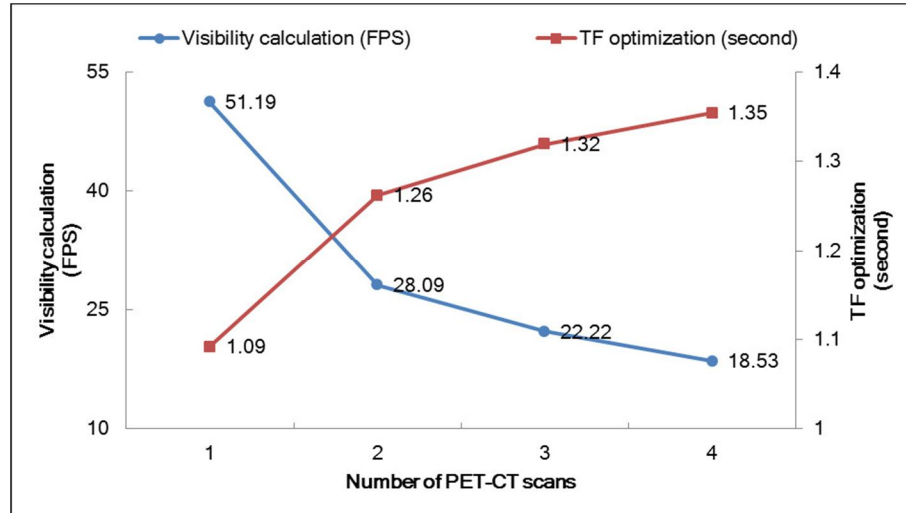


Figure 6.9: The computational performance of our temporal visualization. We calculated the computational time (in seconds) taken for temporal TF optimization (left y-axis), and frame rate (in FPS) taken for visibility calculation (right y-axis) in relation to the number of PET-CT scans (each consisting of two volumes with dimensions of $256 \times 474 \times 134$).

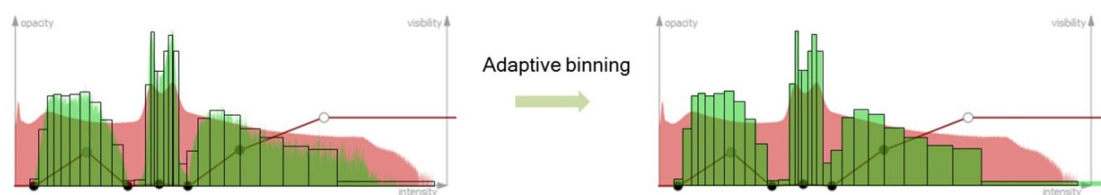
6.6 Conclusions

We proposed a new temporal PET-CT visualization framework for depicting the changes of ROIs (in PET) with the consistent context of the surrounding anatomical structures (from

CT). Our results demonstrated that our framework was interactive, robust in ROI segmentation, and was able to detect temporal changes in ROIs. Our temporal visibility-driven TF optimization, which tolerated errors in ROI segmentation, had the ability to automate temporal visualizations. Our efficient GPU implementation based on MRT allowed real-time visualization and optimization of temporal scans.

7. Visibility Computation

Optimization based on Adaptive Binning



Adaptive construction of visibility histogram

This chapter describes an efficient visibility histogram (VH) computation through the use of adaptive binning. It is an essential process in the other visibility-driven direct volume rendering (DVR) automation approaches proposed in this thesis. This process can be used to compute the visibilities for every voxel in individual image volumes and represent its visibility distribution, such as histogram. Since this is a computationally intensive task, the application of the DVR automation approaches is usually restricted to small image volumes or not in real-time interaction. The key capabilities of our method are demonstrated by using a variety of medical imaging modalities. It resulted in the following publications:

Y. Jung, J. Kim, and D. Feng, "Adaptive histogram with visibility-driven transfer function for PET-CT visualization," *IEEE Pacific Visualization*, Poster, 2013.

Y. Jung, J. Kim, A. Kumar, M. Fulham, and D. Feng, "Efficient visibility-driven visualization of medical images via adaptive binning of visibility histogram," *Computerized Medical Imaging and Graphics*, submitted, 2015.

7.1 Introduction

Visibility histograms (VHs) are effective visual feedback in providing meaningful information to the user about the impact of specific volume manipulations on the resulting visualization [102]. Many investigators have leveraged the VH to enhance the Transfer Function (TF) design with automatic TF optimization to ensure the visibility of regions of interest (ROIs) [103, 104, 111] or its use in multi-modality medical image volumes [121]. Unfortunately, the high computational cost and large memory requirement limit its application to medical image volumes that have large intensity ranges and volume dimensions. Figure 7.1 shows the computation of the VHs for a medical image volume; it is necessary to compute the visibilities of every voxel and structure, including the lungs, muscle, and bone, as well as a histogram that represents their distributions along the intensity range (histogram bins). During histogram construction, the number of bins is the parameter that has the major impact on the computational cost. Prior investigators [102, 103, 111, 121] have improved the computational performance by reducing the bin size and partitioning the intensity ranges to a smaller number of fixed bin sizes. However, such an *equal* binning (EB) technique fails to accurately represent the underlying distribution of its full-bin (FB) counterpart; this is shown by the missing peak in EB with 64 bins (64 EB-VH) that is visible in FB-VH with 4096 bins (4096 FB-VH) in Figure 7.1.

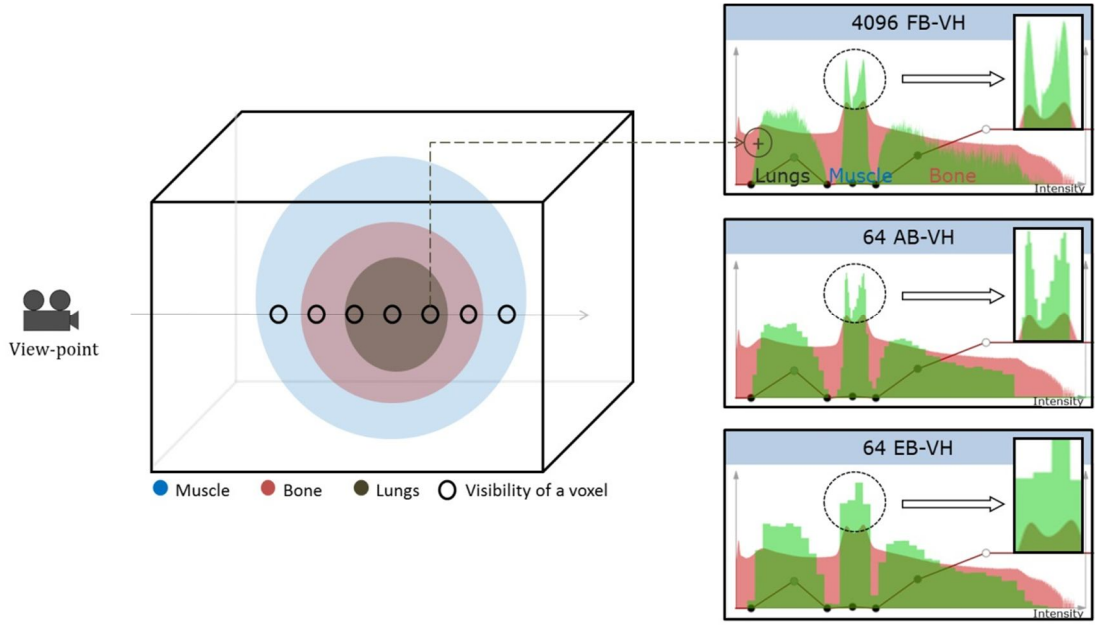


Figure 7.1: VH construction with 3 different binning schemes. Note that AB with 64 bins (64 AB-VH) is able to preserve the major distribution of the intensity ranges when compared to its FB counterpart with 4096 bins (4096 FB-VH) but EB with 64 bins (64 EB-VH) only represents a single peak.

In this chapter, we propose an efficient computation of VHs by adaptively binning (AB) them with a cluster analysis algorithm. In our algorithm, the voxels in an image volume are clustered into a smaller number of related intensity bins. The cluster bins are then used to build an AB-VH that considers density of intensities in the bin allocation. In Figure 7.1, in AB with 64 bins (64 AB-VH), dense intensity ranges, e.g., the muscle, are allocated more bins (see black circles) when compared to the EB counterpart. Due to the reduced number of bins, we are able to leverage the multiple render targets (MRT) extension from modern graphics processing units (GPUs) architecture. This allows a greater number of bins to be stored in memory simultaneously, thereby enabling histograms with 32 bins to be constructed in a single GPU execution (rendering pass) instead of eight rendering passes. We will show the application of our AB algorithm in a variety of common medical image

modalities including high-resolution computed tomography (CT) and magnetic resonance (MR), as well as multi-modality positron emission tomography (PET)-CT.

We adopted well-known and robust generic *K*-means clustering algorithms to support these medical image modalities. *K*-means clustering is capable of partitioning medical images into groups of related voxels that are homogeneous with respect to voxel's attributes, e.g., gray-scale intensity [28, 141] and it has also been used to segment CT [142, 143], PET [144] and MR [145, 146] studies. We note that for VH computation, the primary emphasis is not on the accuracy of the resulting segmentation, but in the ability to accurately represent the distribution of the intensity ranges in the histogram. Our hypothesis is that the AB-VH is able to more accurately preserve visual and numeric resemblances to its FB counterpart when compared to the histogram generated from the conventional EB.

7.2 Related Work

We divide the works related to this chapter into two categories: (i) visibility-driven TF manipulation; and (ii) adaptive binning in histogram construction.

7.2.1 Visibility-driven Transfer Function Manipulation

This content has been already discussed and readers can refer to Section 5.2. We note that all prior related works used medical image volumes as an example or as the experimental data, implying that VH is an important optical property for medical image volumes. In order to achieve efficient VH computation, those studies used conventional binning to down-sample large bin numbers, typically from 4096 (12 bits) into 256 bins (8 bits) [102, 103, 111, 121]. The down-sampling, however, can lose specific intensity distributions from the VH.

7.2.2 Adaptive Binning in Histogram Construction

The algorithm of AB for histogram computation has only been used in a few studies. Gong et al [147] suggested an adaptive histogram based on human perceptual clustering of a color image space. For image retrieval and classification, the bins in the Hue-Value-Chroma (HVC) color space were defined by merging colors that were perceptually indistinguishable by the human eye. Leow and Rui [148] used another binning algorithm that adapted the bins to the color histogram distributions (occurrence) of an image, and performed extensive comparisons with EB counterpart using the large public Corel photo collection. They demonstrated that the AB algorithm produced noticeable improvements in accuracy, efficiency, and memory use for applications including color retention, image retrieval, and classification.

7.3 Methods

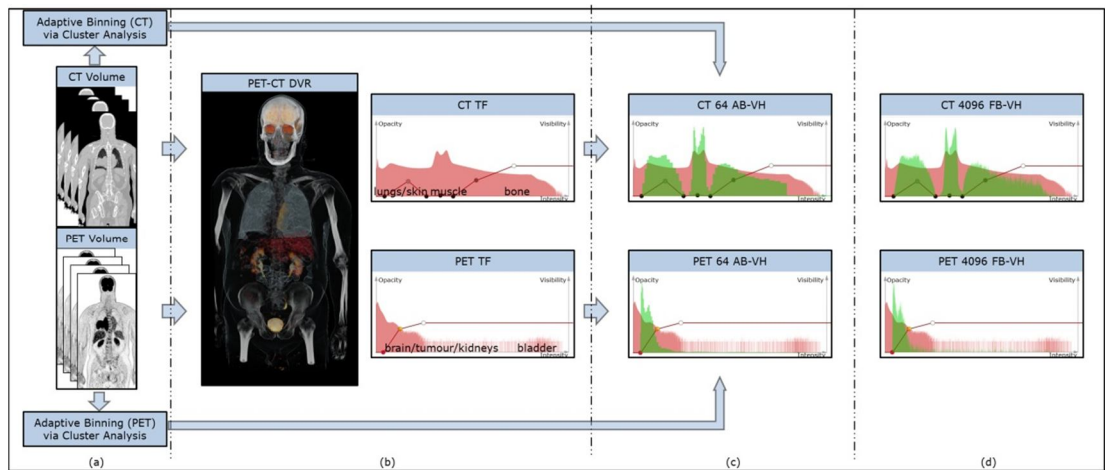


Figure 7.2: An overview of AB-VH applied to the visualization of multi-modality PET-CT image volumes.

Figure 7.2 shows the three major components of the AB-VH applied to multi-modality PET-CT visualization. Prior to direct volume rendering (DVR) and VH computation the PET and

CT image volumes are partitioned into K intensity groups using K -means cluster analysis (Figure 7.2(a)). The image volumes are then rendered separately with their own TFs and fused (data intermixing) into a single visualization, as shown in Figure 7.2(b). The CT TF control line is assigned to three opacity peaks corresponding to the lungs and the skin (first peak), the muscle (second peak), and the bone (third peak). The control line for PET is similarly set to depict structures with high tracer uptake (or functional activity) including the brain, a lung tumor and the kidneys and bladder where the common PET tracer FDG is excreted. The K groups are then used to compute the adaptive VHs (green bars), representing the visibility distributions of the voxels in the image volumes. Figure 7.2(c) shows an example with only 64 bins (64 AB-VH). Figure 7.2(d) shows the FB-VH counterpart as a reference.

7.3.1 Adaptive Binning of Visibility Histogram

Our adaptive bins are derived by clustering of voxels in an image volume into groups of similar intensity values, assigning the bins according to the intensity distributions. We used K -means cluster analysis algorithm [149] to assign each voxel to one of K distinct cluster groups. Each voxel x was assigned to the cluster group c that had the smallest Euclidean distance D between the centroid of the j_{th} cluster c_j and the intensity of x x_i , as given by:

$$c = \operatorname{argmin}_j D(x_i, c_j) = |x_i - c_j|^2. \quad (7.1)$$

The initial centroids of the clusters were randomly defined to be exclusive of each other. The resulting clusters were used to construct the AB-VH such that each bin was assigned to one of the cluster centroids, with its width representing the intensity range of the corresponding cluster. The visibilities of the voxels were computed in the same way as the FB-VH (see section 5.3.3) and added to the adaptive bins belonging to the individual voxels.

We evaluated three commonly used and robust variations of K -means cluster analysis algorithms for our AB. The general K -means uses the average of the voxels in the cluster to calculate the centroids, with random placement of the initial centroids. Since the initialization of the centroids has a significant impact on the clustering results, K -means++ only assigns a single cluster centroid randomly and all other centroids are chosen based on the probability of it being proportional to the Euclidean distance from its closest existing cluster centroid [150]. K -medians differs to K -means in its calculation of the centroids by using the median of the intensity range of the voxels in the cluster instead of the average [151].

7.3.2 Dissimilarity Measurement of Adaptively Binned Visibility Histogram to Full-Bin Counterpart

We measured the numerical dissimilarity of an AB-VH to its full-bin counterpart by re-projecting it back to the full intensity bins in such a way that the visibility values of the adaptive bins were uniformly distributed across the corresponding intensity ranges of the full bins. The visibility dissimilarity V_{dis} between the redistributed AB-VH and its full-bin counterpart was calculated according to:

$$V_{dis} = \frac{\sum_{l=0}^L |FB_l - AB_l|}{\sum_{l=0}^L FB_l} \quad (7.2)$$

where FB_l is the l^{th} visibility of the full bins, AB_l is the l^{th} visibility of the redistributed adaptive bins, and L is the total number of bins. The visibility dissimilarity ranges from 0.0 (perfect similarity) to 1.0 (perfect dissimilarity).

7.3.3 Automatic Transfer Function Optimization using Adaptively Binned Visibility Histogram

TF optimization using VHS explores TF parameter spaces and automatically specifies ideal parameters that ensure the visibilities of structures [102-104, 111, 121]. Since this optimization procedure does not rely on a specific histogram binning scheme, our AB-VH can be deployed in any visibility-driven TF optimization method. We demonstrate the application of our AB-VH to our ROI-based visibility-driven TF optimization method in medical image visualization (see Section 5.3.4). This enables the automated definition of a TF that maximizes the visibility of ROIs. ROIs are defined by the selection of the intensity bins or the use of spatial ROI subsection tools. Adaptive bins belonging to ROIs are then used to compute the visibility tolerance of the energy function.

7.4 Implementation

7.4.1 CUDA-based *K*-Means Cluster analysis

The computational complexity of *K*-means cluster analysis algorithm is $O(n^{k+1} \log n)$, where n is the number of voxels to be clustered [152]. Fortunately, its implementation can be efficiently computed by leveraging the parallel GPU architecture, which produces equivalent results when compared to the conventional sequential CPU implementation [153-155]. We used the Compute Unified Device Architecture (CUDA)-based *CAMPAIGN* framework [155] - clustering algorithms for massively parallel architectures including GPU nodes, to develop our three *K*-means variations.

7.4.2 Visibility Histogram

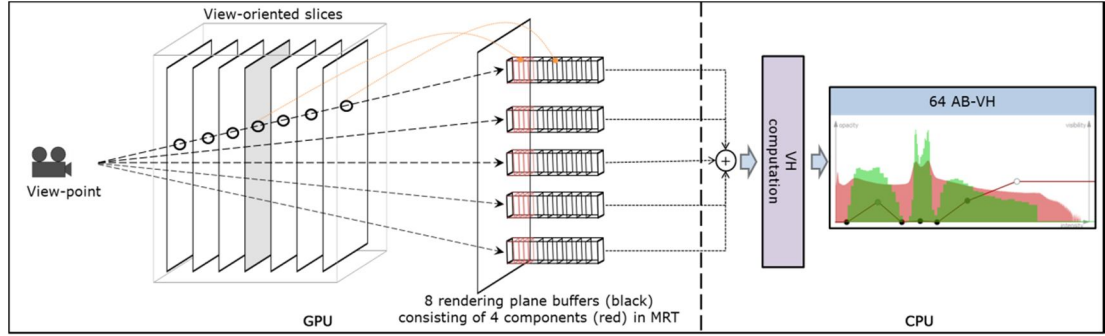


Figure 7.3: GPU-based computation of AB-VH using MRT.

As in Section 6.4, we took advantage of the MRT extension available in modern GPU architecture to efficiently construct the AB-VH. We allocated each component of the buffers to each of the bins in our histogram, e.g., 32 bins to red-green-blue-alpha (RGBA) components in 8 buffers. Such allocation resulted in the number of bin (clusters) being proportional to the buffer sizes of GPUs, i.e., bin sizes are allocated to 32, 64 to 256. Figure 7.3 shows the AB-VH construction procedure. On the GPU side, an image volume was rendered from a given view-point using its view-aligned slices. Each slice was used to compute the visibility of its voxels. All the visibilities (black circles) starting from a view-point to each pixel of the rendering plane buffer were accumulated into the corresponding component bins. The resulting visibility rendering plane buffers were transferred to CPU memory and converted to a histogram representing their visibility distribution (AB-VH). With only a single rendering pass we were able to construct a histogram with 32 bins for a single image volume and 64 bins with one additional rendering pass. For single-modality image volumes with 4096 bins, 128 rendering passes were required; 256 passes were required for the dual-modality image volumes. Note that the histogram computations for EB and AB are the same but the AB is better able to preserve the visibility distribution of its full bin counterpart.

7.5 Results

7.5.1 Adaptive Binning on Visibility Histogram

Figure 7.4 presents the results of VH calculations on a CT image volume from AB with K -means++ (AB-K+) in comparison to the conventional intensity down-sampling of EB and also to the original 4096 FB.

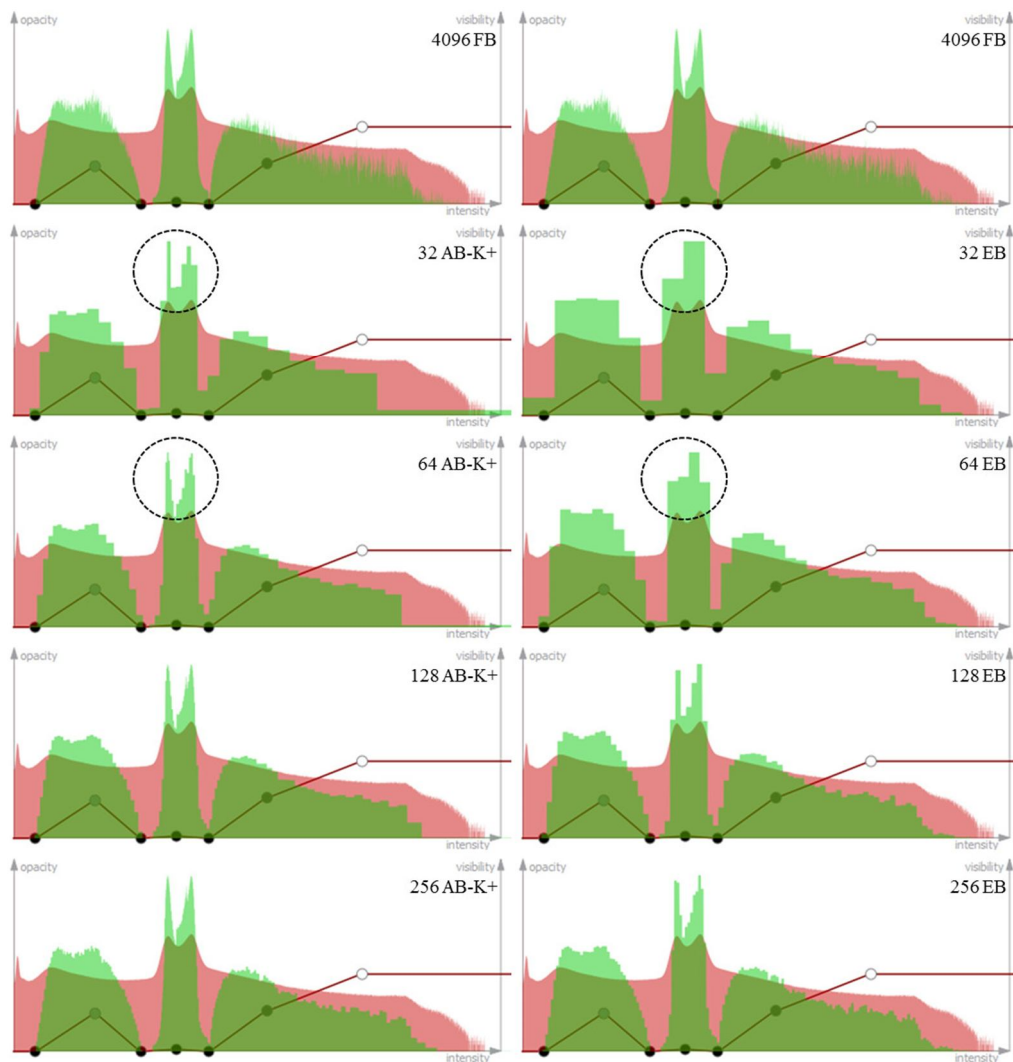


Figure 7.4: FB-VH with 4096 bins of a CT image volume (as in Figure 7.2) compared to its AB-K+ and also to its EB variants. Four different bin sizes of 32, to 64, 128, and 256 (rows two to five, respectively) were computed.

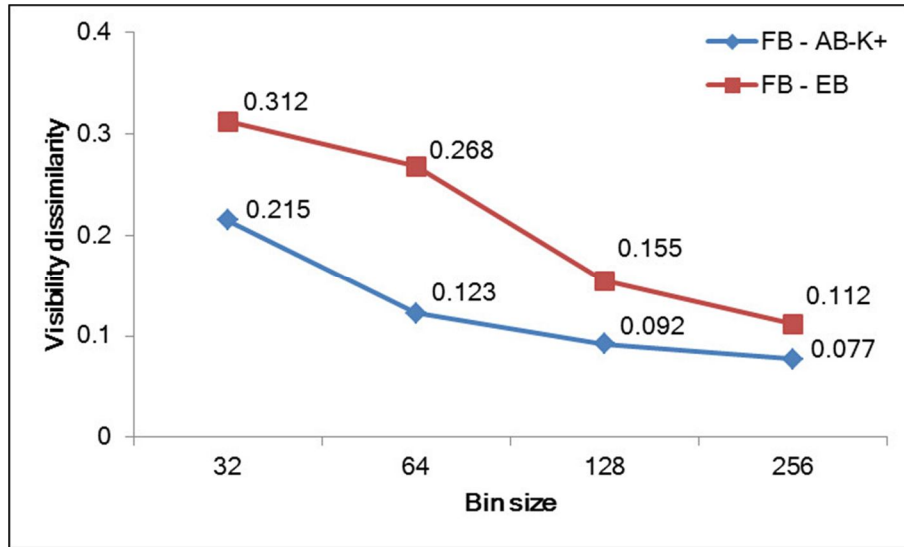


Figure 7.5: Dissimilarities in the VH distribution of AB-K+ and EB relative to FB plotted according to the bin sizes using a CT image volume.

Figure 7.5 plots the dissimilarity indices between the VHs. Four different bin sizes of 32, 64, 128, and 256 were calculated. The differences between AB and EB are clearly seen in the 32 and 64 bin variants (see black dot circles in Figure 7.4).

Figure 7.6 shows dissimilarities in the VHs between each of the clustering-based AB variants (*K*-means (AB-K), AB-K+, and *K*-median (AB-KM)) and FB in comparison to those of EB and FB. Four patient studies from each imaging modality (CT (a), PET (b), and MR (c)) were used and the dissimilarities of each modality were computed by averaging random volume manipulations of view-point and TF changes. EB had the highest dissimilarity to the FB; the AB-K+ obtained the lowest dissimilarity among our proposed AB variants in most cases.

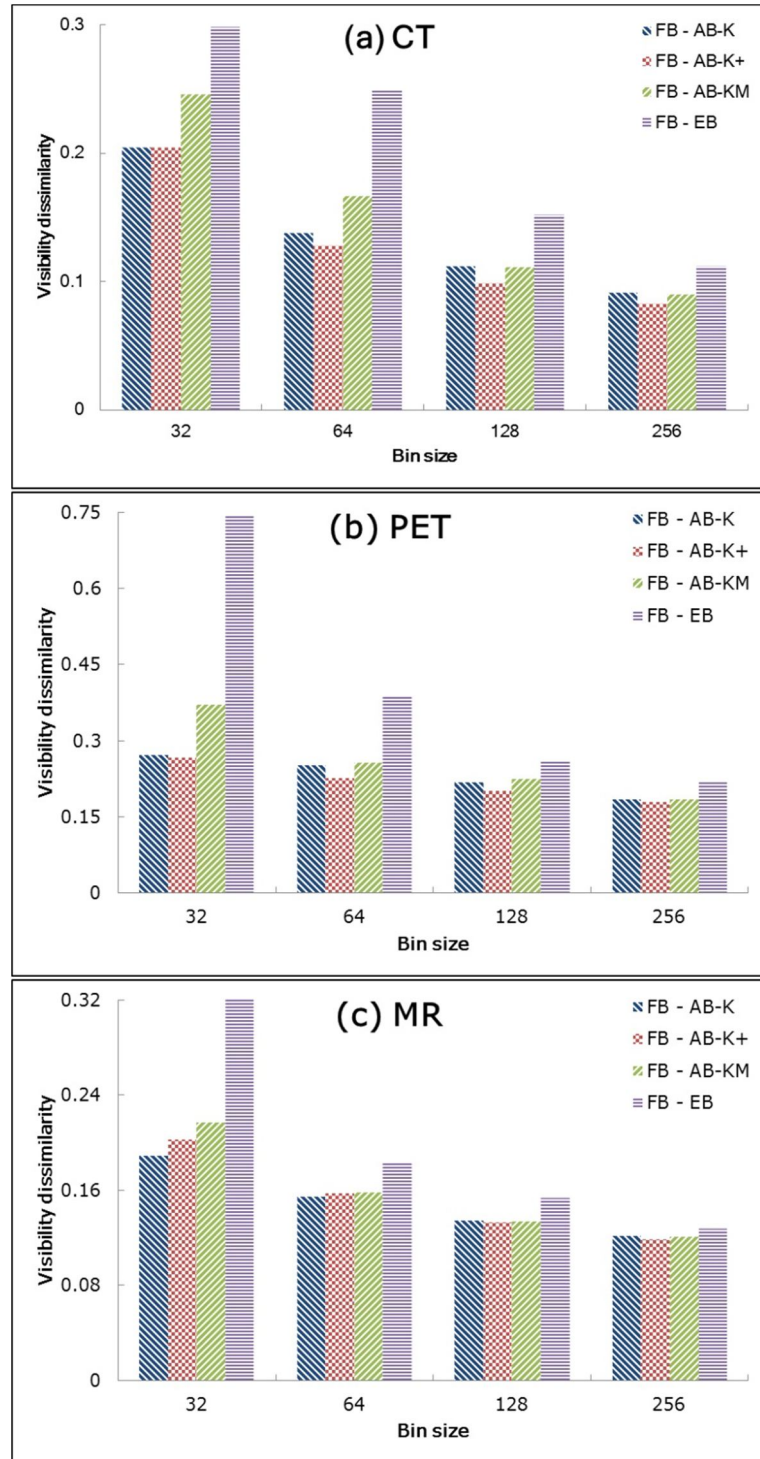


Figure 7.6: The visibility dissimilarities to FB over CT (a) and PET (b), and brain MR (c) using AB algorithms (blue, red, and green bars) in comparison to those of EB (violet bars). For each modality, average of four studies was computed. The bin sizes ranging from 32 to 256 were applied.

7.5.2 Adaptive Binning in Visibility-driven Volume Manipulations

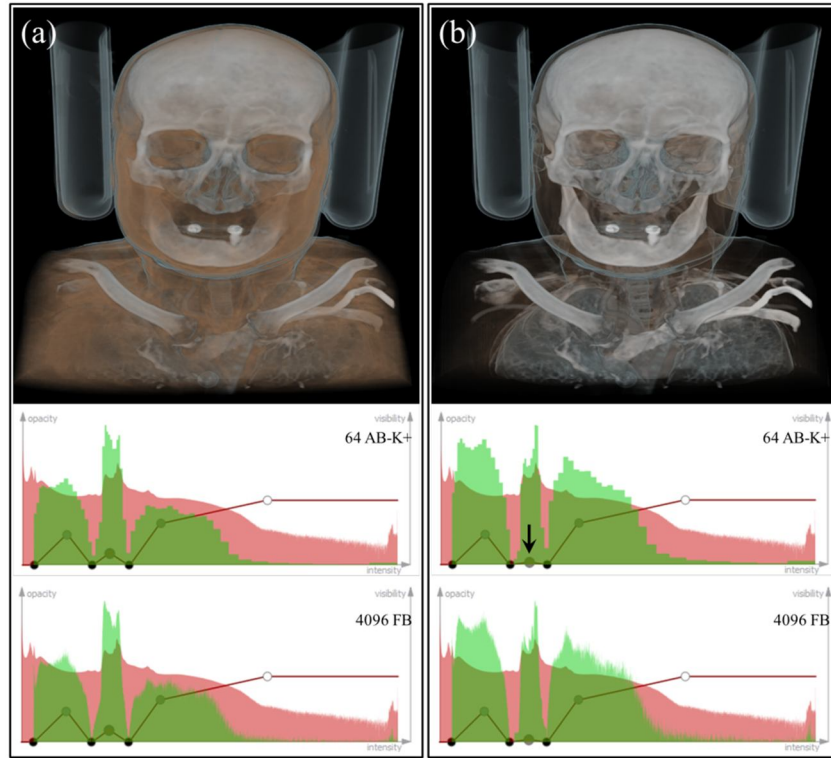


Figure 7.7: A case study of a high-resolution CT image volume with the application of 64 AB-K+ in visibility-driven TF manipulation. The user manipulated the opacities of the muscle (see a black arrow) to reduce its visibility and also increase the visibilities of other structures. Note the visual resemblance of the AB in comparison to its FB counterpart.

Figure 7.7 illustrates the ability of AB in guiding visibility-driven TF manipulation. The improvement of 64 AB-K+ compared to a 4096 FB (second and third rows) is shown with the visualization of a high-resolution CT head scan. In (a), the TF was defined to highlight 3 primary structures: lungs, muscle, and bones of the shoulders. However, due to the dominant visibility of the muscle, the lungs and bone are barely visible. In (b), the TF was manipulated to reduce the muscle visibility (indicated by a black arrow) and so the resulting visualization shows more of the lungs and shoulders. This example shows that the AB-VH is capable of accurately representing the occlusion patterns during TF manipulations despite only using 64 bins instead of the full 4096. The computed dissimilarity index between the AB and FB VHs

were 0.109 in Figure 7.7(a) and 0.105 in Figure 7.7(b); this numerical dissimilarity corresponded to the visual similarity.

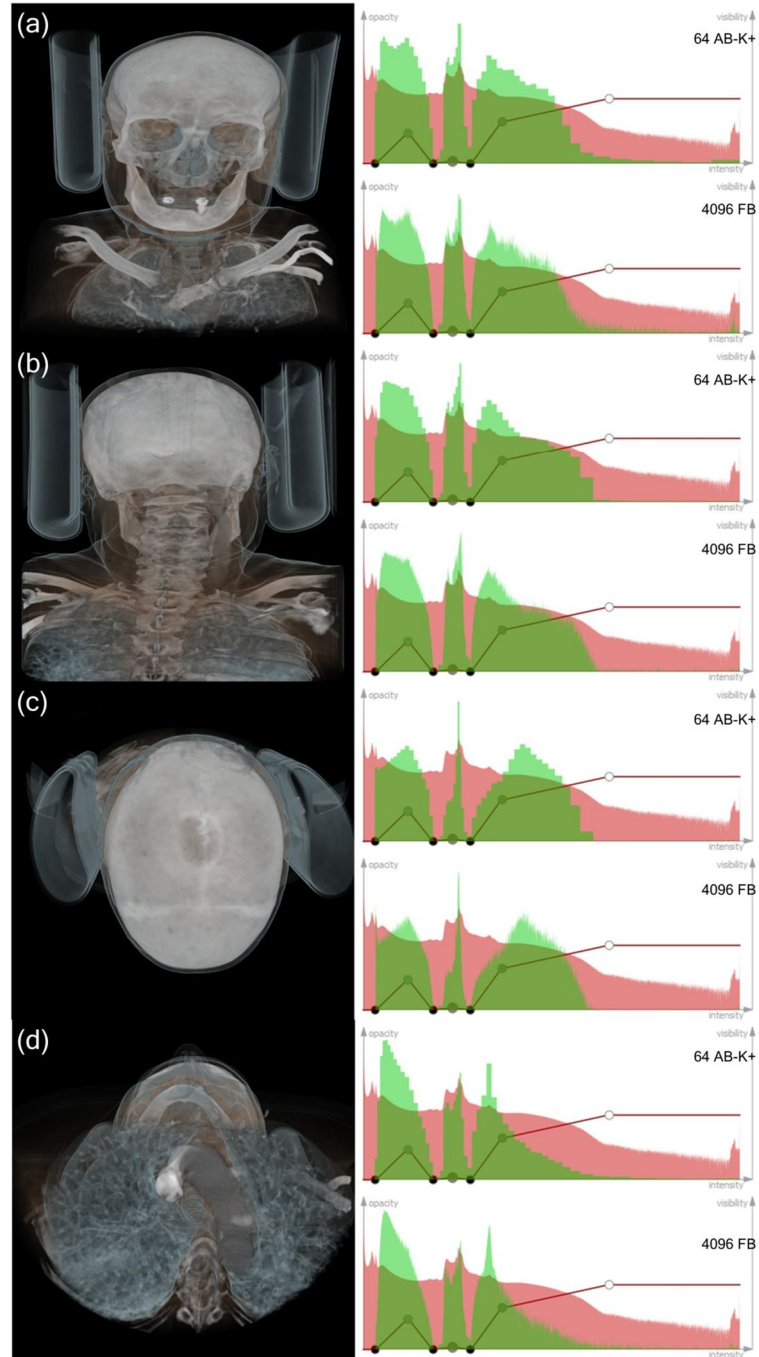


Figure 7.8: View-point manipulations during the visualization of a high-resolution CT study. The left column shows the visualizations and the right column shows AB-VHs (top) and FB counterparts (bottom).

A useful feature of the VH is its view dependency, which computes the visibility according to the user's view-point. Figure 7.8 shows the resulting VHs of 64 AB-K+ and 4096 FB in different view-points. Regardless of the view-points, the AB approach was able to accurately represent the structures that were visible in the resulting visualizations. The average dissimilarity index across the four views was 0.1.

In Figure 7.9, a brain MR image volume was clipped to display the internal structure of the brain; the TF was defined to visualize the white matter. The visibility distribution of 64 AB-K was consistent with the structures that were visible in the resulting visualization (see three visibility peaks corresponding to (i) the ventricles and the air in the sinuses, (ii) the lobes of the brain (ii), and (iii) the surface of the scalp).

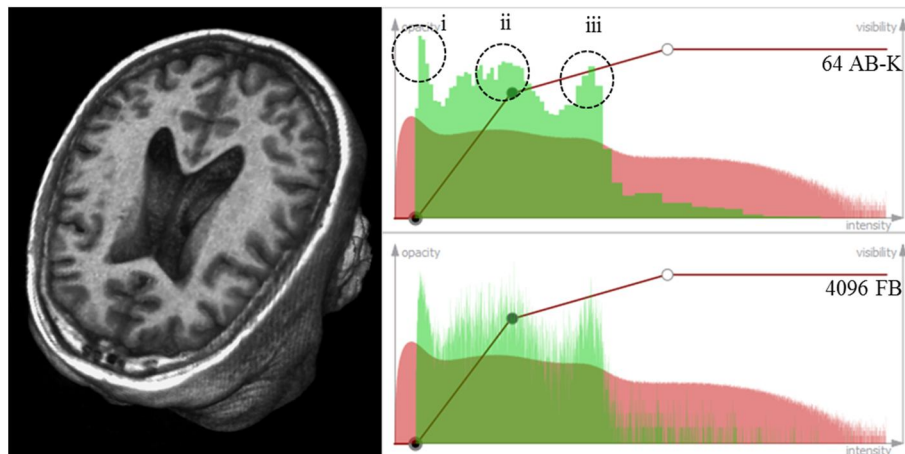


Figure 7.9: A volume clipped brain MR visualization (left column) using 64 AB-K (top row) in comparison to FB (bottom row).

7.5.3 Adaptive Binning in Automatic Visibility-driven Transfer Function Manipulations

We evaluated the use of AB-K+ in automatic visibility-driven TF manipulations with varying bin sizes; the results are shown in Table 7.1. We measured the visibility dissimilarity indices of the visibilities between AB and its FB counterpart in both the ROI-based TF optimization (described in section 7.3.3) and view-independent TF definition using 6 view-point locations [102]. The dissimilarity of the optimized opacity parameters, ranging from 0 to 255, was also compared. The results show that the AB with 64 bins was able to deliver comparable results produced by the FB e.g., the visibility dissimilarities of 0.111 and the opacity dissimilarities of 1.754 in the TF optimization results.

Table 7-1: Dissimilarity indices of the AB-K+ in ROI-based TF optimization and view-independent TF definition, among different bin sizes.

CT volume		32	64	128	256
ROI-based TF optimization	Visibility Dissimilarity				
	(max = 1)	0.143	0.111	0.089	0.082
	Opacity Dissimilarity				
	(max =255)	2.557	1.754	1.698	1.141
View-independent TF definition	Visibility Dissimilarity				
	(max = 1)	0.213	0.123	0.09	0.08

Figure 7.10 shows the corresponding visualization using the same TF optimization algorithm (section 7.3.3) as above with 64 AB-K+ and 4096 FB on a PET-CT study. A key element in

PET-CT visualization is to optimally visualize ROIs from PET while simultaneously introducing the underlying anatomy from CT, without compromising the visibility of the ROI. In the figure, we defined a tumor on the PET image volume inside the lung region (CT) as the ROI (white cuboid). Three opacity control points of the initial CT TF in Figure 7.10(a) were then optimized for maximizing the visibility of the PET ROI. The automatic manipulation reduced the occluding lung's opacity and better depicted the tumor. We compared the FB in (b) to the AB in (c) and noted that they were visually identical.

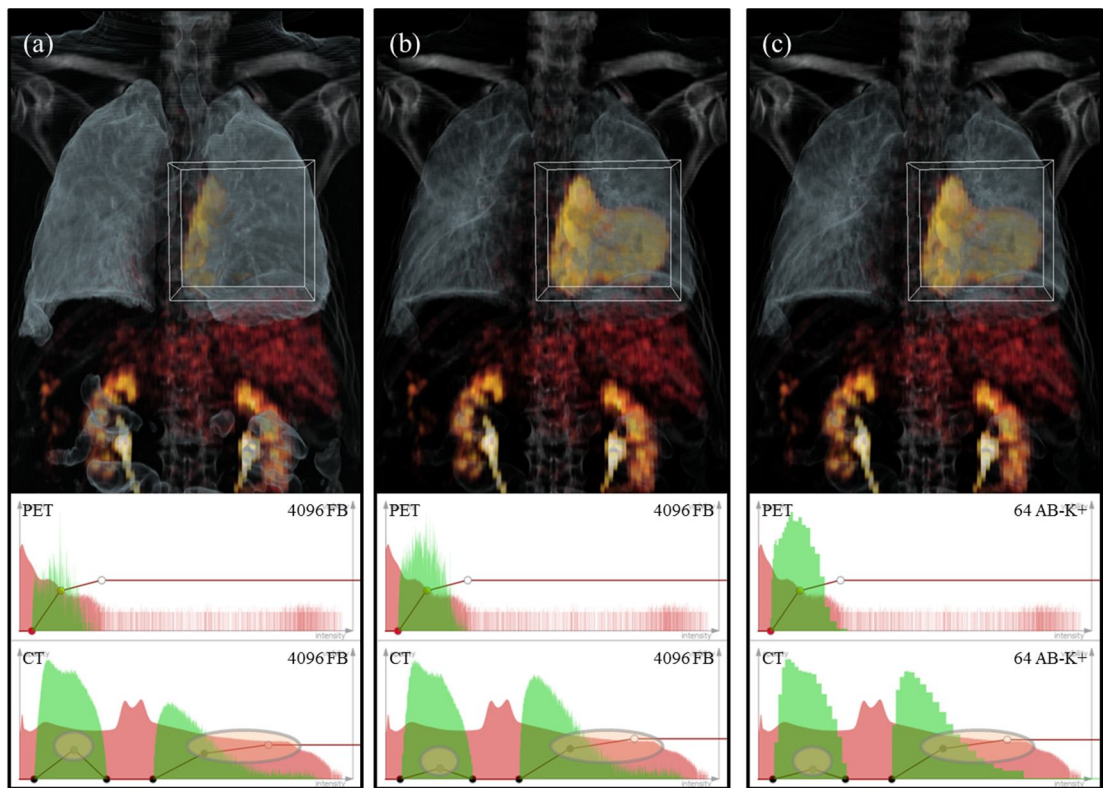


Figure 7.10: TF optimization results using a 64 AB-K+ and 4096 FB on a multi-modality PET-CT study. The CT TF of an initial visualization in (a) is optimized to maximize the visibility of PET ROI (white cuboid). Although the AB in (c) uses a smaller bin size, its visibility distribution is comparable to that of FB in (b) and the resulting optimized visualization is also consistent.

7.5.4 Computational Efficiency

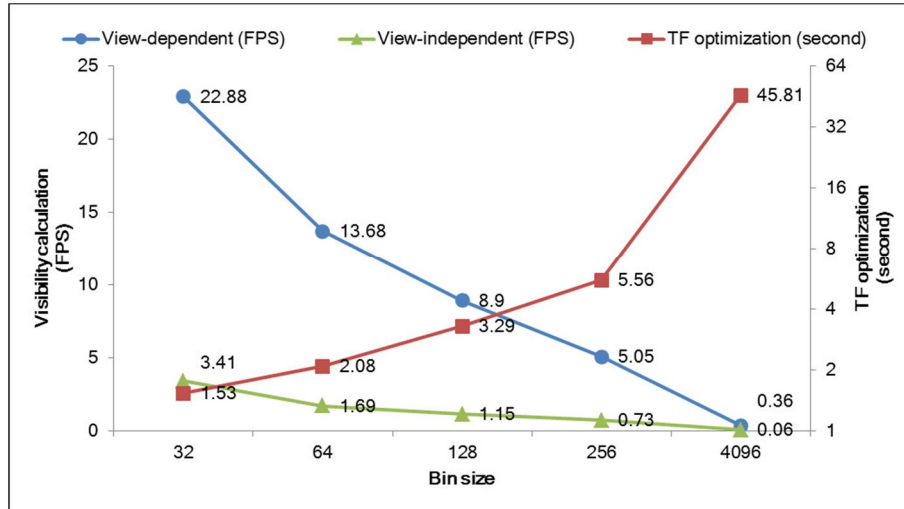


Figure 7.11: frame rate (FPS) of VH calculations (left y-axis) and time (seconds) taken for TF optimization computation (right y-axis) with 5 varying histogram bin sizes.

Figure 7.11 shows the average computing times, using various histogram bin sizes, for the following interactions: (i) calculations of VH from typical volume manipulations measured in frames per second (FPS); (ii) calculations of view-independent VH based on 6 view-point rotations, consistent with previous visualizations as reported by [102], measured in FPS; and (iii) the multi-modality visibility-driven TF optimization calculation, measured in seconds. We used the largest available image volume data (PET-CT with dimensions of $512 \times 512 \times 326$ pixels) in all our measurements to replicate high-end requirements. AB (32 to 256 bins) significantly reduced the computation in all the measures, i.e., from 0.36 FPS of 4096 FB to 22.88 FPS of 32 AB in the VH calculation. Using the default bin size of 64, AB achieved an interactive rate of > 13.7 FPS in the VH calculation and near real-time performance of 2 seconds in the TF optimization. As expected, EB produced identical measurements for all the manipulations. For single-modality image volumes such as MR, all the results were approximately half of that of the multi-modality image volumes.

7.6 Discussion

Our findings from the quantitative dissimilarity evaluation show that AB-VH with 256 bins closely resembled the FB counterpart. These findings are confirmed in Figure 7.5 applying AB-K+, i.e., a negligible dissimilarity index of 0.077. The dissimilarity was more profound with the lowest number of bins, i.e., 0.215 with the 32 bins. The indices from the larger bin sizes were improved, i.e., 0.123 in 64 bins and 0.092 in 128 bins. Note that the dissimilarity indices for the 64 and 128 bins were only higher by a small margin compared to the 256 bins that were used as the default in prior research [102, 103, 111, 121]. The AB results were better in all the bin sizes when compared to the EB counterpart at resembling the FB's visibility distribution, with the smallest improvement being 40.0% at 256 bins while increasing to 46.9% for 64 bins. This was attributed to the adaptive distributions of the intensity bins, which allowed the dense intensity ranges representing the majority of the voxels in the image volume to be allocated with a large proportion of the bins while sparse intensity ranges were allocated with a smaller portion of bins.

The visual representation of the VH with AB produced better approximation to its FB counterpart when compared to EB, in particular with lower bin sizes; this was consistent with the quantitative dissimilarity indices. Even with the lowest setting of 32 bins, AB-VH was able to maintain major patterns, indicated by peaks in Figure 7.4, in the visibility distributions. These results suggest that from 64 bins onwards, our clustering-based AB was able to produce low dissimilarities consistently while retaining visual resemblance to the primary bin distributions. Note that the visual representation of the VH is important for its use in guiding effective TF manipulation and thus producing desired visualization results, as exemplified in Figures 7.7 and 8.

We showed that AB algorithms achieved higher similarities to its FB counterpart in the visibility distribution comparison across all modalities (Figure 7.6). Among the ABs, AB-K+ had better performances in almost every case; AB-K was better only on MR image volumes with the smaller bins of 32 and 64. We used 64 AB-K+ as a default binning scheme in visibility-driven manipulations (section 7.5.2 and 3), with the following reasons. In every modality, the AB-VHs with 64 bin size retained comparatively high similarities to FB, e.g., 0.154 of 64 AB-K+ in MR. The most obvious improvements among all the bin sizes were shown in 64 bins. AB with 64 bins was able to generate almost equivalent similarity results to EB with 256 bins used in prior work [102, 103, 111, 121], e.g., 0.127 of 64 AB-K+ and 0.117 of 256 EB in CT.

We observed that for PET, the visibility dissimilarities to FB were higher than those of the other medical modalities. This was due to the fact that the majority of voxels (structures) were placed in the narrow intensity ranges, for instance from 140 to 948 in Figure 7.2, and a smaller number of bins were used in expressing the visibility distribution when compared to those of the other medical modalities. Nevertheless, we note that the dissimilarities with AB were much lower than those with its EB counterpart e.g., 0.276 of AB-K+ and 0.744 of EB in 32 bins.

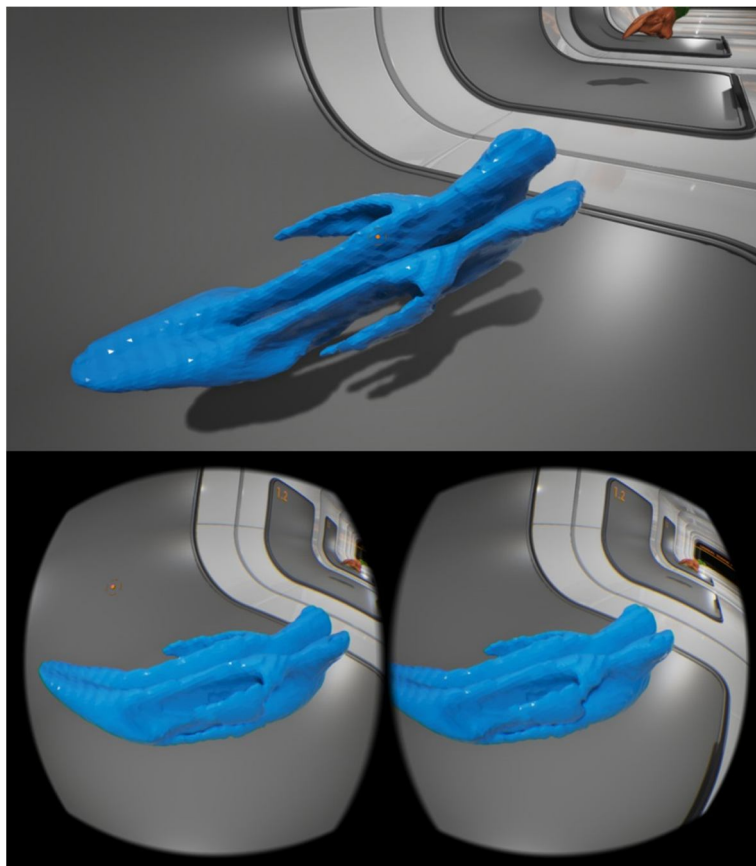
Although clustering added additional complexity to our visualization, it was performed as a pre-process as AB was a static requirement during real-time histogram construction. *K*-means cluster analysis was selected for its broad medical imaging capability and our application produced robust and accurate results. The clustering algorithm can be replaced with modality-specific equivalent that can potentially result in the performance gains.

In this chapter, we only applied conventional 1D TF to all our renderings to demonstrate the capabilities of AB-VH. This method, however, is not restricted to 1D TF and can support multi-dimensional TF manipulations.

7.7 Conclusions

Our results show that a representative VH can be computed via a process of adaptive binning, where automated cluster analysis is used to group intensity ranges in a smaller number of bins. This can then be used to efficiently perform visibility-driven volume manipulations. Our GPU implementation enabled efficient VH construction and its subsequent real-time volume manipulation. Visual and numerical comparisons of our proposed AB-VH with conventional down-sampling showed that our method provided higher accuracy in VH construction and subsequent visualization manipulations.

8. Conclusions



3D volume rendering of a nasal cavity medical data using Oculus Rift

Interactive direct volume rendering (DVR) visualization has become an important tool for efficient data exploration in the medical domain. This thesis addressed the several technical issues pertaining to DVR specifically for the medical domain and proposed further enhancements to improve its utility.

We addressed the lack of volumetric contextual information in established 2D cross-sectional view plane approaches (Chapter 4). Our occlusion and slice-based volume rendering augmentation (OSVRA) visualization automatically augmented a 2D slice of interest (SOI) with the relevant 3D structural context, without impairing the view of the SOI. OSVRA provided accurate spatial location of regions of interest (ROIs) in the SOI and demonstrated their relationships with surrounding structures. An imaging specialist assessed OSVRA as being clinically useful for his lung cancer PET-CT image interpretation workflow.

We also proposed and developed a solution for the time-consuming process of manually specifying the rendering parameters (Chapter 5). Our visibility-driven DVR automation method optimized the rendering parameters to generate visualizations of 3D ROIs while preserving the surrounding structures without compromising the visibility of the ROIs.

We also addressed the greater complexity in managing the rendering parameters in temporal imaging visualization (Chapter 6). Our temporal DVR automation enabled ROIs tracking across the temporal data and their simultaneous visualization under the consistent context of surrounding structures.

We improved the efficiency of VH computation, thereby increasing the applicability of our proposed visibility-driven DVR automations. Our adaptive binning scheme enabled the VH construction using a smaller number of bins while preserving the visibility distribution of the full bin counterpart. Adaptively binning VHs (AB-VHs) significantly improved the computation efficiency of the VHs and enabled real-time visibility-driven DVR visualization and automation with complex imaging data.

8.1 Future Work

There are a number of interesting areas for further development of the visualization approaches presented in this thesis. The visualization approaches are ideally applicable to clinical routine with PET-CT imaging where clinical experts want to inspect sites of disease in PET within the 3D spatial context of high resolution anatomy provided by CT. Although the proposed approaches were mainly presented for PET-CT image volumes, there are no modality-specific parameter settings, as mentioned in the Discussion section of each approach. As such our approaches may be adapted for any image modality data that can be visualized in either ROI-based volume rendering (e.g., PET-MR) or slice-based volume rendering (e.g., CT angiography). Therefore the performance and usability of our approaches with different medical image modalities can be investigated as future work.

Our user study of OSVRA approach (in Chapter 4) identified a number of its potential clinical applications and we are now actively pursuing these in collaboration with two other clinical sites. We intend to explore OSVRA visualization in other diseases including soft tissue sarcomas and the lymphomas.

Virtual Reality (VR) is rapidly gaining attraction in the medical community as researchers and clinicians become aware of its potential benefits [156]. We believe that our methods

when combined with VR will permit improved capabilities for medical imaging visualizations with benefits such as: (i) immersive environments from VR will enable better understanding of the relative 3D context and localization of the features of interest; and (ii) sensory devices of VR facilitate the exploration and interaction of volume rendering. There are several challenges that need to be addressed for broader application of VR for medical imaging visualization. Aside from the known technical limitations of VR, such as sensor navigation devices having inadequate robustness, the large image size of medical imaging data is a major challenge that needs to be addressed as future work.

We can improve the separation capability in the structure-level analysis of OSVRA by extending the 1D occlusion distance histogram along the number of dimensions. The multi-dimensional occlusion distance histograms can be constructed with additional attributes extracted from image volumes; and clustering of their extended histogram space may result in better structure separation. As an example, a 2D histogram can be comprised of occlusion distance and intensity and its space can be clustered by using Gaussian Mixture Modeling (GMM) [128].

We can introduce adaptive TF initialization into our DVR automation methods to avoid the local minima that may occur during TF optimization. In this thesis, a progressive search of optimal TFs was used since the large size of the TF space made exhaustive search computationally difficult and prohibitive. The progressive search explored the TF space in directions that gradually decreased the value of the energy function. The initialization with a single (static) TF to all visualization optimizations would then lead to local minima. This TF initialization can be improved by introducing ray profile analysis that enables the identification of the structures along a viewing ray and mapping the identification to TFs [89, 157, 158]. It is expected that the adaptive TF initialization will reduce the likelihood of being trapped in the local minima and thus increase the chance to reach optimal visualizations.

9. List of References

- [1] J. D. Foley, "Scientific-Data Visualization Software - Trends and Directions," *International Journal of Supercomputer Applications and High Performance Computing*, 4 (2), pp. 154-7, Sum 1990.
- [2] K. Doi, "Computer-aided diagnosis in medical imaging: Historical review, current status and future potential," *Computerized Medical Imaging and Graphics*, 31 (4-5), pp. 198-211, Jun-Jul 2007.
- [3] K. Doi, "Current status and future potential of computer-aided diagnosis in medical imaging," *British Journal of Radiology*, 78 pp. S3-S19, 2005.
- [4] B. Preim and D. Bartz, "Visualization in medicine: theory, algorithms, and applications," Morgan Kaufmann, 2007.
- [5] A. van der Gijp, M. van der Schaaf, I. van der Schaaf, J. Huige, C. Ravesloot, J. van Schaik, and T. J. ten Cate, "Interpretation of radiological images: towards a framework of knowledge and skills," *Advances in Health Sciences Education*, 19 (4), pp. 565-80, 2014.
- [6] D. Rinewalt, B. W. Williams, A. P. Reeves, P. Shah, E. Hong, and J. L. Mulshine, "Evaluation of an Interactive Science Publishing Tool: Toward Enabling Three-Dimensional Analysis of Medical Images," *Academic Radiology*, 22 (3), pp. 380-6, Mar 2015.
- [7] A. Mallouhi, M. Schocke, W. Judmaier, C. Wolf, A. Dessl, B. V. Czermak, P. Waldenberger, and W. R. Jaschke, "3D MR Angiography of Renal Arteries: Comparison of Volume Rendering and Maximum Intensity Projection Algorithms 1," *Radiology*, 223 (2), pp. 509-16, 2002.
- [8] H. Pfister, B. Lorensen, W. Schroeder, C. Bajaj, and G. Kindlmann, "The transfer function bake-off," *Visualization 2000, Proceedings*, pp. 523-6, 2000.
- [9] S. Y. Hu, E. A. Hoffman, and J. M. Reinhardt, "Automatic lung segmentation for accurate quantitation of volumetric X-ray CT images," *Ieee Transactions on Medical Imaging*, 20 (6), pp. 490-8, Jun 2001.
- [10] W. Jentzen, L. Freudenberg, E. G. Eising, M. Heinze, W. Brandau, and A. Bockisch, "Segmentation of PET volumes by iterative image thresholding," *Journal of Nuclear Medicine*, 48 (1), pp. 108-14, Jan 2007.
- [11] J. A. Maintz and M. A. Viergever, "A survey of medical image registration," *Medical image analysis*, 2 (1), pp. 1-36, 1998.
- [12] B. Zitova and J. Flusser, "Image registration methods: a survey," *Image and Vision Computing*, 21 (11), pp. 977-1000, Oct 1 2003.
- [13] Q. Zhang, R. Eagleson, and T. M. Peters, "Volume Visualization: A Technical Overview with a Focus on Medical Applications," *Journal of Digital Imaging*, 24 (4), pp. 640-64, Aug 2011.

- [14] E. Gobbetti, F. Marton, and J. A. I. Guitian, "A single-pass GPU ray casting framework for interactive out-of-core rendering of massive volumetric datasets," *Visual Computer*, 24 (7-9), pp. 797-806, Jul 2008.
- [15] J. Kruger and R. Westermann, "Acceleration techniques for GPU-based volume rendering," *Ieee Visualization 2003, Proceedings*, pp. 287-92, 2003.
- [16] H. Scharsach, "Advanced GPU raycasting," *Proceedings of CESC*, 5 pp. 67-76, 2005.
- [17] V. Vezhnevets and V. Konouchine, "GrowCut: Interactive multi-label ND image segmentation by cellular automata," *Proc. of Graphicon*, 2005.
- [18] C. D. Hansen and C. R. Johnson, "The visualization handbook," Academic Press, 2005.
- [19] G. T. Herman, "Fundamentals of computerized tomography: image reconstruction from projections," Springer Science & Business Media, 2009.
- [20] T. G. Feeman, "The mathematics of medical imaging: a beginner's guide," Springer Science & Business Media, 2010.
- [21] W. Hollingworth, C. J. Todd, M. I. Bell, Q. Arafat, S. Girling, K. R. Karia, and A. K. Dixon, "The diagnostic and therapeutic impact of MRI: an observational multi-centre study," *Clinical Radiology*, 55 (11), pp. 825-31, Nov 2000.
- [22] F. G. Shellock and J. V. Cruess, "Temperature, Heart-Rate, and Blood-Pressure Changes Associated with Clinical Mr Imaging at 1.5-T," *Radiology*, 163 (1), pp. 259-62, Apr 1987.
- [23] G. D. Rubin, J. Leipsic, U. J. Schoepf, D. Fleischmann, and S. Napel, "CT Angiography after 20 Years: A Transformation in Cardiovascular Disease Characterization Continues to Advance," *Radiology*, 271 (3), pp. 633-52, Jun 2014.
- [24] H. Zaidi and I. El Naqa, "PET-guided delineation of radiation therapy treatment volumes: a survey of image segmentation techniques," *European Journal of Nuclear Medicine and Molecular Imaging*, 37 (11), pp. 2165-87, Nov 2010.
- [25] D. W. Townsend and T. Beyer, "A combined PET/CT scanner: the path to true image fusion," *British Journal of Radiology*, 75 pp. S24-S30, 2002.
- [26] D. W. Townsend, T. Beyer, and T. M. Blodgett, "PET/CT scanners: A hardware approach to image fusion," *Seminars in Nuclear Medicine*, 33 (3), pp. 193-204, Jul 2003.
- [27] A. Rosset, L. Spadola, L. Pysher, and O. Ratib, "Informatics in radiology (infoRAD) - Navigating the fifth dimension: Innovative interface for multidimensional multimodality image navigation," *Radiographics*, 26 (1), pp. 299-308, Jan-Feb 2006.
- [28] D. L. Pham, C. Y. Xu, and J. L. Prince, "Current methods in medical image segmentation," *Annual Review of Biomedical Engineering*, 2 pp. 315-+, 2000.
- [29] R. Adams and L. Bischof, "Seeded region growing," *Pattern Analysis and Machine Intelligence, IEEE Transactions on*, 16 (6), pp. 641-7, 1994.
- [30] J. Canny, "A Computational Approach to Edge-Detection," *Ieee Transactions on Pattern Analysis and Machine Intelligence*, 8 (6), pp. 679-98, Nov 1986.

- [31] K. S. Chuang, H. L. Tzeng, S. Chen, J. Wu, and T. J. Chen, "Fuzzy c-means clustering with spatial information for image segmentation," *Computerized Medical Imaging and Graphics*, 30 (1), pp. 9-15, Jan 2006.
- [32] J. Shi and J. Malik, "Normalized cuts and image segmentation," *Pattern Analysis and Machine Intelligence, IEEE Transactions on*, 22 (8), pp. 888-905, 2000.
- [33] M. E. Leventon, W. E. L. Grimson, and O. Faugeras, "Statistical shape influence in geodesic active contours," *Ieee Conference on Computer Vision and Pattern Recognition, Proceedings, Vol I*, pp. 316-23, 2000.
- [34] W. R. Crum, T. Hartkens, and D. L. G. Hill, "Non-rigid image registration: theory and practice," *British Journal of Radiology*, 77 pp. S140-S53, 2004.
- [35] S. Klein, M. Staring, K. Murphy, M. A. Viergever, and J. P. W. Pluim, "elastix: A Toolbox for Intensity-Based Medical Image Registration," *Ieee Transactions on Medical Imaging*, 29 (1), pp. 196-205, Jan 2010.
- [36] A. Kumar, "A Graph-based Approach for the Retrieval of Multi-modality Medical Images," Doctor of Philosophy, The University of Sydney, 2013.
- [37] N. Max, "Optical models for direct volume rendering," *Visualization and Computer Graphics, IEEE Transactions on*, 1 (2), pp. 99-108, 1995.
- [38] J. F. Blinn, "Models of light reflection for computer synthesized pictures," *ACM SIGGRAPH Computer Graphics*, 1977.
- [39] B. T. Phong, "Illumination for Computer Generated Pictures," *Communications of the Acm*, 18 (6), pp. 311-7, 1975.
- [40] M. Hadwiger, J. M. Kniss, C. Rezk-Salama, D. Weiskopf, and K. Engel, "Real-time volume graphics," AK Peters, Ltd., 2006.
- [41] R. Fernando, E. Haines, and T. Sweeney, "GPU gems: programming techniques, tips, and tricks for real-time graphics," *Dimensions*, 7 (4), p. 816, 2001.
- [42] M. Pharr and R. Fernando, "Gpu gems 2: programming techniques for high-performance graphics and general-purpose computation," Addison-Wesley Professional, 2005.
- [43] B. Lichtenbelt, R. Crane, and S. Naqvi, "Introduction to volume rendering," Prentice-Hall, Inc., 1998.
- [44] A. VanGelder and K. Kim, "Direct volume rendering with shading via three-dimensional textures," *1996 Symposium on Volume Visualization, Proceedings*, pp. 23-&, 1996.
- [45] G. K. a. J. W. Durkin, "Semi-automatic generation of transfer functions for direct volume rendering," *Proc. IEEE Symp. Volume visualization*, 1998.
- [46] W. L. Cai and G. Sakas, "Data intermixing and multi-volume rendering," *Computer Graphics Forum*, 18 (3), pp. 359-68, 1999.
- [47] J. Kim, Y. Hu, S. Eberl, D. Feng, and M. Fulham, "A fully automatic bed/linen segmentation for fused PET/CT MIP rendering," *Society of Nuclear Medicine Annual Meeting Abstracts*, 2008.

- [48] D. S. Marcus, T. H. Wang, J. Parker, J. G. Csernansky, J. C. Morris, and R. L. Buckner, "Open Access Series of Imaging Studies (OASIS): cross-sectional MRI data in young, middle aged, nondemented, and demented older adults," *Journal of cognitive neuroscience*, 19 (9), pp. 1498-507, 2007.
- [49] (03/17). *Osirix*. Available: <http://www.osirix-viewer.com/datasets/>
- [50] J. Meyer-Spradow, T. Ropinski, J. Mensmann, and K. Hinrichs, "Voreen: A rapid-prototyping environment for ray-casting-based volume visualizations," *Computer Graphics and Applications, IEEE*, 29 (6), pp. 6-13, 2009.
- [51] J. S. Prassni, T. Ropinski, J. Mensmann, and K. Hinrichs, "Shape-based Transfer Functions for Volume Visualization," *Ieee Pacific Visualization Symposium 2010*, pp. 9-16, 2010.
- [52] R. Bruder, P. Jauer, F. Ernst, L. Richter, and A. Schweikard, "Real-time 4D ultrasound visualization with the Voreen framework," *ACM SIGGRAPH 2011 Posters*, 2011.
- [53] K. T. Nguyen, H. Gauffin, A. Ynnerman, and T. Ropinski, "Quantitative Analysis of Knee Movement Patterns through Comparative Visualization}}," *Visualization in Medicine and Life Sciences*}, 2014.
- [54] J. S. Prassni, T. Ropinski, and K. Hinrichs, "Uncertainty-Aware Guided Volume Segmentation," *Ieee Transactions on Visualization and Computer Graphics*, 16 (6), pp. 1358-65, Nov-Dec 2010.
- [55] J. Kniss, G. Kindlmann, and C. Hansen, "Interactive volume rendering using multi-dimensional transfer functions and direct manipulation widgets," *Visualization 2001, Proceedings*, pp. 255-62, 2001.
- [56] C. Correa and K.-L. Ma, "Size-based transfer functions: A new volume exploration technique," *Visualization and Computer Graphics, IEEE Transactions on*, 14 (6), pp. 1380-7, 2008.
- [57] J. J. Caban and P. Rheingans, "Texture-based transfer functions for direct volume rendering," *Visualization and Computer Graphics, IEEE Transactions on*, 14 (6), pp. 1364-71, 2008.
- [58] J. Kim, S. Eberl, and D. Feng, "Visualizing dual-modality rendered volumes using a dual-lookup table transfer function," *Computing in Science & Engineering*, 9 (1), pp. 20-5, Jan-Feb 2007.
- [59] I. Viola, A. Kanitsar, and M. E. Groller, "Importance-driven feature enhancement in volume visualization," *Ieee Transactions on Visualization and Computer Graphics*, 11 (4), pp. 408-18, Jul-Aug 2005.
- [60] C. Y. Ip, A. Varshney, and J. JaJa, "Hierarchical exploration of volumes using multilevel segmentation of the intensity-gradient histograms," *Visualization and Computer Graphics, IEEE Transactions on*, 18 (12), pp. 2355-63, 2012.
- [61] S. Bruckner and M. E. Groller, "Instant Volume Visualization using Maximum Intensity Difference Accumulation," *Computer Graphics Forum*, 28 (3), pp. 775-82, Jun 10 2009.

- [62] B. Tang, Z. Zhou, and H. Lin, "Depth-based feature enhancement for volume visualization," *12th International Conference on Computer-Aided Design and Computer Graphics (CAD/Graphics)*, 2011.
- [63] I. Viola, A. Kanitsar, and M. E. Groller, "Importance-driven volume rendering," *Ieee Visualization 2004, Proceedings*, pp. 139-45, 2004.
- [64] M. Burns, M. Haidacher, W. Wein, I. Viola, and M. E. Groller, "Feature emphasis and contextual cutaways for multimodal medical visualization," the Proceedings of the 9th Joint Eurographics / IEEE VGTC conference on Visualization, 2007.
- [65] J. Diaz, E. Monclus, I. Navazo, and P. Vazquez, "Adaptive Cross-sections of Anatomical Models," *Computer Graphics Forum*, 31 (7), pp. 2155-64, Sep 2012.
- [66] S. Bruckner, S. Grimm, A. Kanitsar, and M. E. Groller, "Illustrative context-preserving exploration of volume data," *Ieee Transactions on Visualization and Computer Graphics*, 12 (6), pp. 1559-69, Nov-Dec 2006.
- [67] A. Tappenbeck, B. Preim, and V. Dicken, "Distance-based transfer function design: Specification Methods and Applications," *SimVis*, 2006.
- [68] J. Zhou, A. Döring, and K. D. Tönnies, "Distance transfer function based rendering," *International Telegraph and Telephone Consultative Committee*, 2004.
- [69] D. Weiskopf, K. Engel, and T. Ertl, "Interactive clipping techniques for texture-based volume visualization and volume shading," *IEEE Transactions on Visualization and Computer Graphics*, 9 (3), pp. 298-312, Jul-Sep 2003.
- [70] S. Islam, D. Silver, and M. Chen, "Volume splitting and its applications," *IEEE Transactions on Visualization and Computer Graphics*, 13 (2), pp. 193-203, 2007.
- [71] K. H. Hohne, M. Bomans, M. Riemer, R. Schubert, U. Tiede, and W. Lierse, "A Volume-Based Anatomical Atlas," *IEEE Computer Graphics and Applications*, 12 (4), pp. 72-8, Jul 1992.
- [72] O. Konrad-Verse, A. Littmann, and B. Preim, "Virtual Resection with a Deformable Cutting Plane," *SimVis*, 2004.
- [73] T. McInerney and S. Broughton, "HingeSlicer: Interactive exploration of volume images using extended 3D slice plane widgets," *Graphics Interface 2006, Proceedings*, pp. 171-8, 2006.
- [74] A. Birkeland, S. Bruckner, A. Brambilla, and I. Viola, "Illustrative Membrane Clipping," *Computer Graphics Forum*, 31 (3), pp. 905-14, Jun 2012.
- [75] R. Liang, Y. Wu, F. Dong, and G. Clapworthy, "Accumulation of local maximum intensity for feature enhanced volume rendering," *The Visual Computer*, 28 (6-8), pp. 625-33, 2012.
- [76] S. Marchesin, J. M. Dischler, and C. Mongenet, "Per-pixel opacity modulation for feature enhancement in volume rendering," *IEEE Transactions on Visualization and Computer Graphics*, 16 (4), pp. 560-70, Jul-Aug 2010.
- [77] F. de Moura Pinto and C. M. Freitas, "Importance-aware composition for illustrative volume rendering," *Graphics, Patterns and Images (SIBGRAPI), 2010 23rd SIBGRAPI Conference on*, 2010.

- [78] C. Rezk-Salama and A. Kolb, "Opacity peeling for direct volume rendering," *Computer Graphics Forum*, 25 (3), pp. 597-606, 2006.
- [79] M. M. Malik, T. M. #246, Iler, and M. E. Gr, "Feature peeling," the Proceedings of Graphics Interface 2007, 2007.
- [80] R. Stokking, K. J. Zuiderveld, H. E. H. Pol, and M. A. Viergever, "Single photon emission photography/magnetic resonance imaging (SPECT/MRI) visualization for frontal-lobe-damaged regions," *Visualization in Biomedical Computing 1994*, 1994.
- [81] P. Hastreiter and T. Ertl, "Integrated registration and visualization of medical image data," *Computer Graphics International, Proceedings*, pp. 78-85, 1998.
- [82] R. Stokking, K. J. Zuiderveld, and M. A. Viergever, "Integrated volume visualization of functional image data and anatomical surfaces using normal fusion," *Human Brain Mapping*, 12 (4), pp. 203-18, Apr 2001.
- [83] R. Bramon, I. Boada, A. Bardera, J. Rodriguez, M. Feixas, J. Puig, and M. Sbert, "Multimodal Data Fusion Based on Mutual Information," *Ieee Transactions on Visualization and Computer Graphics*, 18 (9), pp. 1574-87, Sep 2012.
- [84] H. Hauser, L. Mroz, G. I. Bisch, and M. E. Groller, "Two-level volume rendering," *Ieee Transactions on Visualization and Computer Graphics*, 7 (3), pp. 242-52, Jul-Sep 2001.
- [85] J. Kim, W. Cai, S. Eberl, and D. Feng, "Real-time volume rendering visualization of dual-modality PET/CT images with interactive fuzzy thresholding segmentation," *IEEE Trans Inf Technol Biomed*, 11 (2), pp. 161-9, Mar 2007.
- [86] M. Haidacher, S. Bruckner, A. Kanitsar, and M. E. Gröller, "Information-based Transfer Functions for Multimodal Visualization," *VCBM*, 2008.
- [87] J. Hay and S. Jannedy, "Probabilistic linguistics," Mit Press, 2003.
- [88] T. Scheuermann and J. Hensley, "Efficient Histogram Generation Using Scattering on GPUs," *I3d 2007: Acm Siggraph Symposium on Interactive 3d Graphics and Games, Proceedings*, pp. 33-7, 2007.
- [89] S. Castro, A. König, H. Löffelmann, and E. Gröller, "Transfer function specification for the visualization of medical data," *Vienne University of Technology*, 1998.
- [90] E. Monclús, P.-P. Vázquez, and I. Navazo, "Data-aware picking for medical models," in *Computer Vision, Imaging and Computer Graphics--Theory and Applications*, ed: Springer, 2014, pp. 50-65.
- [91] J. Seo and B. Shneiderman, "Knowledge discovery in high-dimensional data: Case studies and a user survey for the rank-by-feature framework," *Visualization and Computer Graphics, IEEE Transactions on*, 12 (3), pp. 311-22, 2006.
- [92] B. Shneiderman and C. Plaisant, "Strategies for evaluating information visualization tools: multi-dimensional in-depth long-term case studies," *Proceedings of the 2006 AVI workshop on BEyond time and errors: novel evaluation methods for information visualization*, 2006.
- [93] H. Song, J. Yun, B. Kim, and J. Seo, "GazeVis: interactive 3D gaze visualization for contiguous cross-sectional medical images," *Visualization and Computer Graphics, IEEE Transactions on*, 20 (5), pp. 726-39, 2014.

- [94] P. Ellis, "The importance of multidisciplinary team management of patients with non-small-cell lung cancer," *Current Oncology*, 19 (Suppl 1), p. S7, 2012.
- [95] C. Taylor, A. Shewbridge, J. Harris, and J. S. Green, "Benefits of multidisciplinary teamwork in the management of breast cancer," *Breast Cancer: Targets and Therapy*, 5 p. 79, 2013.
- [96] L. G. Brown, "A Survey of Image Registration Techniques," *Computing Surveys*, 24 (4), pp. 325-76, Dec 1992.
- [97] L. Palm Dzung, X. Chenyang, and L. Prince Jerry, "A survey of current methods in medical image segmentation," 1998.
- [98] A. Criminisi, T. Sharp, and A. Blake, "GeoS: Geodesic Image Segmentation," *Computer Vision - Eccv 2008, Pt I, Proceedings*, 5302 pp. 99-112, 2008.
- [99] U. Vovk, F. Pernus, and B. Likar, "A review of methods for correction of intensity inhomogeneity in MRI," *Ieee Transactions on Medical Imaging*, 26 (3), pp. 405-21, Mar 2007.
- [100] G. Kindlmann, R. Whitaker, T. Tasdizen, and T. Moller, "Curvature-based transfer functions for direct volume rendering: Methods and applications," *IEEE Visualization 2003, Proceedings*, pp. 513-20, 2003.
- [101] C. D. Correa and K. L. Ma, "The Occlusion Spectrum for Volume Classification and Visualization," *Ieee Transactions on Visualization and Computer Graphics*, 15 (6), pp. 1465-72, Nov-Dec 2009.
- [102] C. Correa and K.-L. Ma, "Visibility histograms and visibility-driven transfer functions," *Visualization and Computer Graphics, IEEE Transactions on*, 17 (2), pp. 192-204, 2011.
- [103] M. Ruiz, A. Bardera, I. Boada, I. Viola, M. Feixas, and M. Sbert, "Automatic Transfer Functions Based on Informational Divergence," *Ieee Transactions on Visualization and Computer Graphics*, 17 (12), pp. 1932-41, Dec 2011.
- [104] Y. H. Wang, J. Zhang, W. Chen, H. Zhang, and X. B. Chi, "Efficient opacity specification based on feature visibilities in direct volume rendering," *Computer Graphics Forum*, 30 (7), pp. 2117-26, Sep 2011.
- [105] Y. Jung, J. Kim, and D. D. Feng, "Dual-Modal Visibility Metrics for Interactive PET-CT Visualization," *2012 Annual International Conference of the Ieee Engineering in Medicine and Biology Society (Embc)*, pp. 2696-9, 2012.
- [106] I. Viola, M. Feixas, M. Sbert, and M. E. Groller, "Importance-driven focus of attention," *Ieee Transactions on Visualization and Computer Graphics*, 12 (5), pp. 933-40, Sep-Oct 2006.
- [107] S. Bruckner and M. E. Gröller, "Instant volume visualization using maximum intensity difference accumulation," *Computer Graphics Forum*, 2009.
- [108] U. D. Bordoloi and H. W. Shen, "View selection for volume rendering," *IEEE Visualization 2005, Proceedings*, pp. 487-94, 2005.
- [109] G. F. Ji and H. W. Shen, "Dynamic view selection for time-varying volumes," *Ieee Transactions on Visualization and Computer Graphics*, 12 (5), pp. 1109-16, Sep-Oct 2006.

- [110] S. Takahashi, I. Fujishiro, Y. Takeshima, and T. Nishita, "A feature-driven approach to locating optimal viewpoints for volume visualization," *IEEE Visualization 2005, Proceedings*, pp. 495-502, 2005.
- [111] L. Cai, W. L. Tay, B. P. Nguyen, C. K. Chui, and S. H. Ong, "Automatic transfer function design for medical visualization using visibility distributions and projective color mapping," *Computerized Medical Imaging and Graphics*, 37 (7-8), pp. 450-8, Oct-Dec 2013.
- [112] L. Bi, J. Kim, L. F. Wen, and D. D. Feng, "Automated and Robust PERCIST-based Thresholding framework for whole body PET-CT studies," *2012 Annual International Conference of the Ieee Engineering in Medicine and Biology Society (Embc)*, pp. 5335-8, 2012.
- [113] R. L. Wahl, H. Jacene, Y. Kasamon, and M. A. Lodge, "From RECIST to PERCIST: Evolving Considerations for PET Response Criteria in Solid Tumors," *Journal of Nuclear Medicine*, 50 pp. 122s-50s, May 1 2009.
- [114] J. A. Nelder and R. Mead, "A Simplex-Method for Function Minimization," *Computer Journal*, 7 (4), pp. 308-13, 1965.
- [115] R. R. Barton and J. S. Ivey, "Nelder-Mead simplex modifications for simulation optimization," *Management Science*, 42 (7), pp. 954-73, Jul 1996.
- [116] J. C. Lagarias, J. A. Reeds, M. H. Wright, and P. E. Wright, "Convergence properties of the Nelder-Mead simplex method in low dimensions," *Siam Journal on Optimization*, 9 (1), pp. 112-47, Dec 21 1998.
- [117] A. Zilinskas, "Practical mathematical optimization: An introduction to basic optimization theory and classical and new gradient-based algorithms.," *Interfaces*, 36 (6), pp. 613-5, Nov-Dec 2006.
- [118] Y. H. Dai and Y. Yuan, "A nonlinear conjugate gradient method with a strong global convergence property," *Siam Journal on Optimization*, 10 (1), pp. 177-82, Nov 29 1999.
- [119] O. Fluck, C. Vetter, W. Wein, A. Kamen, B. Preim, and R. Westermann, "A survey of medical image registration on graphics hardware," *Computer Methods and Programs in Biomedicine*, 104 (3), pp. E45-E57, Dec 2011.
- [120] J. M. Kim, D. D. Feng, T. W. D. Cai, and S. Eberl, "Automatic 3D temporal kinetics segmentation of dynamic emission tomography image using adaptive region growing cluster analysis," *2002 Ieee Nuclear Science Symposium, Conference Record, Vols 1-3*, pp. 1580-3, 2003.
- [121] Y. Jung, J. Kim, S. Eberl, M. Fulham, and D. D. Feng, "Visibility-driven PET-CT visualisation with region of interest (ROI) segmentation," *Visual Computer*, 29 (6-8), pp. 805-15, Jun 2013.
- [122] G. Klimeck, S. S. Ahmed, H. Bae, N. Kharche, S. Clark, B. Haley, S. Lee, M. Naumov, H. Ryu, and F. Saied, "Atomistic simulation of realistically sized nanodevices using NEMO 3-D—Part I: Models and benchmarks," *Electron Devices, IEEE Transactions on*, 54 (9), pp. 2079-89, 2007.
- [123] K. L. Ma, "Visualizing time-varying volume data," *Computing in Science & Engineering*, 5 (2), pp. 34-42, Mar-Apr 2003.

- [124] T. J. Jankun-Kelly and K. L. Ma, "A study of transfer function generation for time-varying volume data," *Volume Graphics 2001*, pp. 51-+, 2001.
- [125] F.-Y. Tzeng and K.-L. Ma, "Intelligent feature extraction and tracking for visualizing large-scale 4d flow simulations," *Proceedings of the 2005 ACM/IEEE conference on Supercomputing*, 2005.
- [126] H. Akiba, N. Fout, and K.-L. Ma, "Simultaneous Classification of Time-Varying Volume Data Based on the Time Histogram," *EuroVis*, 2006.
- [127] R. Maciejewski, I. Woo, W. Chen, and D. S. Ebert, "Structuring feature space: A non-parametric method for volumetric transfer function generation," *Visualization and Computer Graphics, IEEE Transactions on*, 15 (6), pp. 1473-80, 2009.
- [128] Y. H. Wang, W. Chen, J. Zhang, T. X. Dong, G. H. Shan, and X. B. Chi, "Efficient Volume Exploration Using the Gaussian Mixture Model," *Ieee Transactions on Visualization and Computer Graphics*, 17 (11), pp. 1560-73, Nov 2011.
- [129] J. Woodring and H. W. Shen, "Semi-Automatic Time-Series Transfer Functions via Temporal Clustering and Sequencing," *Computer Graphics Forum*, 28 (3), pp. 791-8, Jun 10 2009.
- [130] P. A. Freeborough, N. C. Fox, and R. I. Kitney, "Interactive algorithms for the segmentation and quantitation of 3-D MRI brain scans," *Computer methods and programs in biomedicine*, 53 (1), pp. 15-25, 1997.
- [131] E. Day, J. Betler, D. Parda, B. Reitz, A. Kirichenko, S. Mohammadi, and M. Miften, "A region growing method for tumor volume segmentation on PET images for rectal and anal cancer patients," *Medical physics*, 36 (10), pp. 4349-58, 2009.
- [132] J. Kim, W. Cai, D. Feng, and S. Eberl, "Segmentation of VOI from multidimensional dynamic PET images by integrating spatial and temporal features," *Information Technology in Biomedicine, IEEE Transactions on*, 10 (4), pp. 637-46, 2006.
- [133] G. Nyirenda, J. Kim, L. Wen, and D. D. Feng, "Automated segmentation of tumour changes in temporal PET-CT data," *Biomedical Imaging (ISBI), 2012 9th IEEE International Symposium on*, 2012.
- [134] R. Opfer, W. Brenner, I. Carlsen, S. Renisch, J. Sabczynski, and R. Wiemker, "Automatic lesion tracking for a PET/CT based computer aided cancer therapy monitoring system," *Medical imaging*, 2008.
- [135] J. Kim, A. Kumar, L. F. Wen, S. Eberl, and D. D. Feng, "Visual Tracking of Treatment Response in PET-CT Image Sequences," *International Journal of Computer Assisted Radiology and Surgery*, 2011.
- [136] S. Wolfram, "Statistical mechanics of cellular automata," *Reviews of modern physics*, 55 (3), p. 601, 1983.
- [137] Y. Liu, H. D. Cheng, J. H. Huang, Y. T. Zhang, and X. L. Tang, "An Effective Approach of Lesion Segmentation Within the Breast Ultrasound Image Based on the Cellular Automata Principle," *Journal of Digital Imaging*, 25 (5), pp. 580-90, Oct 2012.
- [138] A. Hamamci, N. Kucuk, K. Karaman, K. Engin, and G. Unal, "Tumor-Cut: Segmentation of Brain Tumors on Contrast Enhanced MR Images for Radiosurgery

Applications," *Ieee Transactions on Medical Imaging*, 31 (3), pp. 790-804, Mar 2012.

- [139] A. Hamamci, N. Kucuk, K. Karaman, K. Engin, and G. Unal, "Tumor-Cut: Segmentation of Brain Tumors on Contrast Enhanced MR Images for Radiosurgery Applications," *Medical Imaging, IEEE Transactions on*, 31 (3), pp. 790-804, 2012.
- [140] W. R. Crum, O. Camara, and D. L. G. Hill, "Generalized overlap measures for evaluation and validation in medical image analysis," *Ieee Transactions on Medical Imaging*, 25 (11), pp. 1451-61, Nov 2006.
- [141] N. R. Pal and S. K. Pal, "A review on image segmentation techniques," *Pattern Recognition*, 26 (9), pp. 1277-94, 1993.
- [142] K. T. Bae, M. L. Giger, C. T. Chen, and C. E. Kahn, "Automatic Segmentation of Liver Structure in Ct Images," *Medical Physics*, 20 (1), pp. 71-8, Jan-Feb 1993.
- [143] T. H. Lee, M. F. A. Fauzi, and R. Komiya, "Segmentation of CT Brain Images Using K-means and EM Clustering," *Computer Graphics, Imaging and Visualisation - Modern Techniques and Applications, Proceedings*, pp. 339-44, 2008.
- [144] J. A. Lee, "Segmentation of positron emission tomography images: Some recommendations for target delineation in radiation oncology," *Radiotherapy and Oncology*, 96 (3), pp. 302-7, Sep 2010.
- [145] M. Singh, P. Patel, D. Khosla, and T. Kim, "Segmentation of functional MRI by K-means clustering," *Ieee Transactions on Nuclear Science*, 43 (3), pp. 2030-6, Jun 1996.
- [146] M. X. H. Yan and J. S. Karp, "Segmentation of 3D brain MR using an adaptive K-means clustering algorithm," *Nuclear Science Symposium & Medical Imaging Conference - 1994 Ieee Conference Record, Vols 1-4*, pp. 1529-33, 1994.
- [147] Y. H. Gong, G. Proietti, and C. Faloutsos, "Image indexing and retrieval based on human perceptual color clustering," *1998 Ieee Computer Society Conference on Computer Vision and Pattern Recognition, Proceedings*, pp. 578-83, 1998.
- [148] W. K. Leow and R. Li, "Adaptive binning and dissimilarity measure for image retrieval and classification," *2001 Ieee Computer Society Conference on Computer Vision and Pattern Recognition, Vol 2, Proceedings*, pp. 234-9, 2001.
- [149] J. A. Hartigan, "Clustering algorithms," 1975.
- [150] D. Arthur and S. Vassilvitskii, "k-means++: The advantages of careful seeding," *Proceedings of the eighteenth annual ACM-SIAM symposium on Discrete algorithms*, 2007.
- [151] S. Arora, P. Raghavan, and S. Rao, "Approximation schemes for Euclidean k-medians and related problems," *Proceedings of the thirtieth annual ACM symposium on Theory of computing*, 1998.
- [152] M. Inaba, N. Katoh, and H. Imai, "Applications of weighted Voronoi diagrams and randomization to variance-based k-clustering," *Proceedings of the tenth annual symposium on Computational geometry*, 1994.
- [153] R. Farivar, D. Rebolledo, E. Chan, and R. H. Campbell, "A Parallel Implementation of K-Means Clustering on GPUs," *PDPTA*, 2008.

- [154] Y. Li, K. Zhao, X. Chu, and J. Liu, "Speeding up k-means algorithm by gpus," *Computer and Information Technology (CIT), 2010 IEEE 10th International Conference on*, 2010.
- [155] K. J. Kohlhoff, M. H. Sosnick, W. T. Hsu, V. S. Pande, and R. B. Altman, "CAMPAIGN: an open-source library of GPU-accelerated data clustering algorithms," *Bioinformatics*, 27 (16), pp. 2321-2, 2011.
- [156] N. Ayache, "Medical computer vision, virtual reality and robotics," *Image and Vision Computing*, 13 (4), pp. 295-313, 1995.
- [157] T. Ropinski, J. Praßni, F. Steinicke, and K. Hinrichs, "Stroke-Based Transfer Function Design," *Volume Graphics*, 2008.
- [158] I. Woo, R. Maciejewski, K. P. Gaither, and D. S. Ebert, "Feature-Driven Data Exploration for Volumetric Rendering," *Ieee Transactions on Visualization and Computer Graphics*, 18 (10), pp. 1731-43, Oct 2012.